

**OPTICAL MICROFIBER-BASED SENSOR AND
PULSE FIBER LASER INCORPORATING GRAPHENE
SATURABLE ABSORBER**

MUWAFaq FADHIL JADDOA

**FACULTY OF SCIENCE
UNIVERSITY OF MALAYA
KUALA LUMPUR**

2017

**OPTICAL MICROFIBER-BASED SENSOR AND
PULSE FIBER LASER INCORPORATING GRAPHENE
SATURABLE ABSORBER**

MUWAFAQ FADHIL JADDOA

**THESIS SUBMITTED IN FULFILMENT OF THE
REQUIREMENTS FOR THE DEGREE OF DOCTOR OF
PHILOSOPHY**

**DEPARTMENT OF PHYSICS
FACULTY OF SCIENCE
UNIVERSITY OF MALAYA
KUALA LUMPUR**

2017

UNIVERSITY OF MALAYA
ORIGINAL LITERARY WORK DECLARATION

Name of Candidate: **Muwafaq Fadhil Jaddoa**

Matric No: **SHC130113**

Name of Degree: **Doctor of Philosophy**

Title of Thesis: **Optical Microfiber-Based Sensor and Pulse Fiber Laser**

Incorporating Graphene Saturable Absorber

Field of Study: **Experimental Physics**

I do solemnly and sincerely declare that:

- (1) I am the sole author/writer of this Work;
- (2) This Work is original;
- (3) Any use of any work in which copyright exists was done by way of fair dealing and for permitted purposes and any excerpt or extract from, or reference to or reproduction of any copyright work has been disclosed expressly and sufficiently and the title of the Work and its authorship have been acknowledged in this Work;
- (4) I do not have any actual knowledge nor do I ought reasonably to know that the making of this work constitutes an infringement of any copyright work;
- (5) I hereby assign all and every rights in the copyright to this Work to the University of Malaya ("UM"), who henceforth shall be owner of the copyright in this Work and that any reproduction or use in any form or by any means whatsoever is prohibited without the written consent of UM having been first had and obtained;
- (6) I am fully aware that if in the course of making this Work I have infringed any copyright whether intentionally or otherwise, I may be subject to legal action or any other action as may be determined by UM.

Candidate's Signature

Date:

Subscribed and solemnly declared before,

Witness's Signature

Date:

Name:

Designation:

ABSTRACT

As part of the work presented in this thesis, optical microfibers have been fabricated, characterized and studied in detail. These microfibers have a compact structure, a fast response time, and a strong evanescent field effect and enable facile waveguide fabrication through the reduction of the single-mode fiber diameter. Two methods have been used to fabricate the optical microfibers: a heat-and-pull method using a flame and a heat-and-pull method using a microheater. These methods' advantages lie in their wide array of applications, such as optical sensors and communications. For this study, experimental studies on optical sensors based on optical microfibers (OMFs) were conducted, focusing on the use of inline microfiber Mach-Zehnder interferometer (IMMZI)-based sensors. The responses of IMMZI sensors with various diameters and for various refractive indices of the surrounding medium have been analyzed and experimentally investigated. In addition, an IMMZI was also used to tune single-wavelength erbium-doped fibers (EDFs) based on the stretching technique. The effects of increasing and decreasing the strain force on the IMMZI were also observed. Because of their many uses, additional potential applications based on the interaction of an optical microfiber's evanescent field with saturable absorbers were also experimentally studied. To serve as passive saturable absorbers, graphene and graphene oxide were deposited or fabricated as a thin film to be utilized in an optical microfiber cavity to generate EDF-based multi-wavelength, Q-switched and mode-locked lasing. The optical microfiber acted as a multi-modal interference medium to form an optical-wavelength-selective filter.

ABSTRAK

Sebagai sebahagian kerja yang dispersembahkan di dalam tesis ini, gentian mikrooptik telah dihasilkan, dikaji sifatnya secara lebih teliti. Mikrooptik gentian ini mempunyai struktur yang kompak, tindak balas yang cepat, dan medan *evanescent* yng kuat, dan membolehkan ketelitian keberhasilan pandu gelombang melalui pengurangan diameter mod tunggal gentian optik. Dua kaedah telah digunapakai untuk menghasilkan gentian mikrooptik; kaedah panas dan tarik menggunakan bara api dan panas dan kaedah panas dan tarik menggunakan pemanas mikro. Kelebihan kedua-dua method ini terletak kepada variasi applikasi yang boleh digunakan, sebagai contoh sensor optik dan komunikasi optik. Untuk kajian ini, ujikaji untuk sensor optik berdasarkan gentuan mikrooptik telah dijalankan, di mana fokus lebih kepada dalam-garisan mikrooptik Mach-Zehnder interferometer (IMMZI) sebagai asas sensor. Tindak balas IMMZI dengan variasi diameter dan juga variasi indeks refraktif dare medium berdekatan telah dianalisis dan diujikaji. Sebagai tambahan, IMMZI jug digunakan untuk penalaan variasi gelombang tunggal erbium-doped fibers (EDF) , hasil dari teknik regangan. Kesan dari penaikan dan penurunan dari tekanan regangan juga dikaji. Disebabkan banyak kegunaan, ada potensi penambahan applikasi dari interaksi gentian mikrooptik medan evanescent bersama penyerap ketepuan juga dikaji secara amali. Untuk dijadikan sebagai penyerap ketepuan pasif, graphene dan graphene oksida telah didepositkan atau dihasilkan sebagai filem nipis untuk digunakan utk di dalam gentian mikrooptik untuk menjana EDFmulti gelombang,Q-switched dan mode-lock laser. Gentian mikrooptik bertindak sebagai multi-modal interference medium untuk menghasilkan penapis gelombang-selektif gentian mikrooptik.

ACKNOWLEDGMENTS

It would not have been possible to complete this doctoral thesis without the help, guidance and support of many people around me. I am extremely grateful to my supervisor Prof. Datuk Dr. Harith Ahmad, Director of the Photonic Research Center at the University of Malaya, for the patience, encouragement and guidance given to me throughout my PhD study. His inspiration and valuable suggestions propelled me to complete this research.

I offer special thanks to Dr. Ali A. Jasim for his generous support, especially at the beginning of my PhD study, and for his views and encouragement, which helped me in overcoming many problems. It was my pleasure to work with him.

I would also like to thank Dr. Mohd. Zulhakimi Ab. Razak for his continuous advice on effective writing skills, which facilitated the journal paper writing process and this thesis. I owe him many thanks for discussing and assisting in various laboratory experiments.

Within our Photonic Research Centre, I would like to extend my gratitude to Dr. Saaidal Razali, for his assistance in the laboratory and for his helpful comments, and to Dr. Tiu Zian, who patiently answered many questions and helped to solve several problems I encountered in experiments. I am also grateful to Dr. Mohd Afiq Ismail and Dr. Iraj Sadegh for their assistance. I would also like to extend special thanks to all my friends and research colleagues, especially Md. Jahid Faruki and Muhammad Aizi Mat Salim.

Finally, I would like to express my gratitude to my wife for all the support she has provided all these years!

TABLE OF CONTENTS

ABSTRACT	iii
ABSTRAK	iv
ACKNOWLEDGMENTS	v
TABLE OF CONTENTS.....	vi
LIST OF FIGURES	x
LIST OF TABLES	xiv
LIST OF SYMBOLS AND ABBREVIATIONS	xv
CHAPTER 1: INTRODUCTION.....	1
1.1 Background on Optical Fibers for Communication and Sensing Technology	1
1.2 Optical Microfibers.....	2
1.3 Optical Microfiber Devices	3
1.4 Fiber Lasers	4
1.5 Pulsed Fiber Lasers.....	5
1.6 Motivation.....	7
1.7 Objectives	8
CHAPTER 2: LITERATURE REVIEW.....	9
2.1 Introduction to Optical Microfibers.....	9
2.2 Features of Optical Microfibers.....	10
2.2.1 Evanescent Field.....	10
2.2.2 Optical Microfiber Loss	15
2.2.3 Nonlinear Properties.....	16
2.2.4 Dispersion.....	17
2.3 Methods of Fabricating Optical Microfibers	19

2.3.1	Heat-and-Pull Method	19
2.3.2	Microheater Brushing.....	21
2.3.3	Focused CO ₂ Laser	22
2.3.4	Etching.....	23
2.3.5	Polishing.....	24
2.4	Guidance of Light Modes Inside an Optical Microfiber	26
2.5	Optical Microfiber Structures	28
2.6	Geometric Classification of Optical Microfibers	33
2.6.1	Biconical Optical Microfibers	33
2.6.2	Abrupt Optical Microfibers	39
2.7	Optical Microfiber Applications.....	41
2.7.1	Optical-Microfiber-Based Sensing.....	41
2.7.2	Optical-Microfiber-Based Photonics.....	44
2.8	Pulsed Fiber Lasers Based on Optical Microfibers	46
2.9	Multi-wavelength Erbium-Doped Fiber Lasers Based on Optical Microfibers	48
2.10	Saturable Absorbers and Their Characteristics.....	49

CHAPTER 3: FABRICATION AND PREPARATION OF OPTICAL MICROFIBERS AND SATURABLE ABSORBER MATERIALS.....50

3.1	Introduction.....	50
3.2	Fabrication of Optical Microfibers Using a Modified CNC Machine.....	50
3.3	Fabrication of Optical Microfibers Using the Vytran System.....	52
3.4	Saturable Absorber Properties	54
3.4.1	Thin-Film Saturable Absorber.....	54
3.4.2	Saturable Absorber Deposited on the Surface of an Optical Microfiber..	55
3.5	Characteristics of Graphene and Graphene Oxide Saturable Absorbers	56
3.6	Preparation of Chemical Solutions	57

CHAPTER 4: OPTICAL INLINE MICROFIBER MACH-ZEHNDER INTERFEROMETER FOR SENSING APPLICATIONS59

4.1	Introduction.....	59
4.2	Fabrication of An Inline Microfiber Mach-Zehnder Interferometer	60
4.2.1	Characteristic of Inline Microfiber Mach-Zehnder Interferometer	61
4.3	NaCl Detection Using Inline Microfiber Mach-Zehnder Interferometer	64
4.4	Results and Discussion	66
4.5	Comparison of Optical Microfiber Structures for KNO ₃ Refractive Index Detection.....	72
4.5.1	Material	72
4.5.2	Experimental Setup	72
4.5.3	Results and Discussion	74
4.6	An Inline Microfiber Mach-Zehnder Interferometer for Strain Sensing	78
4.6.1	Experimental Setup	79
4.6.2	Results and Discussion	81

CHAPTER 5: MULTI-WAVELENGTH AND PULSED LASERS BASED ON TAPERED OPTICAL FIBERS AND GRAPHENE SATURABLE ABSORBERS 87

5.1	Introduction.....	87
5.2	Q-Switched Erbium-Doped Fiber Laser	88
5.3	Deposition of Graphene Oxide Around an Optical Microfiber	89
5.4	Experimental Setup.....	90
5.5	Results and Discussion	91
5.6	Dual-Wavelength Q-Switched Pulsed Fiber Laser	96
5.7	Experimental Setup and Fabrication.....	97
5.8	Results and Discussion	101

5.9	Generation of Mode-Locked Pulsed Lasing by Utilizing the Interaction of an Evanescent Field with Graphene Oxide	106
5.10	Experimental Setup.....	107
5.11	Results and Discussion	108
CHAPTER 6: CONCLUSIONS AND FUTURE WORK		115
6.1	Conclusions	115
6.1.1	Sensing Applications Based on an Inline Microfiber Mach-Zehnder Interferometer	115
6.1.2	Erbium-Doped Fiber Laser Pulse Generation	116
6.2	Future Work.....	118
REFERENCES		119
LIST OF PUBLICATIONS AND PAPERS PRESENTED		136
LIST OF PUBLICATIONS (FRONT PAGE).....		137
APPENDIX A		142
APPENDIX B		162

LIST OF FIGURES

Figure 2.1: Profile of the structure of an optical microfiber.	10
Figure 2.2: Cross sections of a) a single-mode fiber and b) a multimode fiber.	11
Figure 2.3: Light propagation inside an optical fiber.	12
Figure 2.4: Transmission power of an optical microfiber as a function of the waist diameter (Ma et al., 2014).	13
Figure 2.5: Z-direction Poynting vectors of a 200nm diameter silica microfiber at 633nm wavelength: (a) 3-D view and (b) 2-D view (Lou et al., 2014).	13
Figure 2.6: Dispersion profiles for elliptical optical microfibers of different diameters (Tang et al., 2016).	18
Figure 2.7: Schematic diagram of a heat-and-pull rig.	20
Figure 2.8: Schematic diagram of a heat-and-pull system using a thermoelectric microheater.	21
Figure 2.9: Fiber tapering setup based on a focused CO ₂ laser (Ozcan et al., 2007).	23
Figure 2.10: Schematic diagram of a D-shaped fiber.	25
Figure 2.11: Index profile of an air-clad optical microfiber (Tong & Sumetsky, 2011).	28
Figure 2.12: Image of an MFBG (Kou et al., 2011).	30
Figure 2.13: Schematic illustrations of optical microfiber resonators: (a) an MLR, (b) an MKR and (c) an MCR (Chen et al., 2013).	32
Figure 2.14: Schematic diagram of two structures of microfiber MZIs (Chen et al., 2013).	33
Figure 2.15: Schematic illustration of a biconical optical microfiber profile (Harun et al., 2013).	34
Figure 2.16: The shapes of a standard optical fiber (a) before heating and (b) after the heat-and-pull process (Harun et al., 2013).	36
Figure 2.17: The profiles of an optical fiber (a) before tapering and (b) after tapering (Harun et al., 2013).	38

Figure 2.18: Profile of an optical microfiber with $\alpha=1$ and $L_0=10$ mm (Harun et al., 2013).	39
Figure 2.19: Schematic illustration of an optical microfiber coupler (Jung et al., 2009).	46
Figure 3.1: Optical microfiber tapering system.	52
Figure 3.2: Vytran GPX-3400 workstation.	53
Figure 3.3: Illustration of a graphene thin-film on optical fiber pigtail.	55
Figure 3.4: Microscopic image of a graphene oxide saturable absorber device.	56
Figure 4.1: IMMZI (a) schematic diagram and (b) optical microscope image.	61
Figure 4.2: Output interference spectrum of an IMMZI with a dual-waist diameter of $10\ \mu\text{m}$	64
Figure 4.3: Schematic for NaCl detection.	65
Figure 4.4: Transmitted interference spectra of the four IMMZI samples (a, b, c, d) with seven solutions of NaCl.	67
Figure 4.5: Dip wavelengths correlation with different RI ranging from 1.31837 to 1.31928 for the four samples of IMMZI (a, b, c, d).	69
Figure 4.6: Responsivity of IMMZI samples for dissimilar waist diameters.	71
Figure 4.7: Experimental setup for KNO_3 detection.	73
Figure 4.8: Output spectrum of the fiber laser cavity with the IMMZI.	74
Figure 4.9: Tuning of the transmission spectrum of the IMMZI with different concentrations of KNO_3	75
Figure 4.10: Output spectrum of the fiber laser cavity with the STF.	76
Figure 4.11: Tuning of the transmission spectrum of the STF with different concentrations of KNO_3	76
Figure 4.12: IMMZI resonant wavelength as a function of the refractive index.	77
Figure 4.13: STF resonant wavelength as a function of the refractive index.	78
Figure 4.14: Experimental setup for IMMZI strain measurements based on a tunable single-wavelength EDF laser.	80

Figure 4.15: Microscopic image of the IMMZI.	81
Figure 4.16: Output power of the IMMZI at increasing strain values.	82
Figure 4.17: Output power of the IMMZI at decreasing strain values.....	83
Figure 4.18: Output power of the IMMZI measured using the second strain adjustment method.	84
Figure 4.19: Stability over time of the wavelength peak at 1557.182 nm.	84
Figure 4.20: Wavelength shifts versus strain values from 20 to 80 μm	85
Figure 5.1: (a) Raman spectrum of the GOSA and (b) microscopic image of a microfiber deposited with the GOSA.....	90
Figure 5.2: Scheme of the proposed passively Q-switched EDF laser.	91
Figure 5.3: Optical spectra of the fiber laser at two different pump currents.	92
Figure 5.4: Q-switched pulse trains generated at different pump powers (56.17 mW, 69.85 mW, 88.36 mW and 105.98 mW).....	93
Figure 5.5: RF spectrum at a pump power of 88.36 mW.....	94
Figure 5.6: Repetition rate and pulse width as functions of the input power.....	95
Figure 5.7: Pulse energy and output power as functions of the input power.	96
Figure 5.8: Experimental setup for the dual-wavelength Q-switched EDF with a tapered fiber and a GSA.	99
Figure 5.9: Output optical spectrum of the fabricated tapered fiber (inset: microscopic image of the tapered fiber, with a diameter of 12 μm).	100
Figure 5.10: Raman spectrum of the deposited graphene saturable absorber.....	101
Figure 5.11: a) Dual-wavelength optical spectrum and b) passively Q-switched pulse train, at the threshold pump power of 83.82 mW.	102
Figure 5.12: Q-switched pulse trains at different pump powers: (a) 88.36 mW, (b) 96.86 mW, (c) 115.91 mW and (d) 135.93 mW.	103
Figure 5.13: Repetition rate and pulse width of the Q-switched pulsed laser setup versus the pump power.	104
Figure 5.14: Pulse energy and total output power versus the pump power in the Q-switched pulsed laser setup.....	105

Figure 5.15: Test of the stability over time of the output spectrum of the dual-wavelength Q-switched laser setup.....	106
Figure 5.16: Mode-locked EDF laser based on a GO-coated D-shaped fiber.	107
Figure 5.17: Raman spectrum of graphene oxide.	108
Figure 5.18: Optical spectra corresponding to the mode-locked pulses produced at different pump powers.	109
Figure 5.19: Spectral properties of the mode-locked pulses measured through the OSA.....	109
Figure 5.20: Mode-locked pulse train recorded at a pump power of 167.23 mW.	110
Figure 5.21: Radio-frequency spectrum.....	111
Figure 5.22: Autocorrelation trace with sech^2 profiling.....	112
Figure 5.23: Relation between the pump power and output power.	113
Figure 5.24: Stability of the output optical spectrum over time.	114

LIST OF TABLES

Table 4.1: Geometric Parameters of the IMMZI Samples	62
Table 4.2: Parameters of the IMMZI and STF	73

University of Malaya

LIST OF SYMBOLS AND ABBREVIATIONS

ASE	:	Amplified Spontaneous Emission
CMKR	:	Cascade Microfiber Knot Resonator
CNC	:	Computer Numerically Controlled
CNT	:	Carbon Nanotube
EDF	:	Erbium-Doped Fiber
EDFA	:	Erbium-Doped Fiber Amplifier
Er^{3+}	:	Erbium
FBG	:	Fiber Bragg Grating
FPI	:	Fabry-Pérot Interferometer
FSR	:	Free Spectral Range
FWHM	:	Full Width at Half Maximum
GO	:	Graphene Oxide
GOSA	:	Graphene Oxide Saturable Absorber
GSA	:	Graphene Saturable Absorber
GVD	:	Group Velocity Dispersion
HBMF	:	Highly Birefringent Microfiber
IMG	:	Index-Matching Gel
IMMZI	:	Inline Microfiber Mach-Zehnder Interferometer
ISO	:	Optical Isolator
KNO_3	:	Potassium Nitrate
LD	:	Laser Diode
MCR	:	Microfiber Coil Resonator
MFBG	:	Microfiber Fiber Bragg Grating
MI	:	Michelson Interferometer

MKR	:	Microfiber Knot Resonator
MLPFG	:	Microfiber Long-Period Fiber Grating
MLR	:	Microfiber Loop Resonator
MMZI	:	Microfiber Mach-Zehnder Interferometer
MZI	:	Mach-Zehnder Interferometer
NaCl	:	Sodium Chloride
NALM	:	Nonlinear Amplifying Loop Mirror
NOLM	:	Nonlinear Optical Loop Mirror
NPR	:	Nonlinear Polarization Rotation
OMF	:	Optical Microfiber
OMNF	:	Optical Micro/Nanofiber
OSA	:	Optical Spectrum Analyzer
PC	:	Polarization Controller
PCF	:	Photonic Crystal Fiber
POF	:	Plastic Optical Fiber
RBW	:	Resolution Bandwidth
RF	:	Radio-Frequency
RI	:	Refractive Index
SA	:	Saturable Absorber
SESAM	:	Semiconductor Saturable Absorber Mirror
SLM	:	Single Longitudinal Mode
SMF	:	Single-Mode Fiber
SNR	:	Signal-to-Noise Ratio
STF	:	Single Tapered Fiber
SWCNT	:	Single-Walled Carbon Nanotube
TBP	:	Time-Bandwidth Product

TMD : Transition Metal Dichalcogenide
WDM : Wavelength Division Multiplexer

University of Malaya

CHAPTER 1: INTRODUCTION

1.1 Background on Optical Fibers for Communication and Sensing Technology

Optical fibers play a very significant role in our daily lives because of their ability to transfer a large amount of information over a long distance with low attenuation. A conventional optical fiber consists of two main components: the inner core, which is made of germanium-doped silica with a diameter of approximately 9 μm , and the outer cladding, which is made of pure silica with a diameter of 125 μm . In addition to the advantages of optical fibers for communication applications, optical fibers have also seen significant use in the fields of sensing and lasing (Li et al., 2012a; Mary et al., 2014). Since the 1970s, previous experiments have successfully demonstrated low-loss optical fibers for sensing applications (Grattan & Sun, 2000); various sensors based on optical fibers have been developed and demonstrated for measuring different physical, chemical and biological parameters, such as temperature, current, bio-chemical characteristics, humidity, pH, and refractive index (RI) (Gholamzadeh & Nabovati, 2008; Monk & Walt, 2004). Optical fiber sensing technology works based on the modification of one or more properties of the light propagating inside the fiber, which include intensity, interferometric behavior, resonance, and polarization (Grattan & Sun, 2000). Continuous advancements in optical fiber technology have been achieved by virtue of its numerous benefits, such as immunity to electromagnetic field interference, long-distance data transmission capability, small size, light weight, chemical and biological inertness, high sensitivity and ability to operate at high temperatures. These advantages are useful in telecommunication systems, power industry applications, biomedical measurements, etc. (Culshaw, 2004).

1.2 Optical Microfibers

Recently, with the rapid progress in micro/nanotechnology and increasing demands for optical sensors with higher performance and versatility, the spatial miniaturization of optical components and devices has become one of the current trends in the development of fiber-optic sensors. It is apparent that reducing the size of a sensing structure is an essential step in endowing the sensor with faster response, higher sensitivity, lower power consumption and better spatial resolution, and OMFs are among the best candidates for reducing the size of a sensing structure. As a combination of fiber optics and nanotechnology, OMFs have been emerging as a novel platform for exploring fiber-optic technology at the micro- or nanoscale. An optical microfiber, which is fabricated by heating and pulling a standard optical fiber or bulk glass, has a diameter of approximately 1 μm , a low roughness and a high index contrast with the surrounding medium. Because of its sub-wavelength cross section, an OMFs exhibits many novel properties, such as tight optical confinement, high fractional evanescent fields, and large manageable waveguide dispersion, which are highly desirable for functionalizing fiber-optic circuits with great versatility on the micro/nano scale (Lou et al., 2014; Wu & Tong, 2013). An OMF is typically made by pulling an optical fiber once it has been heated to its softening temperature to reduce its diameter to tens of micrometers. As a result, the tapered fiber consists of three contiguous parts: one taper waist segment, with a small and uniform diameter, and two conical transition regions, with a gradually changing diameter. The ends of the conical transition regions are untapered fibers. In reality, the fiber core materials in the waist and transition regions do not exhibit clear boundaries with respect to the cladding material because they mix upon heating (Tian et al., 2011).

Microfibers have attracted extensive interest among researchers, particularly with regard to their fabrication methods, structures and applications, because they offer numerous unique properties, such as a small diameter and a high discontinuity in the

refractive index at the surface compared with conventional optical fibers, enormous evanescent fields, immunity to electromagnetic field effects, facile fabrication, strong confinement and high robustness. These remarkable optical and mechanical characteristics of microfibers make them excellent waveguides for use in fiber-optic circuits and devices in sensor and laser applications (Harun et al., 2012a).

1.3 Optical Microfiber Devices

Recently, with the rapid progress that is being achieved in nanoscience, interest in photonic devices fabricated from tapered optical fibers has been increasing. OMFs, tapered fibers or micro-wires are fiber optics with diameters of a few microns that confine light inside them based on total internal reflection due to the difference in refractive index between the core and cladding (Guan et al., 2013). Based on these interesting properties of OMFs, a variety of devices have been designed and demonstrated for diverse applications to date. Tapered fibers can be categorized into two types. The first category consists of non-resonator-type tapered fibers, which can be shaped into many types, such as straight tapered fibers, Mach-Zehnder interferometers (MZIs), and Michelson interferometers (MIs). A MZI shows many benefits over other structures such as high sensitivity, flexible design and simplicity (Jasim et al., 2013b; Raji et al., 2016). The second category consists of resonator-type tapered fibers, which include all structures that exhibit resonant behavior, such as a microfiber loop resonator (MLR), in which a fabricated tapered fiber is curved into a self-coupling structure with turn by taking advantage of the surface attraction force. At a wavelength of 1.5 μm , the Q factor of an MLR with a diameter of approximately 700 μm has been measured to be 5200 (Sun et al., 2012; Yoon et al., 2015). Another example of this second category is a microfiber coil resonator (MCR), in which a tapered fiber is wrapped around a small rod with a low refractive index to form a helix. An MCR with two turns has a Q factor of 61000 (Belal

et al., 2010; Sumetsky, 2008). A third example is a microfiber knot resonator (MKR), in which the free end of the fiber is first formed into a relatively large loop of approximately a few millimeters in diameter, which is then tightened into a smaller knot by pulling on the free end of the fiber. Thus, a microfiber knot is obtained (Jiang et al., 2006). Tapered fiber resonators are often embedded in low-index materials to protect them from moisture and dust, which may affect the stability of a resonator's transmission properties (Ismaeel et al., 2013). In most tapered fiber structures, a portion of the power is transferred outside the physical boundaries, forming a phenomenon known as an evanescent field, where it can interact with the external environment. These evanescent fields are used in a variety of applications, including sensors, photonic devices, couplers, and atom traps (Jasim et al., 2012; Ma et al., 2014; Tong, 2010; Wang et al., 2012a).

1.4 Fiber Lasers

An optical fiber is flexible, has ultra-low power loss and is an ideal waveguide. Thus, the first fiber laser is constructed in 1963 by Koester and Snitzer (Dianov, 2009), and fiber lasers with excellent performance were made possible by using optical fibers with their cores doped with rare-earth ions as the gain medium. Recently, it has been found that fiber lasers show many advantages over other types of lasers, such as CO₂ lasers, in terms of high output power, high stability (because the light is tightly confined to the core), small size, and practical usability. For these reasons, fiber lasers play an important role in the field of laser research. Furthermore, fiber lasers are widely used in many applications, including telecommunications, materials processing, medicine and spectroscopy. The gain medium in a fiber laser system is usually a single-mode fiber whose core is doped with rare-earth elements such as erbium (Er³⁺) and ytterbium (Yb³⁺). The most common fiber lasers are those with an EDF as a gain device that operates at a wavelength of 1550 nm. This fiber can be pumped with laser sources of different

wavelengths, such as 980 nm and 1480 nm (Nishizawa, 2014). To fabricate an EDF, the core of an optical fiber is doped with Er^{3+} ions. The concentration ratio of the Er^{3+} ions will affect the output spectral characteristics of the EDF. An Er-doped fiber laser has three energy levels: E_1 , E_2 , and E_3 . When the electrons are pumped with 980 nm light, they will be excited from the ground-state energy, E_1 , to the highest energy level, E_3 . Ions at E_3 are unstable and will drop to the ground state via two channels. The first is spontaneous emission; the ions at E_3 transition to E_2 through non-radiative emission and then decay to E_1 through spontaneous emission, emitting photons in the wavelength range of 1520-1570 nm. The spontaneously emitted light will be amplified during its propagation through the fiber in a phenomenon called amplified spontaneous emission (ASE), which is considered to be the main source of noise in the system. The second channel is stimulated emission, which occurs when spontaneous emission has given rise to an appropriate level of ion population inversion between the energy levels of E_2 and E_1 ; during this time, the newly generated photons will be amplified through the fiber, and the system will act as an erbium-doped fiber amplifier (EDFA) (Zhu et al., 2015).

1.5 Pulsed Fiber Lasers

Many applications require a fiber laser source operating in a pulsed mode, including the areas of telecommunications, optical signal processing, sensing, spectroscopy and medical treatment. By virtue of the large gain bandwidth (on the order of tens of nanometers) of the rare-earth elements in a fiber laser, a femtosecond pulse can be produced. Such pulsed lasers may be achieved in two main ways: Q-switching and mode-locking (Set et al., 2004). The Q-switching technique involves controlling the Q factor of a laser system. The ratio between the stored and lost energy for each round trip of propagating light is represented by the Q factor. Therefore, a higher Q factor implies a higher gain. A laser cavity is operating in a Q-switched pulse regime when the stored

energy is released by increasing the pump power. This is because the Q factor is low at the start of pumping and the cavity loss then decreases gradually. Generally, a Q-switched pulsed laser has a low repetition rate (kHz) and a high pulse energy and duration (Svelto & Hanna, 1976). Q-switched pulsed lasers can be classified into two types: active and passive. An acousto-optic or electro-optic modulator is used in all active Q-switched laser cavities to achieve high stability and adjust the repetition rate. However, this technique is expensive and results in complicated design requirements, a low output power and a low damage threshold. By contrast, a passively Q-switched laser system has many advantages, such as compactness, flexibility and simplicity in design. A transition-metal-doped crystal and saturable absorbers, such as semiconductor saturable absorber mirror (SESAM), single-walled carbon nanotubes (SWCNT) and graphene, have been fabricated and demonstrated to generate passively Q-switched pulsed lasing (Chen et al., 2014a; Luo et al., 2010).

Mode-locked pulsed lasers represent the second approach for producing short pulses. In mode locking, a continuous-wave laser is made to produce short pulse trains, where the modes that are independently circulating inside the fiber laser cavity are made to propagate at the same phase velocity by supporting the coherence between them. After each round trip into the cavity, the phase difference between the different modes will be fixed, and a stable short pulse train will be generated (Haus, 2000). Like Q-switched pulsed lasers, mode-locked lasers can also be divided into active and passive types. Various techniques are implemented in active mode-locked lasers, such as Kerr-lens mode locking and SESAMs. However, these techniques have several disadvantages; for example, external perturbations are required to initiate Kerr-lens mode locking, and such systems are highly sensitive to misalignment, whereas SESAMs are complicated and expensive to fabricate (Sun et al., 2010a).

Passive mode locking has been investigated using various approaches, such as nonlinear amplifying loop mirrors (NALMs), nonlinear polarization rotation (NPR) and various saturable absorbers (SAs), all of which have been employed to achieve ultra-short pulses in fiber lasers. Among these techniques, SAs are considered to be effective materials that permit a simple cavity design. Suitable SAs include graphene, graphene oxide (GO), carbon nanotubes (CNTs) and charcoal nanoparticles (Liu et al., 2014; Yang et al., 2015).

1.6 Motivation

The motivation behind this thesis work is to establish microfibers as the basis of novel optical devices that can be integrated into optical fiber technology and nanotechnology. Compared with conventional optical fibers, because of their low loss and small dimensions, microfibers exhibit many interesting properties, such as tight optical confinement, strong evanescent fields, evident surface field enhancement, and large and abnormal waveguide dispersion, which make them ideal nano-waveguides for a variety of optical and photonics applications, including sensing, supercontinuum generation, microfiber-based dye lasing, evanescent wave spectroscopy and atom trapping (Ma et al., 2014). In addition, tapered optical fibers can achieve both Q-switched and mode-locked pulsed fiber lasing with the assistance of suitable SA materials (Kashiwagi & Yamashita, 2009; Lee et al., 2013; Luo et al., 2012).

1.7 Objectives

1. To investigate the effects of evanescent fields in refractive index and strain sensor applications.
2. To investigate the effects of the optical microfiber geometry in tuning the wavelength of an erbium-doped fiber laser.
3. To investigate the dual-wavelength generation in a Q-switched pulsed laser by means of an optical microfiber and a graphene SA.
4. To investigate the interaction of the evanescent field of an optical microfiber with a graphene oxide saturable absorber (GOSA) for the generation of Q-switched pulsed lasing.
5. To demonstrate the generation of mode-locked pulsed lasing using an erbium-doped fiber with the incorporation of GO and a side-polished fiber.

CHAPTER 2: LITERATURE REVIEW

2.1 Introduction to Optical Microfibers

An OMF is an optical waveguide that is fabricated by heating and pulling a standard optical fiber to a small diameter, on the order of a few hundred nanometers to a few microns, especially in the microfiber waist region, which is a down-tapered section of a few millimeters in length along the fiber. Various names are used for OMFs in the literature, such as tapered fibers, subwavelength fibers, micro/nanowires and photonic micro/nanofibers. OMFs have garnered significant interest from researchers over the past two decades because of their various mechanical and optical properties, such as their small size, low cost, large evanescent fields and strong confinement of propagating light. These benefits are why they are preferred over other techniques, especially for sensing and lasing applications. For the manufacturing of OMFs, silica fibers are the most commonly used. However, a wide variety of materials other than silica have also been used, including lead silicate, bismuthate, phosphate, tellurite glasses, chalcogenide glasses and several types of polymers (Chen et al., 2013). Applications based on OMFs first emerged in the early nineteen-seventies, when they were employed to couple two propagating light modes (HE_{11} and HE_{12}) (Snyder, 1970). However, the shortcomings of OMFs include high loss and the complexity of fabricating such fibers with a diameter of approximately 5 μm . An important advance occurred in 2003, when an OMF was fabricated with a diameter of approximately 50 nm and an output power loss of lower than 0.1 dB/mm (Ismaeel et al., 2013; Tong et al., 2003). OMF structures offer two significant advantages relative to lithographically manufactured waveguides: low losses and the simple fabrication of 3-D structures (loops, rings, and knots) (Sumetsky, 2008). Traditionally, the basic shape of an OMF consists of three main regions: the first transition

region (tapering down), the waist region and the second transition region (tapering up). The ends of such an OMF behave as typical single-mode fibers. The diameter reduction achieved for an OMF is highly dependent on the stretching speed and the flame temperature. **Figure 2.1** presents the structural regions of an OMF.

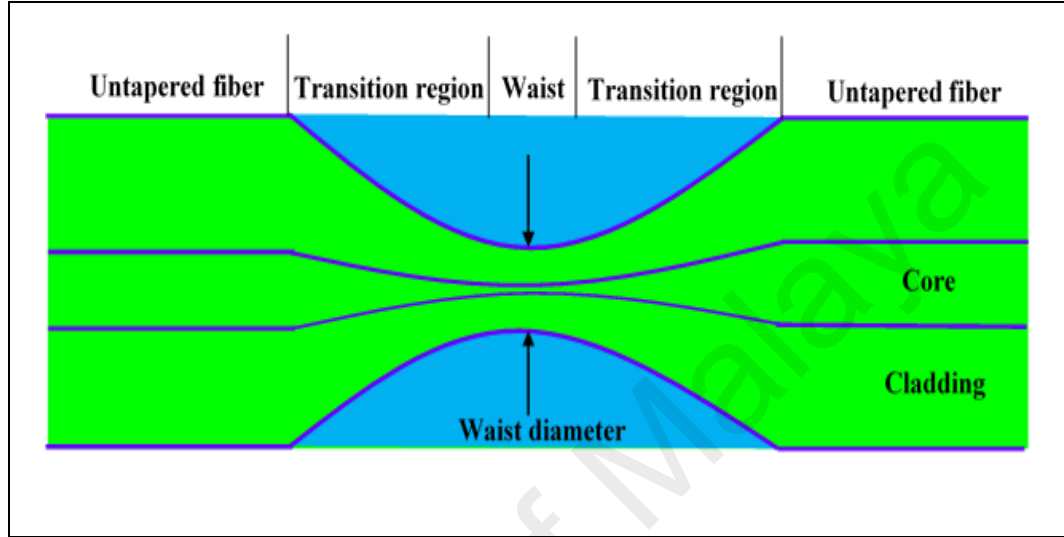


Figure 2.1: Profile of the structure of an optical microfiber.

2.2 Features of Optical Microfibers

This section explains in detail the optical and mechanical characteristics of OMFs, including their evanescent fields, losses, nonlinearity, and dispersion.

2.2.1 Evanescent Field

Silica glass is one of the low-loss materials that are used to make optical fibers. Such a fiber consists of two main layers: an inner cylinder (the core) surrounded by cladding. The light propagates inside the core of the optical fiber because its refractive index is slightly higher than that of the cladding, $n_{co} > n_{cl}$. This difference in refractive index gives rise to total internal reflection when light is incident on the core-cladding interface, thereby confining the light in the fiber core. This type of optical fiber is called a step-index fiber; it is also called a single-mode fiber. By contrast, in a graded-index fiber, the refractive index decreases gradually from the core to the cladding. Such a fiber is also

called a multimode fiber. **Figure 2.2** shows the cross sections of both single-mode and multimode fibers.

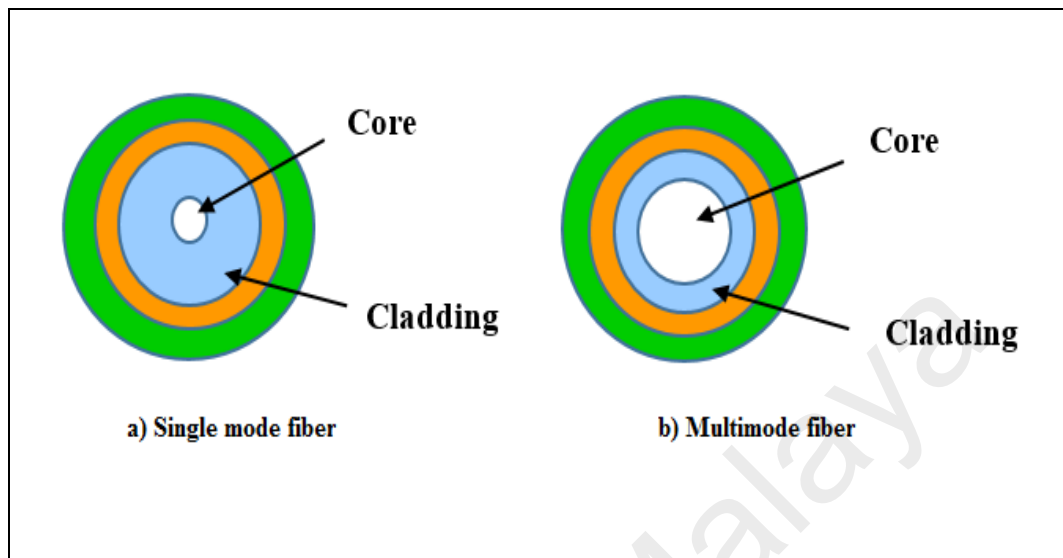


Figure 2.2: Cross sections of a) a single-mode fiber and b) a multimode fiber.

The light that propagates in the core is also called the core mode. It can pass into the cladding region as an evanescent field, but it cannot penetrate into the external medium because the cladding diameter is large ($125\text{ }\mu\text{m}$) relative to the diameter of the core-mode field ($9\text{ }\mu\text{m}$). This evanescent field is insignificant in sensing applications because it cannot be extended into the surrounding medium of the fiber (Mitschke, 2010). **Figure 2.3** shows the light propagation inside an optical fiber based on the total internal reflection effect.

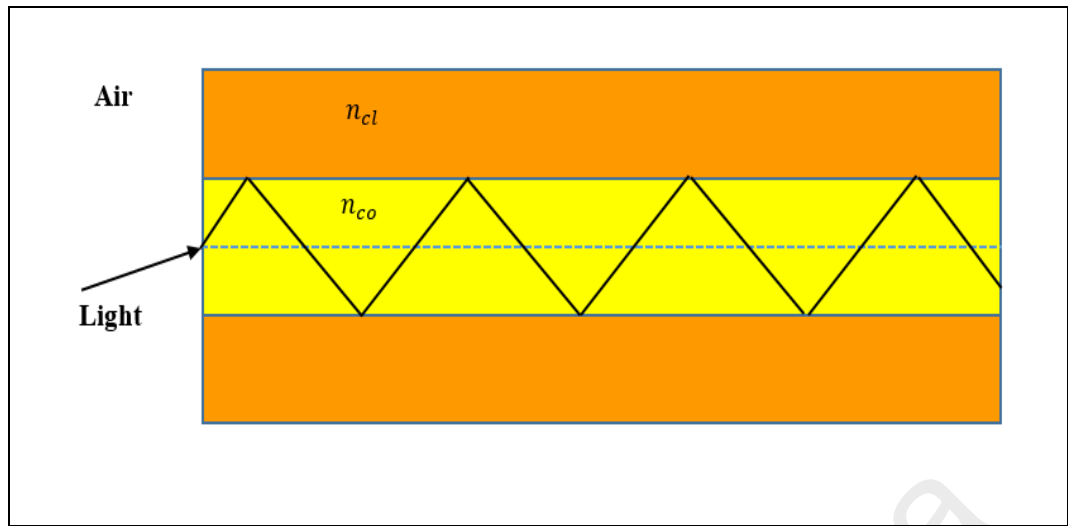


Figure 2.3: Light propagation inside an optical fiber.

An OMF is a dielectric, cylindrical waveguide that is formed by stretching a fiber to a small diameter of approximately a few microns in one local region. As the fiber is tapered, the dimensions of the fiber core and cladding gradually decrease, but their chemical structure remains the same. Once the fiber has been tapered, especially to a waist diameter that is smaller than the wavelength λ of the light, the magnitude of the evanescent field radiation that spreads outside the microfiber increases, enabling the potential to achieve sensing (Ji et al., 2012; Sumetsky, 2006). In addition, the penetration depth of a microfiber's evanescent field grows as the microfiber's waist diameter decreases. The evanescent wave intensity outside the optical microfiber increases as the core-cladding interface in the microfiber gradually decreases (Ma et al., 2014). **Figure 2.4** shows the relationship between the transmission power and the waist diameter of an OMF. **Figure 2.5** shows the Z-direction Poynting vectors of an optical microfiber with a 200nm diameter at a wavelength of 600 nm in (a) a 3-D view and (b) a 2-D view.

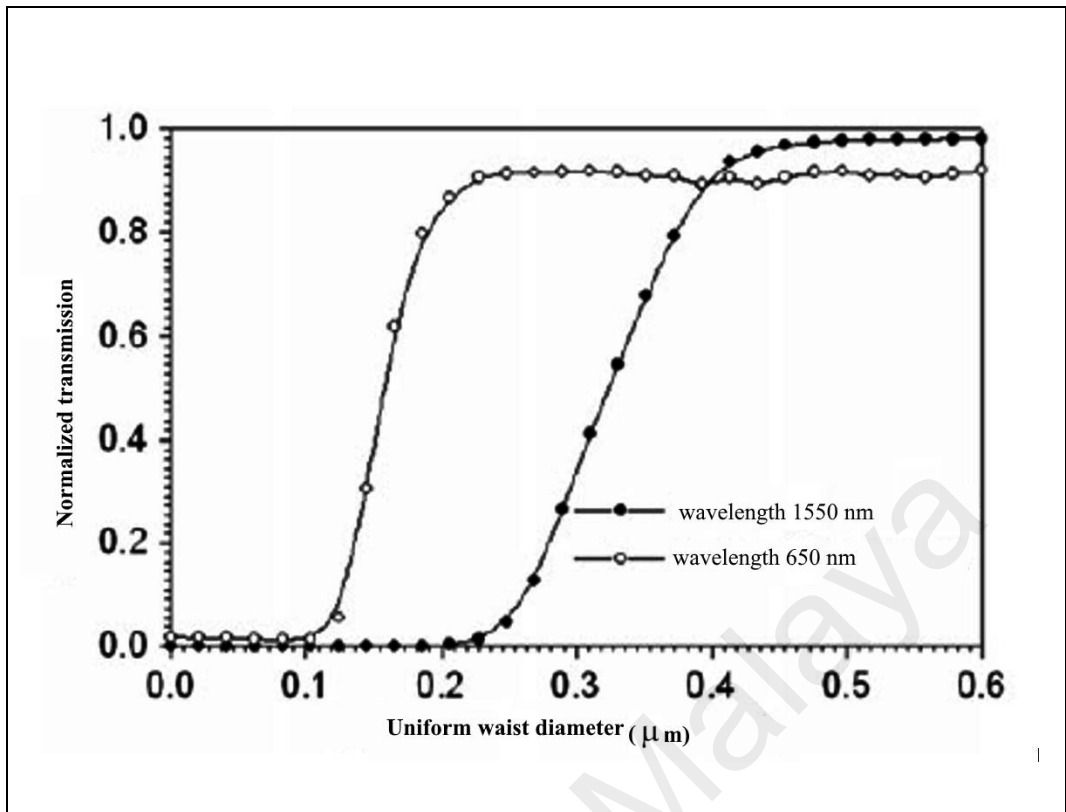


Figure 2.4: Transmission power of an optical microfiber as a function of the waist diameter (Ma et al., 2014).

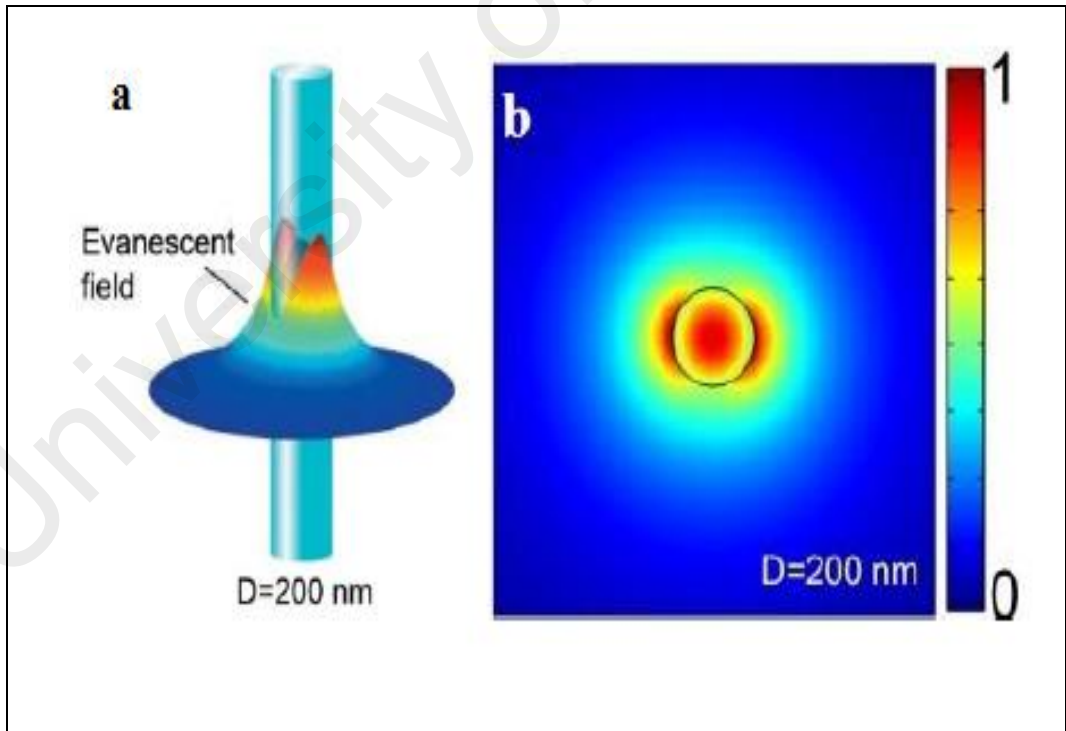


Figure 2.5: Z-direction Poynting vectors of a 200nm diameter silica microfiber at 633nm wavelength: (a) 3-D view and (b) 2-D view (Lou et al., 2014).

The evanescent field of an optical fiber exponentially decays, as represented by the following expression (Zaatar et al., 2000):

$$E(z) = E_0 \exp(-z/d_p) \quad (2.1)$$

where d_p is the penetration depth, which can be written as follows:

$$d_p = \frac{\lambda}{2\pi n_1 (\cos^2 \theta - \cos^2 \theta_c)^{0.5}} = \frac{\lambda}{2\pi n_1 \sqrt{\cos^2 \theta - (n_2/n_1)^2}} \quad (2.2)$$

In addition, both the absorption and scattering of the evanescent field in an OMF can be characterized based on the Beer–Lambert Law as per the following equation (Haddock et al., 2003a) :

$$\ln I/I_0 = -\alpha c \chi \quad (2.3)$$

where I is the output power (mW), I_0 is the input power (mW), α is a characteristic constant that is specific to the microfiber, c is the cell concentration, and χ is the interaction length of the fiber. To evaluate the influence of the tapering of an optical microfiber, a comparative study of the optical characteristics of a de-cladded uniform-core fiber and those of a de-cladded tapered-core fiber in the context of evanescent absorption was conducted by Mignani et al. The fractional power (η) was defined as the fraction of power in the evanescent field with respect to the total power in the fiber. Although the absorption characteristics of both fibers were found to follow the Beer–Lambert Law, the fractional power η differed significantly. For a uniform fiber with a diameter of 200 μm , η ranged from 4×10^{-4} to 8×10^{-4} . By contrast, the parameter η for a tapered fiber was far superior, ranging from 6×10^{-3} to 8×10^{-3} . In addition, the sensitivity is proportional to η , which indicates that tapered-core fibers are 10 times more sensitive than uniform-core fibers (Leung et al., 2007). To enhance the fractional power and evanescent field in the cladding, a hollow microfiber can be used (Wu et al., 2008).

A microfiber long-period fiber grating (MLPFG) has been fabricated using CO₂ laser with a layer of gold nanoparticles immobilized on its surface. This sensor shows an improved evanescent field and an improved effective surface surrounding it, thereby increasing its sensitivity to the external medium (Taghipour et al., 2012). Apart from enhancing the evanescent field by reducing the optical fiber diameter via the tapering process, a tapered fiber can also be bent in the waist region to increase the penetration depth of the evanescent field. A U-shaped optical probe has been found to show a significantly higher sensitivity compared with that of a straight probe with the same dimensions; this finding is attributed to the decrease in the light propagation angle in the U-shaped probe, which improves the penetration depth. By contrast, in the straight probe, the angle of light propagation is nearly constant, and only the variation in the radius affects the evanescent field (Khijwania & Gupta, 1999).

2.2.2 Optical Microfiber Loss

High transmission is one of the desired properties of OMFs for many applications. The power loss of a microfiber can be essentially attributed to low surface smoothness, the microfiber diameter and impurities. Scattering loss is induced in an optical microfiber by surface roughness (Zhai & Tong, 2007). Both the increase in the OMF surface area and the decrease in the microfiber diameter caused by the tapering and drawing of the fiber to create an OMF will increase the propagation loss. In addition, it has been found that the external environment can contribute to increasing the loss of a microfiber as a result of the adherence of particles to its surface (Chuo & Wang, 2011). The experimentally demonstrated transmission loss of an OMF fabricated from silica is measured about 1 dB/m, which is two times greater than the loss of a state-of-the-art telecommunication fiber. Nevertheless, this OMF transmission loss is significantly smaller than that of lithographically fabricated planar photonic circuits. To reduce the effect of dust and microparticles on optical microfiber loss and to recover OMF transmission

characteristics, some chemical solutions can be used (distilled water, acetone, methanol and isopropanol) to clean the surface, or OMFs can be post-processed through heating. However, the OMF surface contamination effect is significantly reduced when the diameter of the microfiber is large (Tong & Sumetsky, 2011).

The propagation loss (α) is highly dependent on microfiber diameter fluctuations and can be represented as in the following equation (Brambilla et al., 2009):

$$\alpha = \frac{1}{4\gamma} \sqrt{\frac{k}{L_f}} \exp\left(-\frac{\pi L_f \gamma^2}{k}\right) \quad (2.4)$$

where k is the propagation constant, γ is the absolute value of the transverse component of the propagation constant, and L_f is the characteristic length of the diameter fluctuations.

2.2.3 Nonlinear Properties

The nonlinear characteristics of an OMF can be determined from the effective nonlinear optical coefficient (Γ), which also provides a quantitative measure of the power needed to achieve a similar nonlinear effect in different OMF materials. This parameter is defined as follows (Ismaeel et al., 2013):

$$\Gamma = \frac{2\pi}{\lambda} \frac{\bar{n}_2}{A_{eff}} \quad (2.5)$$

where \bar{n}_2 is the average value of the nonlinear refractive index and A_{eff} is the nonlinear effective area, which can be expressed as

$$A_{eff} = \frac{\pi \omega^2}{4} \quad (2.6)$$

Where ω represent the mode spot size (defined as the radius where the normalized intensity has dropped to $1/e^2$). In OMF for weak confinements most of the power is in

the transverse component of the field and the longitudinal field component can approximate as zero. However, For strong confinements near the diffraction limit, a considerable fraction of the power existing the longitudinal field components. Equation 2.6 can still be used to evaluate the OMF nonlinearity provided that the bulk material n_2 is replaced by its average value over an inhomogeneous cross section weighted with respect to the field distribution.

$$\bar{n}_2 = \frac{\varepsilon_0}{\mu_0} k_0 \frac{\int n^2(x, y) n_2(x, y) [2 |e|^4 + |e^2|^2] dA}{\int |(e \times h^*) \cdot \hat{z}|^2 dA} \quad (2.7)$$

where e and h represent the electric and magnetic fields, respectively, and n_2 is the same refractive index used for the bulk material (for example, $2.7 \times 10^{16} \text{ cm}^2 \text{ W}^{-1}$ at $\lambda=1.55 \text{ }\mu\text{m}$ for silica). In addition, a small optical microfiber size not only offers high nonlinearity but is also associated with strong dispersion, and the interplay between these effects has been studied for subwavelength silica fibers. However, an optical fiber manufactured from a highly nonlinear material such as lead silicate, bismuth silicate or chalcogenide glass or a semiconductor such as silicon can possess a value of γ that is enhanced by five times compared with that of silica (Afshar et al., 2009; Ismaeel et al., 2013).

2.2.4 Dispersion

In optical waveguides, dispersion (D) is one of the most significant properties. Dispersion is vital for many nonlinear processes and optical communications systems. An optical microfiber that has been tapered from a standard optical fiber can offer a group velocity dispersion (GVD) that strongly depends on both the core refractive index and the waist diameter of the OMF (Xu et al., 2014). An OMF with a diameter ranging from $5 \text{ }\mu\text{m}$ to $2 \text{ }\mu\text{m}$ can produce a 270 nm shift in the zero-dispersion wavelength. Furthermore, when the waist diameter of the tapered fiber is decreased to $1 \text{ }\mu\text{m}$, the dispersion curve experiences a substantial change, and the relation between the dispersion and the

wavelength is not a monotonic function from 600 nm to 1550 nm. The dispersion of an OMF is given by the following equation:

$$D(\lambda) = -\frac{\lambda}{c} \frac{d^2 n_{eff}}{d\lambda^2} \quad (2.8)$$

where λ is the wavelength, n_{eff} is the effective refractive index and c is the velocity of light in vacuum. The dispersion of a bulk material is measured by Sellmeier's formula.

Figure 2.6 shows the dispersion as a function of the wavelength for different optical microfiber diameters (Tang et al., 2016).

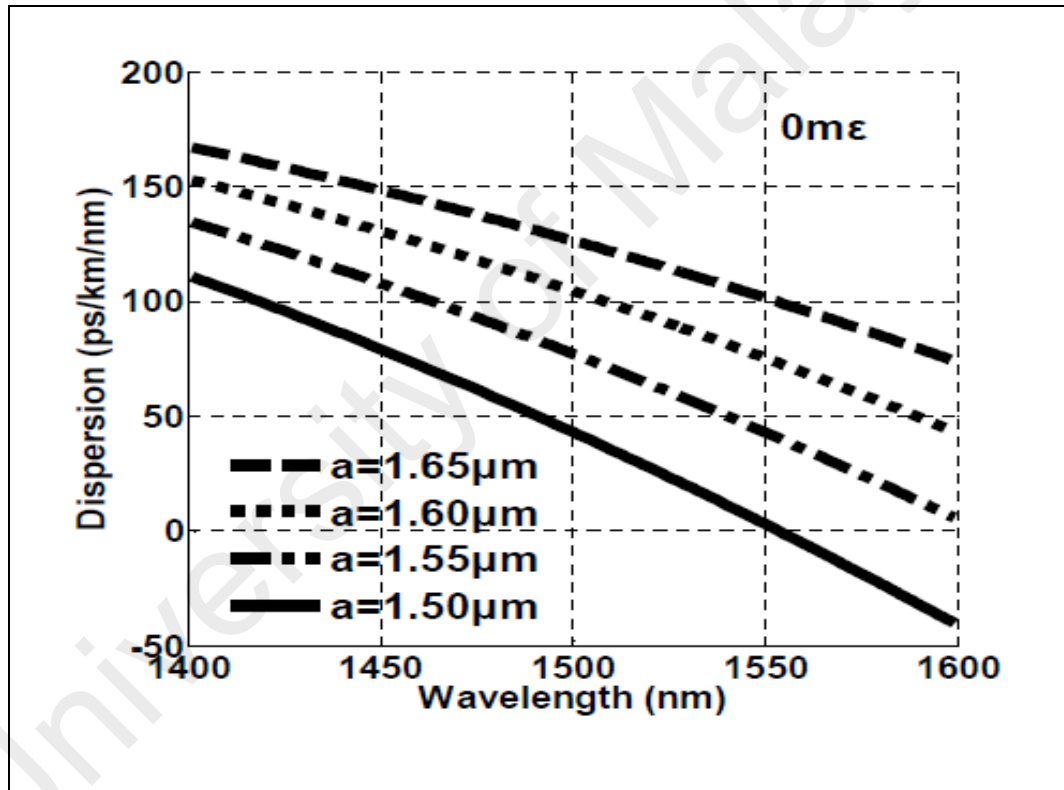


Figure 2.6: Dispersion profiles for elliptical optical microfibers of different diameters (Tang et al., 2016).

Various techniques have been used to control the dispersion of OMFs. An OMF with a nanoscale slot can achieve a low dispersion of ± 10 ps/(nm.km) over a bandwidth in excess of 340 nm (Guo et al., 2011). The dispersion of an OMF for supercontinuum generation can be engineered by immersing the 2.5 μm waist region of the optical microfiber in heavy water (D_2O); thus, the dispersion spectrum is flattened at zero dispersion near 1064 nm, and a 1200 nm broad supercontinuum spectrum (two octaves

broad in frequency) can be obtained by concatenating two tapered fibers with carefully chosen dispersion spectra, pumped by a simple microchip laser (Cordeiro et al., 2005).

2.3 Methods of Fabricating Optical Microfibers

Over the last few years, a variety of techniques have been used to fabricate tapered fibers with diameters ranging from hundreds of nanometers to several microns. The main methods that are widely utilized to fabricate OMFs are detailed below.

2.3.1 Heat-and-Pull Method

The fabrication of low-dimensional optical fibers made from silica using the heat-and-pull approach and studies of their mechanical features were first reported in the twentieth century. However, their optical properties and their applications remained uninvestigated (Méndez & Morse, 2011). A flame-pulling rig is capable of the direct drawing of an OMF with a diameter much lower than that of a standard optical fiber. A typical heat-and-pull system is schematically illustrated in **Figure 2.7**. The setup consists of two movable holders that are used to clamp the optical fiber and to pull on it when the tapering process starts. An OMF can be tapered from either a single-mode fiber or a multimode fiber, and the fiber material can be silica glass or other types of glasses, such as phosphate glass. The heat source is the flame from a torch, and the gas used as the fuel for ignition is either oxy-butane or oxy-hydrogen. The translation stages start to pull the fiber after it has been heated to the glass softening point by the scanning flame. The softening temperature of silica is 1100-1200 °C. By finely controlling the size and speed of the flame to ensure a uniform distribution of heat along the tapered region and moving the translation-stage-mounted holders in opposite directions, the fiber is pulled to obtain a tapered fiber with low loss and a good profile. This technique is also called flame brushing because of the motion of the flame along the tapered fiber. In experimental applications, the ends of the tapered region of the OMF should be connected to standard optical fibers to launch the

light into and/or receive the light from the tapered fiber (Orucevic et al., 2007; Tong & Sumetsky, 2011). Heat-and-pull systems can be designed in three ways depending on how the flame moves to brush the optical fiber. The first type of system uses a stationary flame with stacked pulling stages, the second type uses a stationary flame with independent pulling stages, and the third type uses independent pulling stages and a moving flame (Ward et al., 2014). The flame size and air turbulence must be well controlled to tailor the waist diameter of the OMF. By using a high-purity gas consisting of oxygen and isobutene, a very long OMF with loss of 10^{-2} dB/mm and a waist diameter of 480nm has been reported (Brambilla et al., 2004).

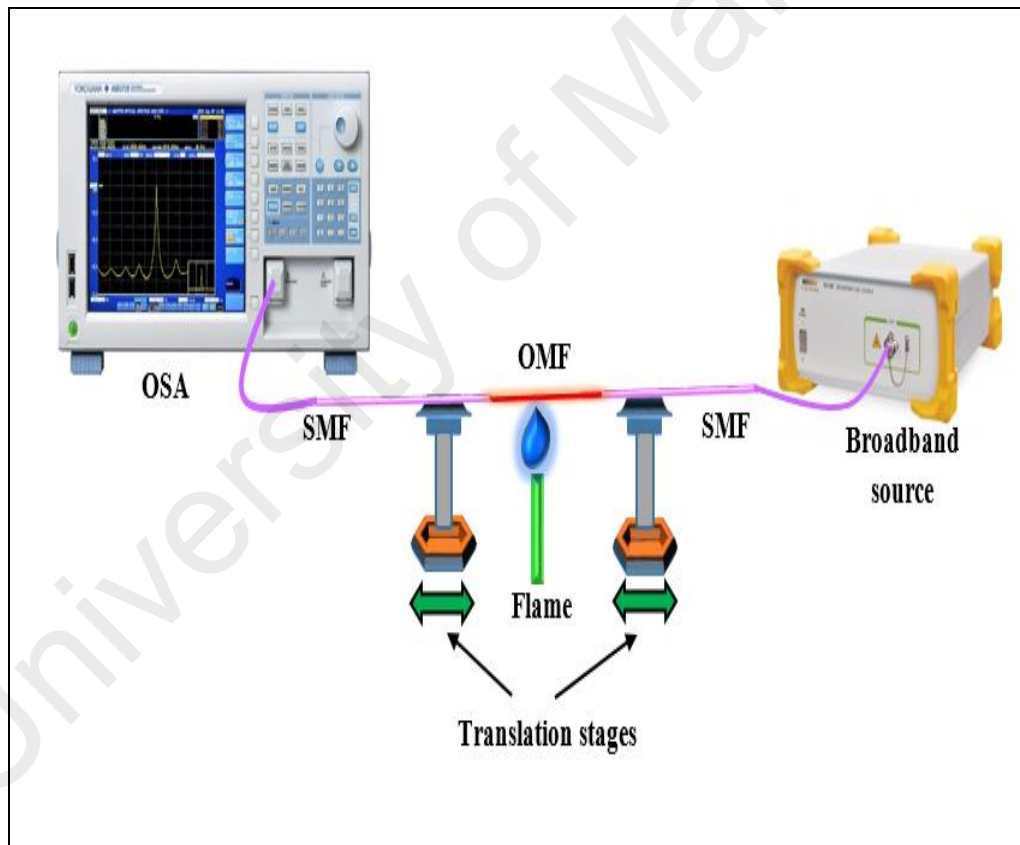


Figure 2.7: Schematic diagram of a heat-and-pull rig.

2.3.2 Microheater Brushing

Based on the heat-and-pull technique, an OMF can be fabricated using a modified flame and pulling system. In this case, a microheater or micro-furnace is used as the heat source to produce the OMF. The temperature of the micro-heater is stable at each point and can be well controlled by adjusting the applied current. In addition, the tapering of an OMF using a thermoelectric microheater circumvents some of the difficulties of standard flame fabrication, such as flame jetting and gas impurities. Ultra-low losses and different OMF shapes can be achieved by varying the pulling speed and the micro-heater temperature (Ding et al., 2010). A lower OH content in tapered optical fibers has been achieved using a graphite micro-heater operating in the temperature range between 200 and 1700 °C (Brambilla et al., 2005). **Figure 2.8** shows a schematic diagram of a thermoelectric microheater setup.

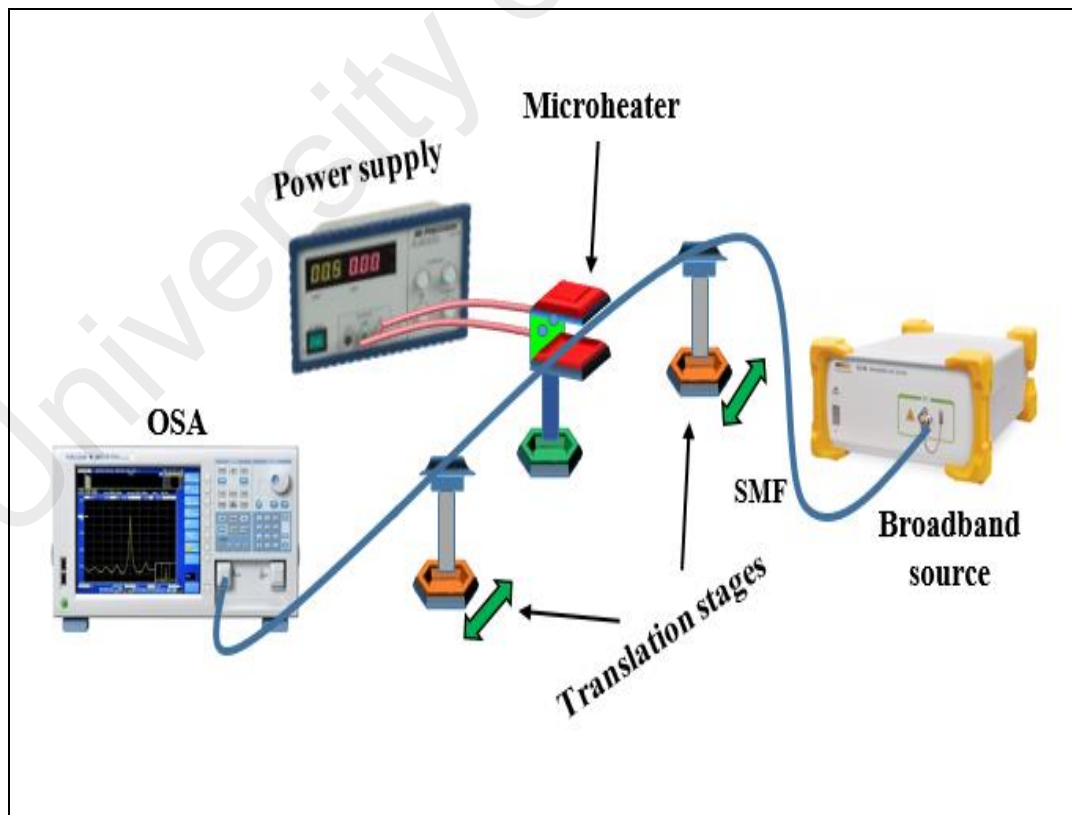


Figure 2.8: Schematic diagram of a heat-and-pull system using a thermoelectric microheater.

2.3.3 Focused CO₂ Laser

This optical fiber tapering system depends on a CO₂ laser beam as the heat source. The many advantages offered by this technique include high stability, facile control, a lack of sensitivity to air currents and other undesired environmental effects, and the ability to precisely control the length of the tapered region. The inner region of the optical fiber will absorb the incident laser beam, thereby heating the fiber, whereas for a flame- or micro-heater-based technique, the process involves heating the fiber's surface. In addition, there is an inverse square relationship between the radius and the heating effect for a CO₂ laser heat source, whereas for a flame heat source, there is simply an inverse relationship between the heating effect and the radius. Silica fibers have a high absorbance efficiency for CO₂ laser radiation (McAtamney et al., 2005; Ward et al., 2006). To obtain a symmetrically tapered fiber, the laser beam needs to be scanned along the fiber, similar to the scanning process applied in the flame-based technique. Using this scheme, the temperature distribution in the optical fiber is evened out both along and perpendicular to its axis. By contrast, if the laser were to be focused at a fixed point, the heat distribution would be even along the axis, but a thermal gradient would exist across the thickness of the fiber, creating an asymmetry between the front and rear surfaces and inducing propagation losses in the taper. A typical optical fiber tapering rig based on a CO₂ laser consists of a CO₂ laser as the heat source, an X-Y galvanometer mirror to create the desired heat zone, and two translation stages for holding and stretching the fiber. **Figure 2.9** illustrates such a typical CO₂-laser-based fiber tapering setup (Ozcan et al., 2007).

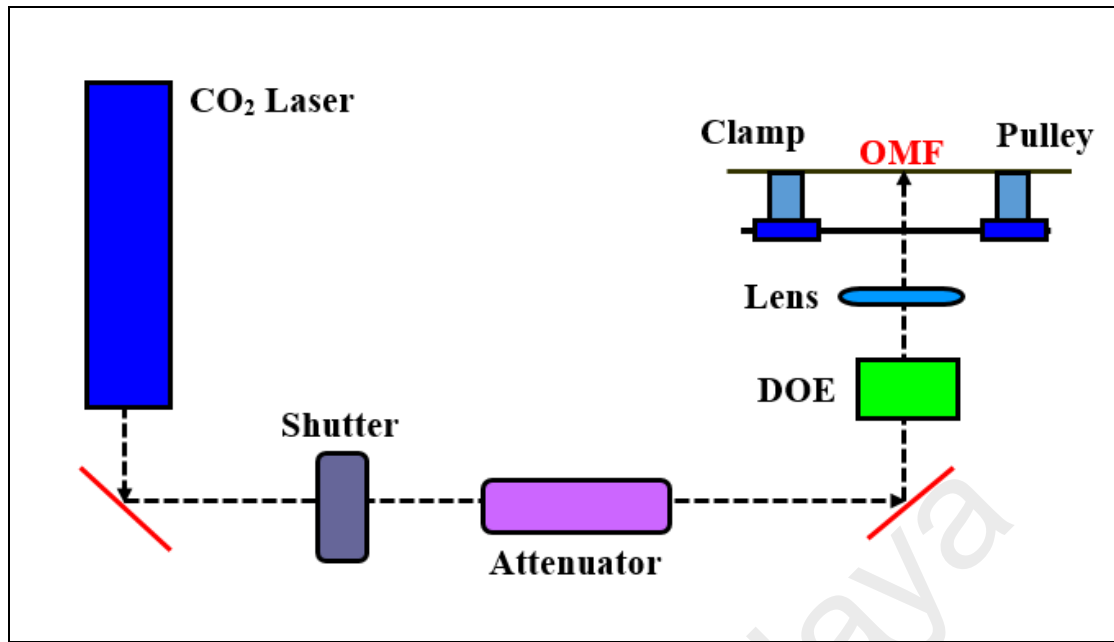


Figure 2.9: Fiber tapering setup based on a focused CO₂ laser (Ozcan et al., 2007).

2.3.4 Etching

The previously reviewed approaches for fabricating a tapered optical fiber are all based on the heat-and-pull technique, with the only difference being the type of heat source used. The second main method of tapering an optical fiber to a sub-micron diameter is by immersing the optical fiber in a chemical solution (hydrofluoric acid) for etching. Although this technique is simple and low in cost compared with other methods, the tapered optical fiber thus generated will have a high loss. In addition, it is difficult to control the desired dimensions of a tapered fiber produced through chemical etching. Generally, the cladding of the optical fiber will be completely removed by the chemical etching process, and the light will be propagated by the core-air interface. By contrast, a tapered optical fiber fabricated using a heat-and-pull technique will maintain its core-cladding structure, and the light will be guided by the entire core-cladding-air system (Haddock et al., 2003b). To reduce the difficulty of achieving the desired diameter of a tapered optical fiber produced through chemical etching, a two-step etching process based on hydrofluoric acid and buffered hydrofluoric acid has been developed and applied, in

which the etching rate in the second step is three times slower than that in the first step; using this process, a 1.1 μm waist diameter has been achieved (Chenari et al., 2016). Fiber tips with cone angles ranging from 3° to 33° have been fabricated by vertically placing an optical fiber in a container of hydrofluoric acid and adjusting the height of the hydrofluoric acid in the container to obtain the desired cone angle. To control the etching rate, several relevant parameters must be considered and controlled during the fiber etching process, including the hydrofluoric acid concentration, the fiber structure and the etching temperature (Nikbakht et al., 2015).

2.3.5 Polishing

One of the benefits of tapering an optical fiber is to permit access to its evanescent field by decreasing or removing the fiber cladding. A mechanical method can be used in which one side of the optical fiber is polished to remove some of the fiber cladding. The structure thus produced is called a D-shaped fiber, because its cross-sectional profile resembles the letter D, or a side-polished fiber. Thus, the evanescent field can be made to interact with the surrounding medium, which is useful in many applications such as sensors, reflectors, couplers and polarizers (Mishakov & Sokolov, 2002). The fractional power distributed in the evanescent field increases as the number of higher-order modes increases. The number of modes that can be supported inside an optical fiber can be described by the V -number using the following equation:

$$V = \frac{2\pi r}{\lambda} \sqrt{n_{co}^2 - n_{cl}^2} \quad (2.9)$$

where λ is the wavelength of the light, r is the radius of the fiber core, and n_{co} and n_{cl} are the refractive indices of the fiber core and cladding, respectively. By contrast, in a D-shaped fiber, the V -number is given as follows:

$$V_D = V_{eff} = \frac{2\pi r_{eff}(d)}{\lambda} \sqrt{n_{co} - n_{cl}} \quad (2.10)$$

where r_{eff} is the radius of the D-shaped fiber, which is related to the side-polished depth of the fiber. This difference in the V -number between an optical fiber and a D-shaped fiber arises from the side-polished core. The side-polished region serves as the core, and the surrounding medium acts as a new cladding (De-Jun et al., 2014b). Generally, to fabricate a D-shaped fiber, an optical fiber is firmly fixed in a V-shaped groove using epoxy glue, and its cladding is ground away for a few millimeters along its length using an aluminum oxide polishing film or a rotating grinding wheel that is precisely controlled by a stepper motor. Alternatively, a CO₂ laser may also be used to fabricate a side-polished fiber (De-Jun et al., 2014b; Qazi et al., 2016a; Qazi et al., 2016b). **Figure 2.10** shows a schematic diagram of a D-shaped fiber.

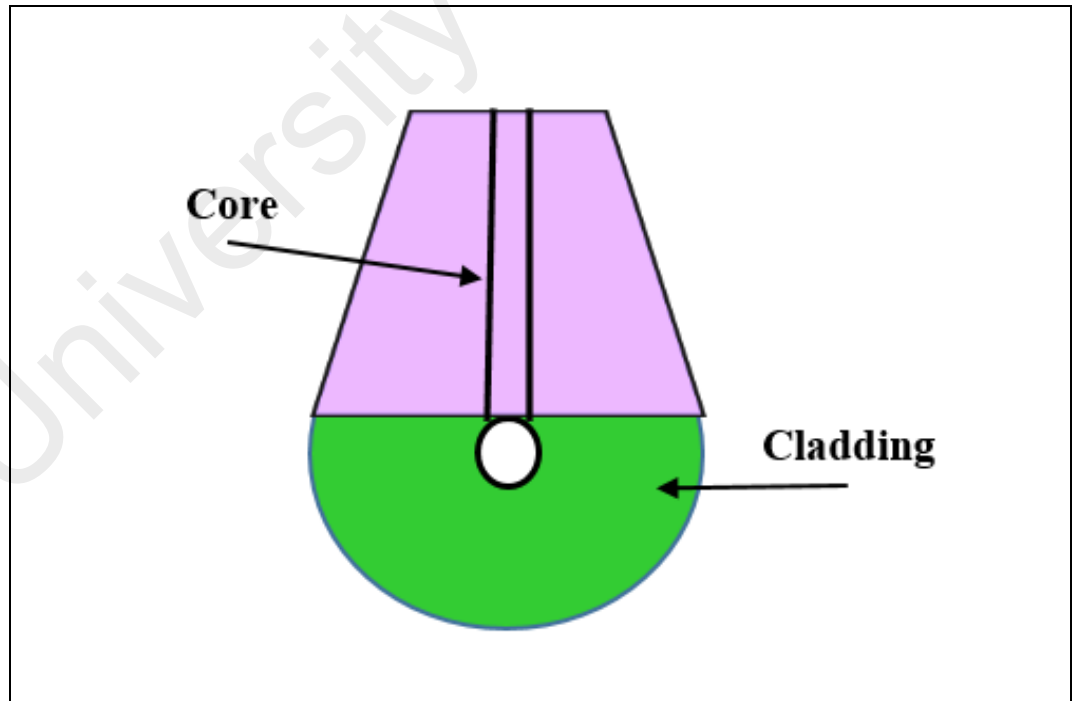


Figure 2.10: Schematic diagram of a D-shaped fiber.

2.4 Guidance of Light Modes Inside an Optical Microfiber

The propagation of light inside an OMF has very important characteristics that strongly depend on the optical microfiber's cross section and taper angle (Love et al., 1991). The tapering of an optical fiber results in a section in which the core and cladding are greatly reduced. The core dimension can be considered negligible, and the light propagates inside the OMF based on the difference in refractive index between the cladding and the surrounding medium. After tapering, the reduced cladding acts as the new core, and the surrounding medium acts as the new cladding of the OMF. In addition, the core dopants are distributed throughout the cross section of the OMF with a uniform concentration. Therefore, an OMF can be regarded as a cylindrical waveguide with a homogeneous refractive index profile (Wang et al., 2015). When light is launched into the OMF, core modes arise that are guided by the cladding/air interface. Maxwell's equations serve as the basic model for analyzing the modes circulating within such a cylindrical submicron fiber. When the fiber is sufficiently long for a spatial steady state to be established, the diameter of the fiber (d) is larger than 10 nm; therefore, the permittivity (ϵ) and permeability (μ) of the bulk material can be used to describe the responses of the dielectric medium to the incident electromagnetic field. **Figure 2.11** shows the basic mathematical model of an OMF, in which n_1 and n_2 are the refractive indices of the optical fiber material and the air, respectively. The index profile of the wave-guiding system can then be expressed as follows (Tong & Sumetsky, 2011):

$$n(r) = \begin{cases} n_1, & 0 < r < a, \\ n_2, & a \leq r < \infty \end{cases} \quad (2.11)$$

where a is the radius of the fiber and n_1 and n_2 are the refractive indices of the fiber material and the air, respectively. The OMF can be considered as a non-dissipative and source-free waveguide because both the fiber material and the cladding medium are

dielectric and are used in the spectral range to which they are transparent. Therefore, Maxwell's equations can be reduced to the following Helmholtz equations:

$$(\nabla^2 n^2 k^2 - \beta^2)e = 0, \quad (2.12)$$

$$(\nabla^2 n^2 k^2 - \beta^2)h = 0$$

where $k = 2\pi/\lambda$ and β is the propagation constant.

The exact solution to this model can be described by the following eigenvalue equations for the electric field distribution (HE_{vm} or EH_{vm}) modes (Wang et al., 2015):

$$\left\{ \frac{J'_v(U)}{U J_v(U)} + \frac{K'_v(W)}{W K_v(W)} \right\} \left\{ \frac{J'_v(U)}{U J_v(U)} + \frac{n_2^2 K'_v(W)}{n_1^2 W K_v(W)} \right\} = \left(\frac{v\beta}{k n_1} \right)^2 \left(\frac{V}{UW} \right)^4 \quad (2.13)$$

For the transverse electric field (TE_{0m}) modes,

$$\frac{J_1(U)}{U J_0(U)} + \frac{K_1(W)}{W K_0(W)} = 0 \quad (2.14)$$

For the transverse magnetic field (TM_{0m}) modes,

$$\frac{n_1^2 J_1(U)}{U J_0(U)} + \frac{n_2^2 K_1(W)}{W K_0(W)} = 0 \quad (2.15)$$

where J_v is the Bessel function of the first kind, K_v is the modified Bessel function of the second kind, $d = 2a$, and

$$U = \frac{d(K_0^2 n_1^2 - \beta^2)^{1/2}}{2}, \quad W = \frac{d(\beta^2 - K_0^2 n_2^2)^{1/2}}{2}, \quad V = \frac{K_0 d(n_1^2 - n_2^2)^{1/2}}{2}$$

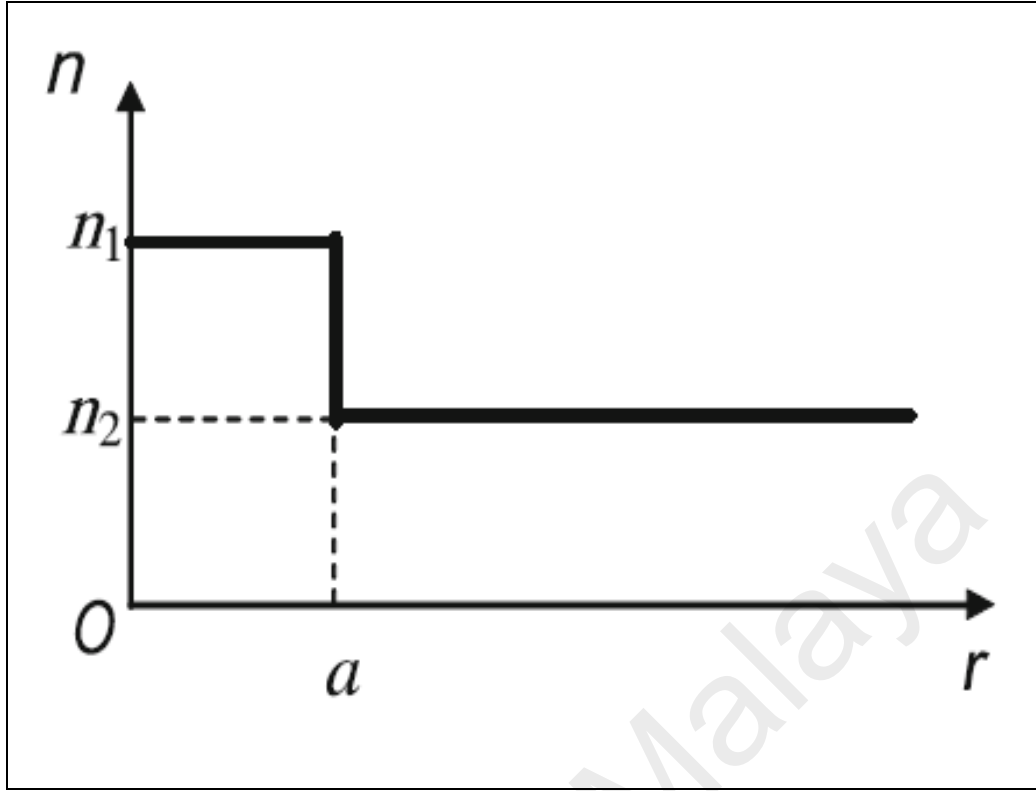


Figure 2.11: Index profile of an air-clad optical microfiber (Tong & Sumetsky, 2011).

The propagation constant for hybrid modes can be calculated by solving Equation 2.13.

The V-number can be expressed as follows:

$$V = \sqrt{U^2 + W^2} \frac{2\pi}{\lambda} \cdot r \cdot NA \quad (2.16)$$

It is known that OMFs exhibit single-mode operation when $V < 2.405$.

2.5 Optical Microfiber Structures

Based on the index to be measured and by virtue of the flexibility, large evanescent fields and strong light confinement of OMFs, many different structures based on OMFs have been proposed and demonstrated. For example, an MLPFG has been reported. The device consisted of a tapered fiber with a waist diameter of approximately $6 \mu\text{m}$ prepared using the heat-and-pull technique; a CO_2 laser beam was focused on and scanned along the microfiber many times in combination with the application of a small longitudinal

tensile strain to produce a grating with a pitch of $\sim 100\text{ }\mu\text{m}$ and 20 periods. The MLPFG was used to experimentally detect temperature and RI, with sensitivities of $-130\text{ pm}/^\circ\text{C}$ and $1900\text{ nm}/\text{RIU}$, respectively (Xuan et al., 2009). LPGs exhibit notch spectra at wavelengths where the light is resonantly coupled from the input fundamental mode to a higher-order cladding mode. This interaction is uniquely strong in MLPFG structures because the input and output modes are both cladding modes and have a strong overlap (Kakarantzas et al., 2001).

Fiber Bragg gratings (FBGs) are very important photonic components that are widely used in various sensing applications. A microfiber FBG (MFBG) can overcome the difficulties of a normal FBG, such as a lack of responsivity to the surrounding medium. To manufacture an MFBG, first, a microfiber should be fabricated. An etching process based on buffered HF acid has been used to reduce the diameter of a commercial FBG to approximately $8.5\text{ }\mu\text{m}$. The thinned FBG thus obtained was applied to detect changes in RI in the range of 1.333–1.450 (Iadicicco et al., 2004). An MFBG has also been fabricated by using a pulsed laser to irradiate a microfiber with a waist diameter of $2\text{--}10\text{ }\mu\text{m}$. The OMF was fabricated using a heat-and-pull system, and the maximum sensitivity achieved was approximately $231.4\text{ nm}/\text{RIU}$ at a RI value of 1.44 for a fiber diameter of $2\text{ }\mu\text{m}$ (Fang et al., 2010). In addition, a focused ion beam system has been utilized to fabricate a compact, all-silica, deeply corrugated first-order FBG for high-temperature sensing. FIB technology is perfect for micro-machining and nano-fabrication because of its small and controllable spot size and high beam current density. A magnified image showing the shape of the fabricated MFBG, with a length and period of $36.6\text{ }\mu\text{m}$ and 61, respectively, is shown in **Figure 2.12** (Kou et al., 2011).

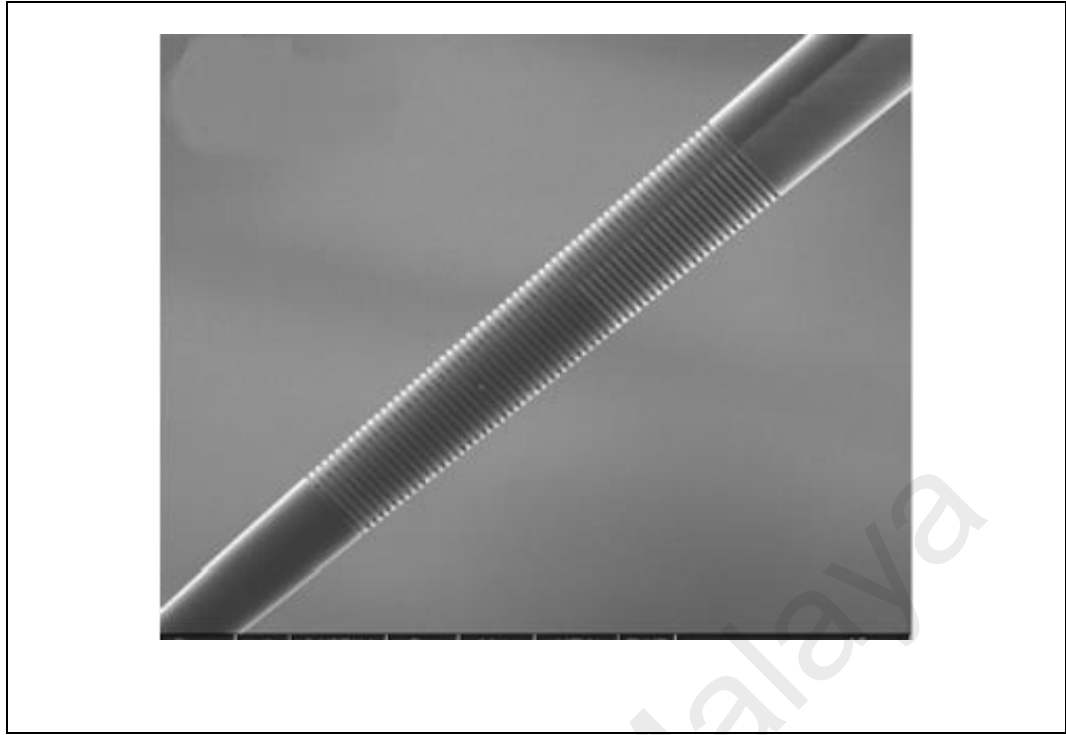


Figure 2.12: Image of an MFBG (Kou et al., 2011).

Moreover, optical-microfiber-based resonators can be created with configurations based on a loop (MLR), knot (MKR) or coil (MCR). These OMF devices have attracted considerable attention because of their ability to function as sensors and filters for optical communications and laser systems (Jiang et al., 2007a; Lim et al., 2012). An MLR is assembled by turning the waist of a biconical taper over on itself. **Figure 2.13 (a)** shows the typical shape of an MLR (Chen et al., 2013). In 2005, Sumetsky et al. demonstrated an MLR with a loop diameter of 2 mm and a Q factor exceeding 15,000, a finesse of ~ 10 and a 100 GHz free spectral range (FSR) (Sumetsky et al., 2005). Another MLR was wrapped around a copper rod for support, with a diameter of approximately 480 μm . The measured Q factor and FSR of this resonator were approximately 4300 and 1.09 nm, respectively. This resonator was utilized as a sensor to detect changes in RI (Guo & Tong, 2008).

A very stable MKR has been assembled by forming a large microfiber loop of approximately a few millimeters in diameter and then tightening the fiber into a small knot by pulling on the free end of the fiber. After this manipulation, a MKR was obtained. This structure was shown to have a Q factor of higher than 50,000, and the FSR could be tuned by changing the MKR diameter (Jiang et al., 2006). **Figure 2.13 (b)** shows an image of an MKR (Chen et al., 2013). With the addition of a copper wire inside the MKR, a current sensor based on this structure has been demonstrated, in which the output wavelength is shifted as a result of thermally induced optical phase shifts attributed to the heat produced by the current flow (Lim et al., 2011)

The last major type of resonator, an MCR, consists of a few turns of microfiber. Such a device has been used as a current sensor, with a monolayer sheet of graphene coating the MCR. The sensitivity was found to be very high, approximately $67.297 \mu\text{m}/\text{A}^2$ (Yan et al., 2015). However, an MCR acts as an all-pass filter that transmits an input pulse very rapidly, leaving it unchanged, when the input wavelength is far from the MCR's resonance, whereas it traps light inside it when operating under a resonance condition (Kowsari et al., 2016). A high Q factor of approximately 5×10^5 and an extinction ratio of ~ 10 dB were achieved when an MCR was packaged with polydimethylsiloxane ($n \sim 1.402$) (Lu & Wang, 2015). **Figure 2.13 (c)** illustrates the structure of an MCR (Chen et al., 2013).

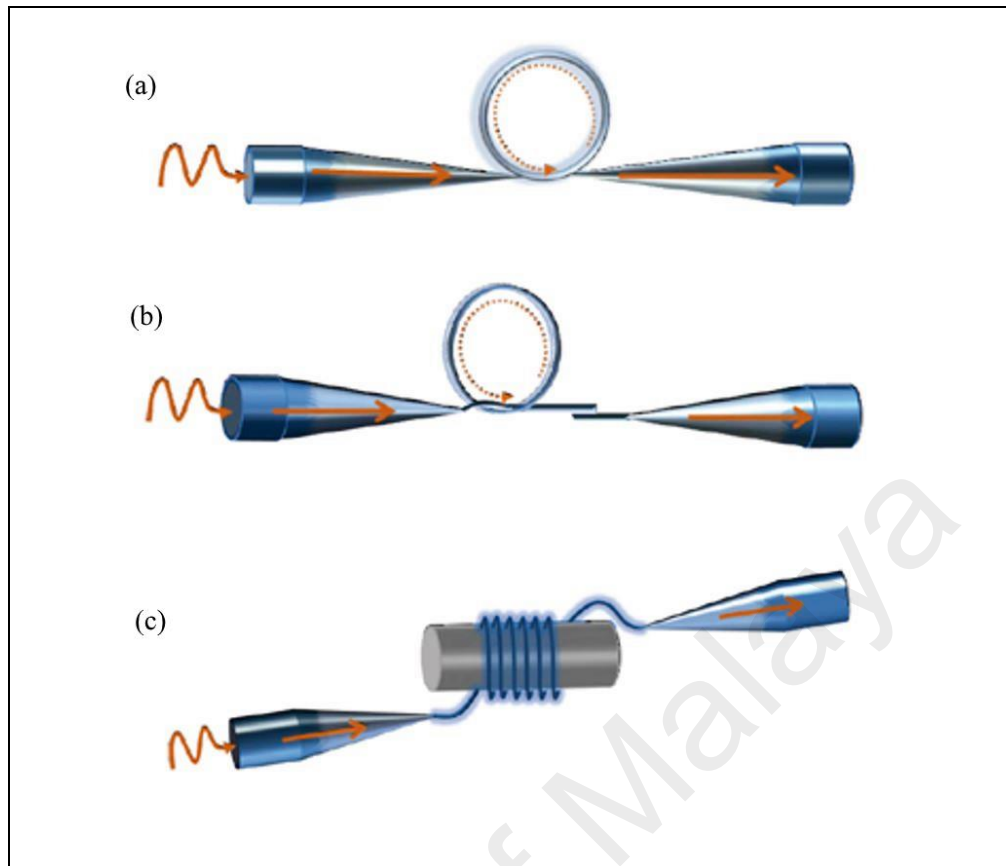


Figure 2.13: Schematic illustrations of optical microfiber resonators:(a) an MLR,(b) an MKR and (c) an MCR (Chen et al., 2013).

Microfiber interferometers are structures that are fabricated from tapered optical fibers. The most important types of optical-microfiber-based interferometers are MZIs, MIs and Fabry-Pérot interferometers (FPIs). OMF interferometers have been widely used in sensing applications for the detection of various parameters in the fields of biology, chemistry and physics (Han et al., 2014). The fundamental operating principle for microfiber MZIs of all shapes is based on splitting the input light beam into core and cladding modes, which have different optical paths because of mode dispersion, and then recoupling them later to produce an interferometric spectrum (Lee et al., 2012; Wen et al., 2015). **Figure 2.14** shows schematic diagrams of two types of MMZIs. Meanwhile, an MI setup consisting of a single tapered fiber region terminated by a ~500 nm thick gold coating has been used as RI sensor. This device had a low insertion loss of 1 dB and an extinction ratio of 13 dB (Tian et al., 2008). A microfiber FPI has been proposed and

applied for use as a radio-frequency interrogated RI sensor. The device consisted of a normal FBG that had been tapered with a uniform waist of about $1.3\ \mu\text{m}$ diameter at the center of the FBG via the heat-and-pull technique. This FPI could detect ambient RI changes in a range of 1.334 to 1.4 with a sensitivity of 911 MHz/RIU (Zhang et al., 2012).

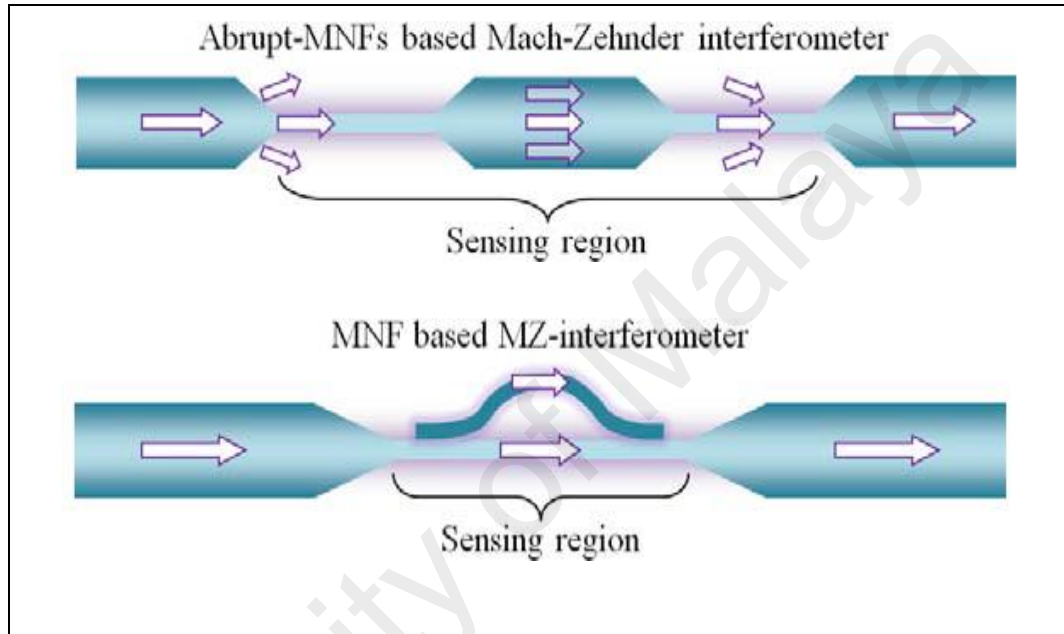


Figure 2.14: Schematic diagram of two structures of microfiber MZIs (Chen et al., 2013).

2.6 Geometric Classification of Optical Microfibers

The shape of an OMF that has been fabricated based on the heat-and-pull technique is determined by fabrication conditions such as the pulling speed, the heating zone radius and the flame temperature. OMFs can be classified based on their profiles into two main groups, biconical and irregular.

2.6.1 Biconical Optical Microfibers

An OMF is called biconical or adiabatic when the majority of the power remains in the fundamental mode (LP_{01}) and does not couple to higher-order modes as it propagates

along the taper. This condition is satisfied when the taper angle is small (Zibaii et al., 2010). **Figure 2.15** shows the profile of a biconical microfiber, where z denotes the position along the microfiber. Theoretically, an adiabatic tapered fiber operates based on the condition that the beat length between the fundamental mode LP_{01} and the second local mode is smaller than the local taper length scale, z_t .

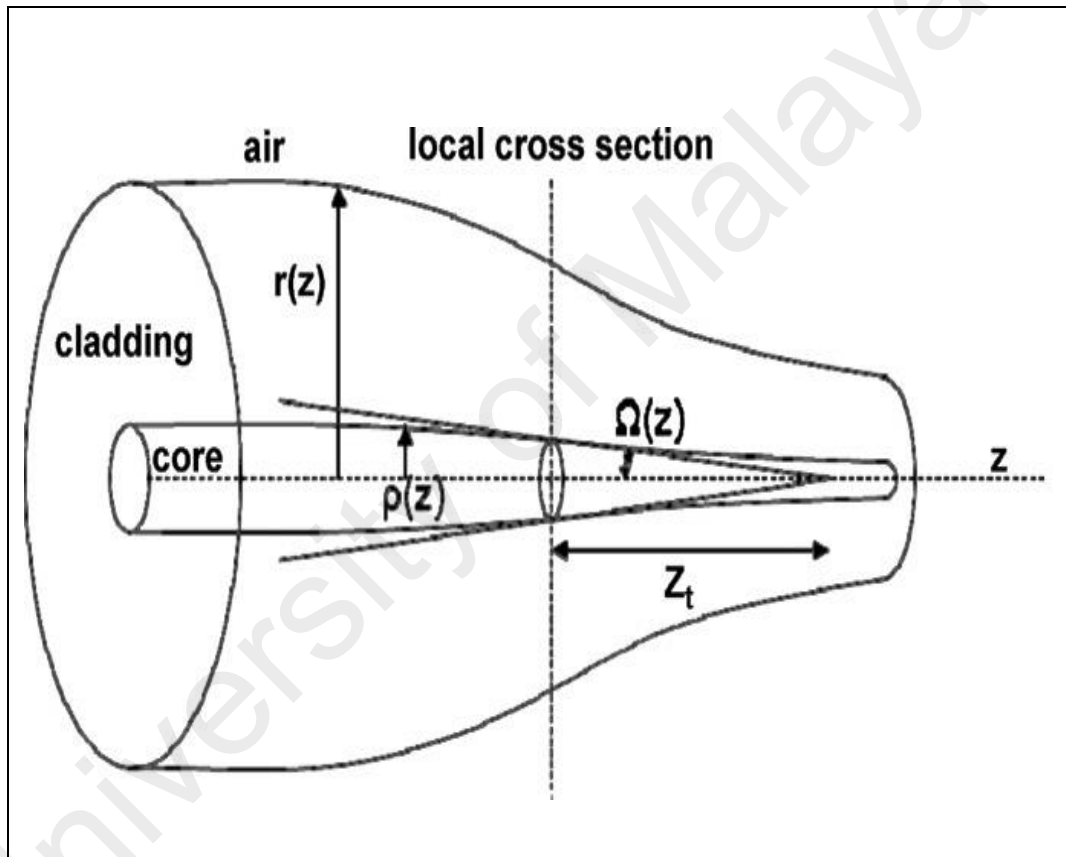


Figure 2.15: Schematic illustration of a biconical optical microfiber profile (Harun et al., 2013).

$$z_b < z_t \quad (2.17)$$

$$z_t = \frac{\rho}{\tan \Omega} \quad (2.18)$$

where $\rho = \rho(z)$ is the local core radius and $\Omega = \Omega(z)$ is the local taper angle. The beat length between the two modes is expressed as

$$z_b = \frac{2\pi}{\beta_1 - \beta_2} \quad (2.19)$$

where $\beta_1 = \beta_1(r)$ and $\beta_2 = \beta_2(r)$ are the propagation constants of the fundamental mode and the second local mode, respectively. From the above equations, the following inequality can be derived for the tapered fiber:

$$\left| \frac{d\rho}{dz} \right| = \tan \Omega < \frac{\rho(\beta_1 - \beta_2)}{2\pi} \quad (2.20)$$

where $\left| \frac{d\rho}{dz} \right|$ is the rate of change of the local core radius and its magnitude is equal to $\tan \Omega$. The inequality expressed in Equation 2.20 can be rewritten as a function of the local cladding radius $r = r(z)$ as follows:

$$\left| \frac{dr}{dz} \right| < \frac{r(\beta_1 - \beta_2)}{2\pi} \quad (2.21)$$

To achieve a balance between the taper length and the rate of diameter reduction, a factor f is introduced into the inequality function expressed by Equation 2.21, which yields

$$\left| \frac{dr}{dz} \right| < \frac{fr(\beta_1 - \beta_2)}{2\pi} \quad (2.22)$$

where the value of f can be chosen to lie between 0 and 1. The optimal microfiber profile is achieved at $f = 1$. In practice, a tapered fiber with negligible loss can be achieved with $f = 0.5$, but the transition length of such a tapered fiber will be twice as long as that of the optimal tapered fiber. When a silica optical fiber is heated, its volume is marginally

increased because of thermal expansion. However, the change in volume is negligibly small not to mention that the volume expansion wears off very quickly once the heat is dissipated from the mass, it is reasonable to assume that the total volume of the heated fiber is conserved throughout the entire tapering process. A straightforward mathematical analysis is presented to investigate the relationship between the shape of the tapered fiber, the elongation distance and the hot-zone length. **Figure 2.16** shows the shapes of the optical fiber before and after heating. At time = t , the section between A and B represents the equivalent hot-zone length of the heated fiber, L , and the radius of the microfiber waist, r . After a short interval of time δt , the heated fiber is stretched, the length is extended to $L + \delta x$, and the radius of the heated fiber becomes $r + \delta r$.

$$(r + \delta r)^2 (L + \delta x) = \pi r^2 L \quad (2.23)$$

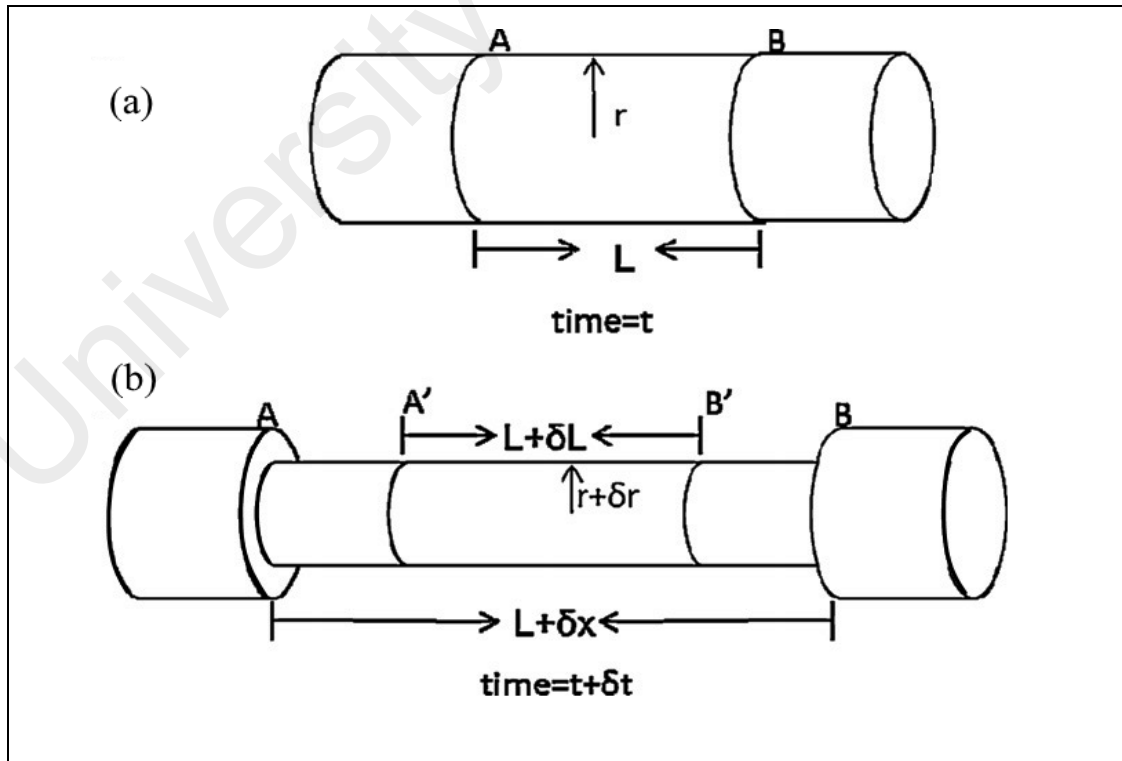


Figure 2.16: The shapes of a standard optical fiber (a) before heating and (b) after the heat-and-pull process (Harun et al., 2013).

After some algebraic manipulations, a differential equation can be derived from Equation 2.23 as follows:

$$\frac{dr}{dx} = -\frac{r}{2L} \quad (2.24)$$

The function describing the radius profile is given by the integral

$$r(x) = r_0 \exp\left(-\frac{1}{2} \int \frac{dx}{L}\right) \quad (2.25)$$

where r_0 denotes the initial radius of the fiber. To relate the varying hot-zone length L to the elongation distance x during the tapering process, L can be replaced with any function of x , such as a linear function:

$$L(x) = L_0 + \alpha x \quad (2.26)$$

Where L_0 is the initial value of L

By substituting Equation. 2.26 into Equation 2.25, we obtain

$$r(x) = r_0 \exp\left(-\frac{1}{2} \int \frac{dx}{L_0 + \alpha x}\right) \quad (2.27)$$

$$r(x) = r_0 \left(1 + \frac{\alpha x}{L_0}\right)^{-1/2\alpha} \quad (2.28)$$

To relate the elongation distance x to the position of the taper transition z , another equation can be derived by referring to the model depicted in. **Figure 2.17**. In **Figure 2.17 (a)**, L_0 denotes the initial hot-zone length bounded by the cross sections P and Q of the fiber, whereas x denotes the elongation distance. It is considered that the heated fiber is elongated to form a biconical shape.

This elongation results in two identical taper extensions on both sides of the hot zone, each of length $x/2$. After tapering for a certain period of time $= t$, P and Q have been separated from each other by an extension distance of x , and the length of the taper waist is L . Based on the above description, the following equation is obtained:

$$2z + L = x + L_0 \quad (2.29)$$

where $L = L(x)$. Substituting Equation. 2.27 into Equation 2.26 yields

$$r(z) = r_0 \left(1 + \frac{2\alpha z}{(1-\alpha)L_0} \right)^{-1/2\alpha} \quad (2.30)$$

where α is a constant that varies from -1 to 1.

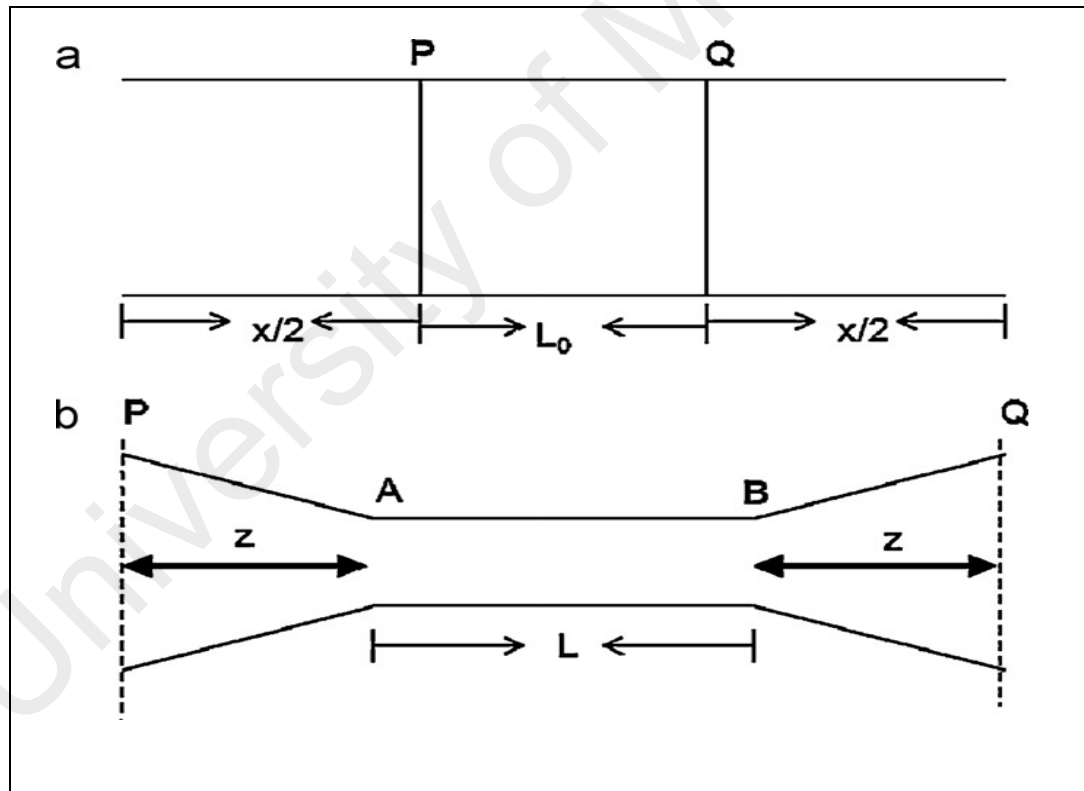


Figure 2.17: The profiles of an optical fiber (a) before tapering and (b) after tapering (Harun et al., 2013).

OMFs of various shapes can be obtained by changing the value of α ; such shapes include a reciprocal curve ($\alpha = 0.5$), an exponentially decaying curve ($\alpha = 1$), a linear curve ($\alpha = -0.5$) and a concave curve. **Figure 2.18** shows the profile of an optical microfiber with $\alpha = 1$ and $L_0 = 10$ mm. The function for an exponentially decaying profile is given by (Birks & Li, 1992; Harun et al., 2013)

$$r(z) = r_0 e^{-z/L_0} \quad (2.31)$$

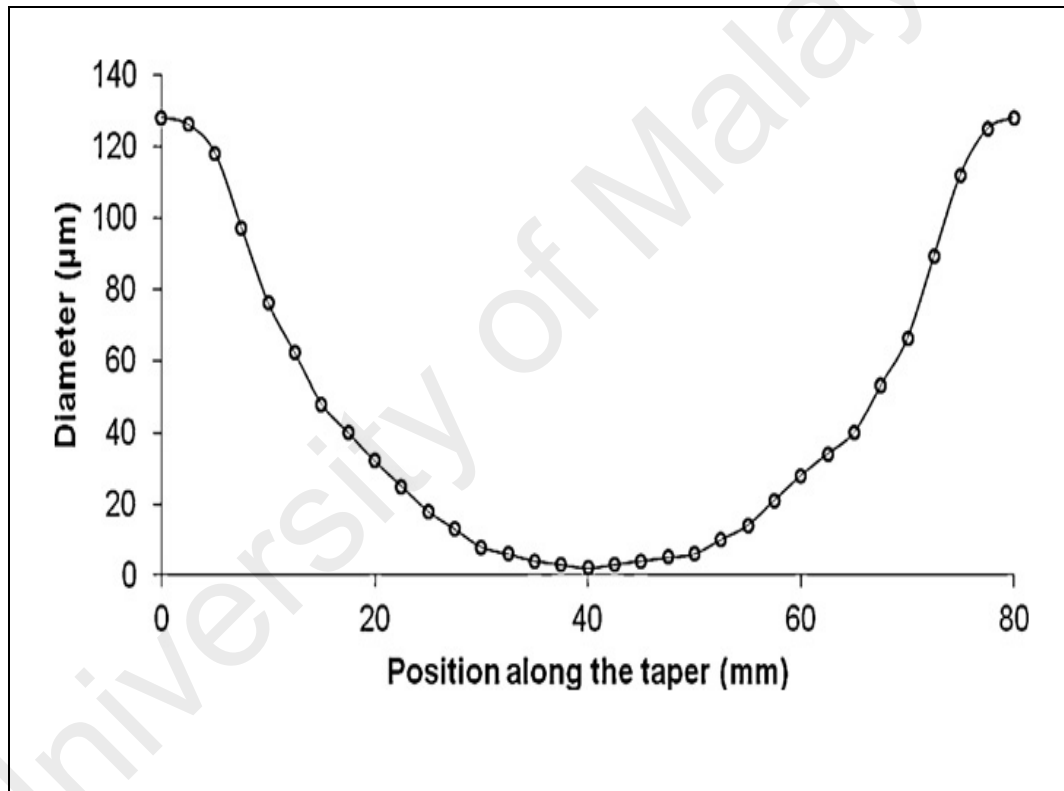


Figure 2.18: Profile of an optical microfiber with $\alpha=1$ and $L_0=10$ mm (Harun et al., 2013).

2.6.2 Abrupt Optical Microfibers

In contrast to a biconical tapered fiber, an abrupt or nonadiabatic tapered fiber has an abrupt taper angle and can serve as a multimode interferometer because of coupling between the fundamental mode and higher-order modes, mainly LP_{01} and LP_{02} . A

nonadiabatic tapered fiber can support more than one mode because of the large difference in refractive index between the cladding of the OMF and the surrounding medium (Zibaii et al., 2010). The modal interference can be mathematically expressed as (Ji et al., 2012)

$$I = I_1 + I_2 + 2\sqrt{I_1 I_2} \cos \phi \quad (2.32)$$

where I_m ($m=1,2$) is the power coupling between the fundamental mode and the HE_{1m} mode and ϕ is the phase difference between the two modes. For a uniform beating region, the latter takes the form of

$$\phi = \Delta\beta L \quad (2.33)$$

where L is the length of the beating region and $\Delta\beta$ is the difference between the propagation constants of the two modes, which can theoretically be expressed as

$$\Delta\beta = \frac{\lambda (U_2^{\infty 2} - U_1^{\infty 2})}{4\pi n_{cl} \rho^2} \exp\left(-\frac{2}{V}\right) \quad (2.34)$$

where V represents the normalized frequency, expressed as

$$V = \frac{2\pi\rho}{\lambda} \sqrt{n_{cl}^2 - n_{ext}^2} \quad (2.35)$$

where n_{cl} is the refractive index of the fiber cladding, n_{ext} is the refractive index of the external medium, λ is the wavelength of the light, ρ is the radius of the taper waist, and U_1^{∞} and U_2^{∞} are the asymptotic values of the U parameters of the two modes. The FSR can also be locally defined as a function of wavelength as follows:

$$FSR(\lambda) = \frac{2\pi}{d\phi/d\lambda} = \frac{8\pi^2 \rho^2 n_{cl}}{L(U_2^{\infty 2} - U_1^{\infty 2}) \exp\left(-\frac{2}{V}\right) \left(1 - \frac{2}{V}\right)} \quad (2.36)$$

From Equations 2.33, 2.34 and 2.35, the wavelength shift due to the change of external refractive index can be derived as (Luo et al., 2014):

$$\Delta\lambda_m = \lambda \times \left[\exp\left(\frac{2}{V_i} - \frac{2}{V_j}\right) - 1 \right] \quad (2.37)$$

where the revised normalized frequency V_{ij} is expressed as in the following equation:

$$V_{ij} = \frac{2\pi d}{\lambda} \sqrt{n_{cl}^2 - n_{ambient\ i,j}^2} \quad (2.38)$$

Where d is the equivalent diameter of OMF, V_i and V_j represent the normalized frequencies of OMF with the ambient RI of $n_{ambient\ i}$ and $n_{ambient\ j}$, respectively. It is noticed that, the responsivity of an OMF operating as a sensor can be increased by increasing the RI of the external medium or by decreasing the diameter of the microfiber.

2.7 Optical Microfiber Applications

OMFs have been used for various applications, which can be grouped into two main categories based on the function of the OMF in the experimental system.

2.7.1 Optical-Microfiber-Based Sensing

OMFs are beneficial for practical detection applications because of their evanescent fields. The detection of changes in RI is very significant for applications in various fields, including biomedical, chemical, and environmental applications as well as food safety technology (De-Jun et al., 2014a). An ultracompact nanofiber MZI with a diameter of 700 nm was manufactured from poly trimethylene terephthalate, a polymer material, to quantify the RI changes in glycerol solutions of different concentrations. The achieved responsivity of this device was 1100 nm/RIU within an RI range of 1.34 - 1.39 (Wang et al., 2014). To enhance the RI detection limit, a cascade MKR (CMKR) with a Vernier effect can be utilized as a RI sensor. A CMKR was fabricated by connecting two MKRs

(MKR₁, MKR₂), with two knotting turns in each coupling region, via a tapered fiber bus. The ambient RI of MKR₂ was increased from 1.3315 to 1.3349 by injecting pure glycerin, at 1 ml each time, while the ambient RI of MKR₁ was kept at 1.3315, and the shifting of the output spectra of the CMKRs toward longer wavelengths was traced and recorded. The sensitivity of this sensor was 6523 nm/RIU (Xu et al., 2015). In addition, a single tapered fiber, with three different waist length samples, was used to investigate the shifting of the output spectrum due to the change in concentration of the ambient medium (gelatin). The measured responsivity was 2.4214 nm/% W/V (Yadav et al., 2014).

OMFs have been demonstrated to be applicable for measuring the temperatures of air, hot plates and liquids. Sea water temperatures have been identified using a microfiber knot resonator based on the thermo-optical effect. This sensor had a tapered microfiber diameter ranging from 2.30 to 3.91 μm , and the maximum sensitivity was 22.81 pm/ $^{\circ}\text{C}$ (Yang et al., 2014). A multimode microfiber Mach-Zehnder interferometer (MMZI), with a length of 12 mm and a 11.24 μm waist diameter, was used as a temperature sensor by tracing and recording the shift toward longer wavelengths of two dips in the optical spectrum. The sensor achieved sensitivities of -0.193 nm/ $^{\circ}\text{C}$ and 0.239 nm/ $^{\circ}\text{C}$ for dip 1 and dip 2, respectively (Luo et al., 2014). To date, various OMF structures have been used as temperature sensors, such as a tapered microfiber coated with polydimethylsiloxane, which achieved a temperature sensitivity of 3101.8 pm/ $^{\circ}\text{C}$ (Hernández-Romano et al., 2015), and a gourd-shaped microfiber with a sensitivity of 17.15 pm/ $^{\circ}\text{C}$ in the range of 30-390 $^{\circ}\text{C}$ (Xian et al., 2016). A high sensitivity of 41 pm/ $^{\circ}\text{C}$ in a temperature range up to 1100 $^{\circ}\text{C}$ has been achieved using an ultra-compact microfiber sensor head based on inner air cavity (Liao et al., 2014).

A humidity sensor based on an OMF has been proposed. A simple tapered microfiber was fabricated with a waist diameter of 1.2 μm to probe the changes in relative humidity.

The humidity-sensing principle was based on the change in the RI of the OMF due to the absorbance of water molecules. This sensor had a sensitivity of 97.76 pm/%RH (Tan et al., 2013). Another OMF was tapered from a plastic optical fiber (POF), and a layer of agarose gel was then deposited on the waist region. The proposed sensor achieved a sensitivity of 0.0228 mV/%, with a slope linearity of more than 98.36% and a limit of detection of 0.927% (Batumalay et al., 2014a). The sensitivity of a similar detector was enhanced by coating a POF with seeded ZnO nanoparticles, yielding a sensitivity of 0.0258 mV/% with a slope linearity of more than 95.48% and a detection limit of 0.143% (Batumalay et al., 2015).

Recently, tapered OMFs have been used as current sensors. In such a sensor, the current flow around the OMF induces a temperature change that changes the effective RI of the microfiber and shifts the dip wavelength. A MCR was wrapped around a thin rod of chromium-nickel (CrNi) with diameters of 50 μm and 80 μm . The measured responsivity of this device when the applied current ranged from 0.0 to 0.12 A was 220.65 nm/A² (Xie et al., 2014). Both the resistivity and diameter of the rod were very effective in tuning the level of microfiber sensitivity; lower sensitivity values were achieved using copper wire with an MKR (Lim et al., 2011) and an MMZI (Sulaiman et al., 2012).

The sensing of magnetic fields based on OMFs has been widely studied because of their small size and their ability to be integrated with many functional materials. Magnetic fluids are stable colloidal suspensions of ferromagnetic nanoparticles in certain suitable liquid carriers. The nanoparticles form chains along the magnetic field direction under an external magnetic field. Such fluids have highly tunable optical properties, such as the magneto-optical effect, RI, birefringence, magneto chromatic characteristics and nonlinear optical effects (Miao et al., 2013). A magnetic field sensor based on the interaction of the evanescent field of a nonadiabatic microfiber with a magnetic fluid has

been experimentally demonstrated, where the nonadiabatic microfiber acts as the core and the magnetic fluid acts as the cladding in this sensor. Moreover, when the external magnetic field changes, the RI of the magnetic fluid will change, causing a shift in the output interference spectrum. A sensitivity of -7.17×10^{-2} nm/mT was reported for an increase in the external magnetic field intensity from 0 to 44 mT (Layeghi et al., 2014).

Only limited studies have been conducted on strain-sensing applications of OMFs compared with the applications discussed above. A nonadiabatic OMF has been employed to detect applied strain. A responsivity of 4.2 pm/ μm was recorded (Muhammad et al., 2013). Moreover, a biconical microfiber with a diameter of 2.5 μm has been used for strain measurements. The sensitivities of this structure for strain and elongation were 4.84 pm/ μe and 404 pm/ μm , respectively (Li et al., 2014). In 2013, Liao et al. fabricated a compact IMMZI with an inner air cavity section for strain-sensing measurements. The highest strain sensitivity achieved was 6.8 pm/ μe , corresponding to the inner air cavity length of 860 μm (Liao et al., 2013).

2.7.2 Optical-Microfiber-Based Photonics

An OMF can function as a free-standing or supported waveguide because of its advantageous properties such as a large evanescent field, strong light confinement and ease of configuration. Because of these properties, OMFs have been used as essential components in photonic devices and circuits based on OMFs. It has been reported that four-wave mixing can be induced by attaching a graphene film to an OMF of 2 μm in diameter and 70 mm in length. With two continuous pump beams, the conversion efficiency varies from -28 to -34 dB as the wavelength difference between the two pump lasers varies from 0.5 to 4.5 nm (Wu et al., 2014). Moreover, narrowband UV frequencies have been produced via four-wave mixing using OMFs (Khudus et al., 2016).

Supercontinuum generation sources have been used in many applications, such as optical coherence tomography, spectroscopy, frequency metrology and wavelength division multiplexing (WDM) (Xu et al., 2009). Supercontinuum generation based on OMFs has been used in many studies. An octave-spanning supercontinuum has been generated with 250 pJ pulses from a femtosecond mode-locked Ti:sapphire oscillator by means of a tapered fiber with a sub-wavelength diameter of approximately 600 nm. In this system, the high normal group velocity dispersion (GVD) toward longer wavelengths was responsible for the sharp cutoff of the continuum at these wavelengths (Foster & Gaeta, 2004). OMFs fabricated from standard optical fibers and photonic crystal fibers have separately been used to generate single-mode supercontinua that are sufficiently broad to fill the visible spectrum without spreading far beyond it (Leon-Saval et al., 2004). In 2005, Foster et al. investigated the reduction of the diameter of an optical fiber to shift the generated supercontinuum generation into the blue region. In addition, they found that the geometry of an OMF has a strong influence on its spectral features (Foster et al., 2005).

OMFs can also be used as tunable bandpass filters, which are very important for filtering out noise and unwanted signals in optical communications systems. A substrate of MgF₂ of 1 mm in thickness was used to support an OMF with a 1 μ m waist diameter, where van der Waals and electrostatic forces attracted the OMF to the substrate. By controlling the interaction length of the OMF with the MgF₂, the cutoff wavelength could be tuned over a range of 400 nm, from the visible region to the infrared region (Chen et al., 2008). A biconical OMF coupler has also been demonstrated. The waist diameter in the coupling section was 1.5 μ m, and the device was operated based on a combination of the fabrication technique for fused-fiber couplers and the higher-order filtering characteristics of sub-wavelength-diameter optical wires. The output spectrum of a single mode ranged over a wide wavelength region between 400 nm and 1700 nm, and the output

power was efficiently divided at a ratio of 50:50 (Jung et al., 2009). **Figure 2.19** shows a schematic illustration of the microfiber coupler.

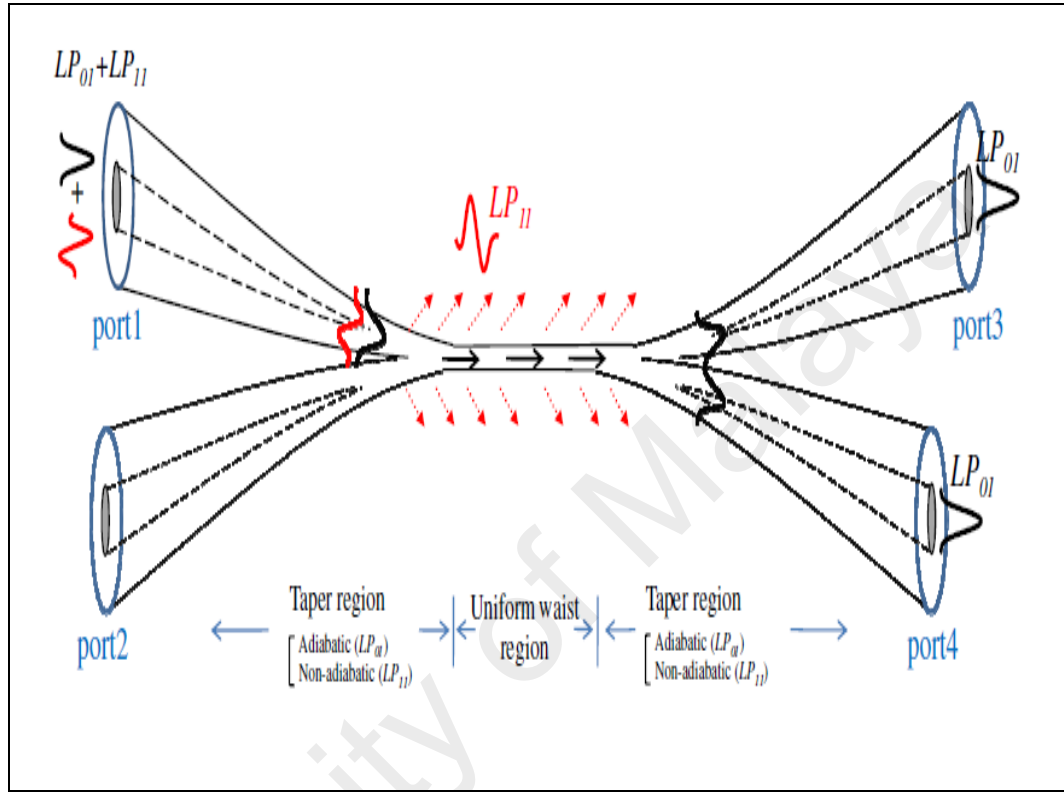


Figure 2.19: Schematic illustration of an optical microfiber coupler (Jung et al., 2009).

2.8 Pulsed Fiber Lasers Based on Optical Microfibers

Pulsed fiber lasers have attracted the interest of many researchers over the past decade because of their wide array of applications in many fields, such as spectroscopy, medicine and optical communications. Based on different materials and structures, pulsed lasers can be fabricated using various SAs, SESAMs and nonlinear polarization rotation (NPR). By virtue of their unique properties, OMFs have been used as low-loss waveguides with large evanescent fields for the generation of passive Q-switched and mode-locked pulsed lasing with the assistance of passive SA materials. Compared with the direct interaction of light with an SA on the face of a fiber ferrule, the interaction of a saturable absorber

with the evanescent field of an OMF offers many advantages, such as a long interaction length and a high thermal damage limit (Khazaeinezhad et al., 2015). CNTs have been deposited around an OMF with a diameter of 6 μm to realize a passively mode-locked fiber laser. The OMF was immersed in a CNT-dispersed dimethylformamide (DMF) droplet on a slide glass and was simultaneously injected with light from a laser diode at a wavelength of 1560 nm and at -10 dBm; the optical power fed into the microfiber was amplified to 13 dBm by an EDFA. The laser output had a bandwidth of 3.7 nm and a pulse duration of 1.14 ps at a 1.54 MHz repetition rate (Kashiwagi & Yamashita, 2009). Moreover, a CNT solution has been deposited on the surface of a side-polished fiber. Because of the interaction between the CNT SA and the evanescent field of the D-shaped fiber, this photonic device could produce a Q-switched pulse train with an energy of 81.3 nJ, a repetition rate of 70.4 kHz and a pulse width of 4.5 μs (Liu et al., 2013a). A polarization-sensitive SA has been fabricated by wrapping an OMF in a coil shaped around a graphene-coated rod. By fixing the input power, stable Q-switched and mode-locked pulses with a rectangular shape could be obtained (Li et al., 2016). In addition, graphene can provide both saturable absorption and nonlinear effects when it is deposited on an OMF. Optical rogue waves have been generated in a passively mode-locked EDF laser by incorporating a graphene-decorated microfiber photonic device into the cavity. The microfiber had a diameter of 8 μm (Cai et al., 2017). Meanwhile, a topological insulator SA, which exhibits a Dirac-like linear band dispersion similar to that of graphene, has been deposited on a microfiber that had been tapered down to 12 μm to generate harmonic mode-locking behavior. The pulses had a repetition rate of 2.04 GHz at a pump power of 126 mW (Luo et al., 2013).

2.9 Multi-wavelength Erbium-Doped Fiber Lasers Based on Optical Microfibers

Multi-wavelength lasers have been a concept of significant importance since the discovery of the lasing phenomenon, and they have been used in various applications, such as optical communications systems, remote sensing devices, laser ranging, topography and medicine (Walsh, 2010). Various techniques have been used to produce multi-wavelength lasers, such as FBGs (He et al., 2009), photonic crystal fibers (PCFs) (Ahmad et al., 2013) and double-ring filters (Yeh et al., 2007). However, these conventional methods are subject to certain disadvantages, such as complicated manufacturing processes and high costs. By virtue of their significant properties as previously mentioned in this thesis, OMFs are potential candidates for serving as selective elements in laser cavities for the generation of dual and multiple wavelengths. To produce a dual-wavelength laser, a MZI-based tapered fiber has been fabricated and utilized as a comb filter inside an EDF laser cavity. In addition, it was observed that the dual wavelengths could be tuned by bending the MZI (Ali et al., 2014). Moreover, a compact double knot resonator with diameters of 146.1 and 223.6 μm has been employed to produce tunable dual wavelengths. This two-emission-line laser had a 2 kHz linewidth and an optical side-mode suppression ratio of over 31 dB. By changing the length of the coupling region and the relative positioning of the tapered fiber and the double-knot resonator, the wavelengths could be smoothly tuned (Fan et al., 2013). In another study, mode competition in the laser cavity was suppressed using a tapered fiber, whereas an intermodal interference occurred among the microfiber cladding modes, and dual wavelengths were generated with a stable peak power and a signal-to-noise ratio of more than 40 dB (Harun et al., 2010).

2.10 Saturable Absorbers and Their Characteristics

SAs are optical components that are widely used in pulsed lasers. The behavior of any SA when interacting with light is that it absorbs low-intensity light and transmits high-intensity light. In other words, the nonlinear optical properties of a device with an SA are enhanced (He et al., 2013). Recently, graphene has attracted considerable research interest for its various applications in optoelectronic devices, super-capacitors, sensors and nanocomposite materials. This is because of its unique characteristics, such as high surface area, excellent electrical conductivity and high electron mobility. In addition, graphene can be easily obtained through the chemical conversion of inexpensive graphite (Batumalay et al., 2014b). Graphene also shows remarkable optical properties. For example, it can be optically visualized, despite being only a single atom thick. Its transmittance can be expressed in terms of the fine structure constant. The linear dispersion of Dirac electrons makes broadband applications possible. Saturable absorption is observed in graphene as a consequence of Pauli blocking and non-equilibrium carriers resulting in hot luminescence. Chemical and physical treatments can also lead to luminescence. These properties make graphene an ideal photonic and optoelectronic material (Bonaccorso et al., 2010). Graphene can be easily integrated with optical fibers and is used as a polarization controller, as a wideband saturable absorber and in sensing applications (Sun et al., 2016). Meanwhile, GO is a layered material consisting of hydrophilic oxygenated graphene sheets (graphene oxide sheets) bearing oxygen functional groups on their basal planes and edges (Dikin et al., 2007). The nonlinear optical properties of GO have been studied using the Z-scan method, where the GO was prepared using the modified Hummers technique (Liu et al., 2009). The polar oxygen functional groups of GO render it hydrophilic; GO can be exfoliated in many solvents, and it disperses particularly well in water (Zhu et al., 2010).

CHAPTER 3: FABRICATION AND PREPARATION OF OPTICAL MICROFIBERS AND SATURABLE ABSORBER MATERIALS

3.1 Introduction

An essential step before utilizing an OMF in any application is to fabricate a sample with typically preferred properties, such as low propagation loss, low surface roughness and high adiabaticity. This chapter reports the use of a flame-pulling technique to fabricate OMFs using two systems. The first is a modified computer numerically controlled (CNC) machine, and the second is a commercial optical fiber tapering system called the Vytran. In addition, SAs, such as graphene and GO, were also prepared and used to passively produce fiber laser pulses with the assistance of an OMF. These two approaches are discussed in detail in the following sub-sections of this chapter.

3.2 Fabrication of Optical Microfibers Using a Modified CNC Machine

To fabricate OMFs with good accuracy and reproducibility, simultaneous heating and stretching of single-mode optical fibers is required. This method has many advantages compared with other fabrication techniques, such as facile control, good performance and low cost. Consequently, the three most important parameters of the fiber tapering process that determine the fiber quality are the fiber position, flame size and pulling speed (Orucevic et al., 2007).

The OMF fabrication machine used in our laboratory consists of two movable holders on one translation stage for holding and stretching the optical fiber throughout the tapering process. These holders are moved linearly to the left and right by high-precision stepper motors operated by a control board. Moreover, the setup contains an oxygen butane flame torch that is used as the heat source for heating the optical fiber. The

temperature at the optical fiber should not exceed the softening-point temperature of silica fiber. Two cylinders supply the oxygen and butane gases separately. By controlling the oxy-butane gas valves, the flame's size and temperature can be adjusted. The torch produces a jetting flame that could cut or deform the microfiber if the flame temperature were to be higher than the temperature required for OMF fabrication, resulting in a high loss of light transmission. To avoid such a scenario, the flame size should be chosen very precisely, and it is important that the fiber does not reach the center of the flame; therefore, the flame torch stage can be manually shifted from the ignition location to the fiber location and back. During the tapering process, the flame torch must be kept stationary while the optical fiber is elongated. To fabricate an OMF with the desired dimensions, the stepper motors move the fiber holders at different steady speeds in the same direction by rotating a lead screw to apply an appropriate stretch to the fiber. This linear motion procedure is achieved relatively simply using the stepper motors. A Mach 3 CNC computer controller system is used to control the speed of the stepper motors through the controller card. The stepper motors have a step angle of 1.8° (200 steps/revolution). The homemade tapering fiber machine is shown in **Figure 3.1**.

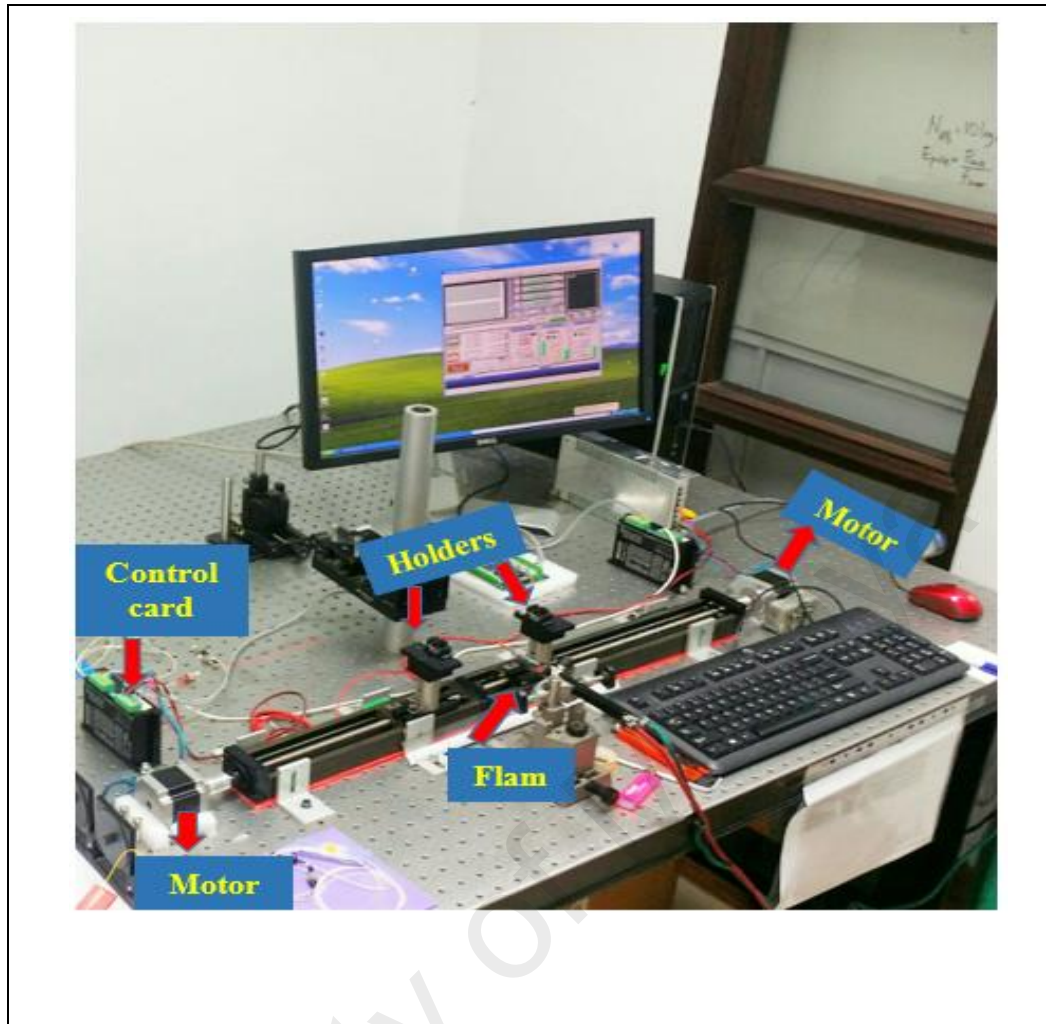


Figure 3.1: Optical microfiber tapering system.

3.3 Fabrication of Optical Microfibers Using the Vytran System

The Vytran optical fiber system (GPX-3400 series) was used to fabricate some of the OMFs discussed in this thesis. The Vytran is a fully computerized system that is capable of performing precise tapering, splicing and fusion of optical fibers. The Vytran system comprises a microheater that consists of graphite in an omega shape that can move along the positioned fiber, fiber holder clamps with three-dimensional axis control, a microscopic system with a high-resolution CCD with the ability to move forward and backward for fiber imaging, and a personal computer. This system works based on the heat-and-pull principle. The microheater can provide a range of temperatures from room temperature to approximately 3000 °C, making it possible to fabricate OMFs of various

shapes and sizes. The movement of the fiber clamps is programmable to assist in positioning, rotating and moving the optical fiber throughout various processes. By using the graphical interface, users can fabricate and taper OMFs with specific desired dimensions. When the Vytran workstation is switched on, the fiber tapering process is started by heating the fiber to the softening point and applying a stretching force. At this time, a tapered-down region is created. When the fiber has been tapered down to a certain diameter, the workstation then maintains the rate of stretching to form a particular length of the fiber into a region with the reduced, but constant, diameter. This region is referred to as the “waist” of the fiber. After the waist region has been created, the pulling force on the fiber is diminished until, finally, a stretching force is no longer applied. This creates what is called the “up taper”. **Figure 3.2** shows the Vytran GPX-3400 workstation.



Figure 3.2: Vytran GPX-3400 workstation.

3.4 Saturable Absorber Properties

SA is a material that is used in a laser cavity to transmit high-energy light while absorbing low-energy light during the propagation of light inside the cavity. Saturable absorbers are widely used in both mode-locked and Q-switched pulsed lasers of the passive type because of their ability to reduce the phase fluctuations of different longitudinal modes to enhance the constructive interference and pulsed radiation produced in a laser cavity. Generally, SAs can be divided into two types: real SAs, optical materials that exhibit strong saturable absorption, and artificial SAs, which are devices that induce an intensity-dependent transmittance through some kind of nonlinear optic effect, such as nonlinear polarization rotation (NPR) and or a nonlinear optical loop mirror (NOLM). Only real SAs are considered in this thesis. In the early 1990s, a SESAM was successfully demonstrated as the first real SA. However, SESAMs have certain limitations, such as narrow-bandwidth operation, high material costs and complicated fabrication. These disadvantages have led scientists to develop many other SAs, such as carbon nanomaterials (CNT, graphene), topological insulators, and transition metal dichalcogenides (TMDs) (Sotor et al., 2015; Woodward & Kelleher, 2015). The interaction of a SA with the light inside a laser cavity to produce a Q-switched or multi-wavelength fiber laser spectrum can either be direct or indirect.

3.4.1 Thin-Film Saturable Absorber

To generate pulsed radiation in a laser resonator, a graphene SA in the form of a thin film was produced using the optical deposition method. An optical fiber ferrule was first spread with index-matching gel (IMG), which is a transparent material with a refractive index of 1.4, similar to that of a silica optical fiber. Afterward, the IMG-covered fiber ferrule was immersed in a graphene solution and then allowed to dry at room temperature. The IMG was used to cause the graphene flakes to adhere and to reduce the Fresnel

reflection at the fiber surface. The sample used in this work had previously been fabricated and used by (Muhammad et al., 2012). When prepared using this method, the saturable absorber will directly interact with light propagating inside the laser cavity. **Figure 3.3** shows a schematic illustration of the fiber facet with the saturable absorber sheet.

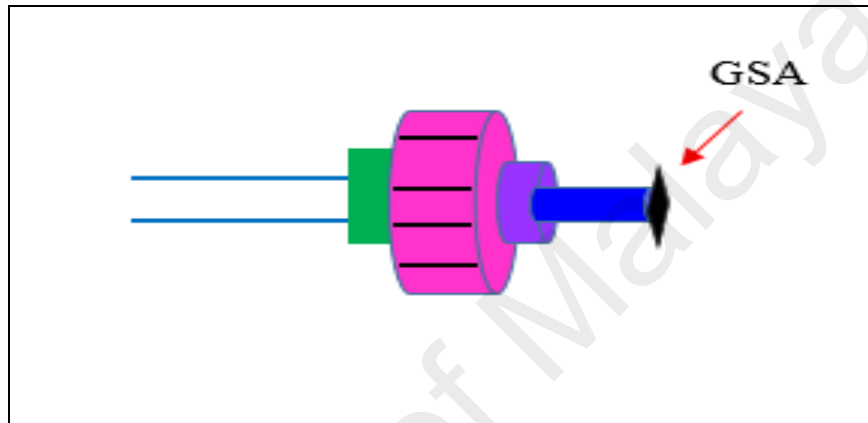


Figure 3.3: Illustration of a graphene thin-film on optical fiber pigtail.

3.4.2 Saturable Absorber Deposited on the Surface of an Optical Microfiber

Another method, called optical deposition, was used to produce a SA element based on interaction with the evanescent field of an OMF. Compared with direct interaction, this method results in a large thermal damage threshold for the saturable absorber and an enhanced nonlinear effect in the OMF/SA platform as a result of the wide area over which the evanescent field interacts with the SA (Khazaeinezhad et al., 2015; Luo et al., 2015a). After the OMF was tapered to the proper dimensions, one end of the OMF was connected to a laser source and the other to an optical power meter to measure the insertion loss of the microfiber before the deposition of the SA. A droplet of commercially available graphene oxide SA solution was deposited onto a glass slide using a microliter pipet, and the fabricated OMF was then immersed in this droplet. An ASE laser source was launched into the SA-deposited microfiber device. The insertion loss of the SA-deposited

microfiber device was approximately 5 dB, and the prepared device was ready to be inserted into a laser cavity to serve as a multi-wavelength, Q-switching or mode-locking generator. Microscopic imaging of the GOSA revealed excellent adherence to the waist of the microfiber. **Figure 3.4** shows an optical microscopic image of the GO deposited on the surface of the OMF.

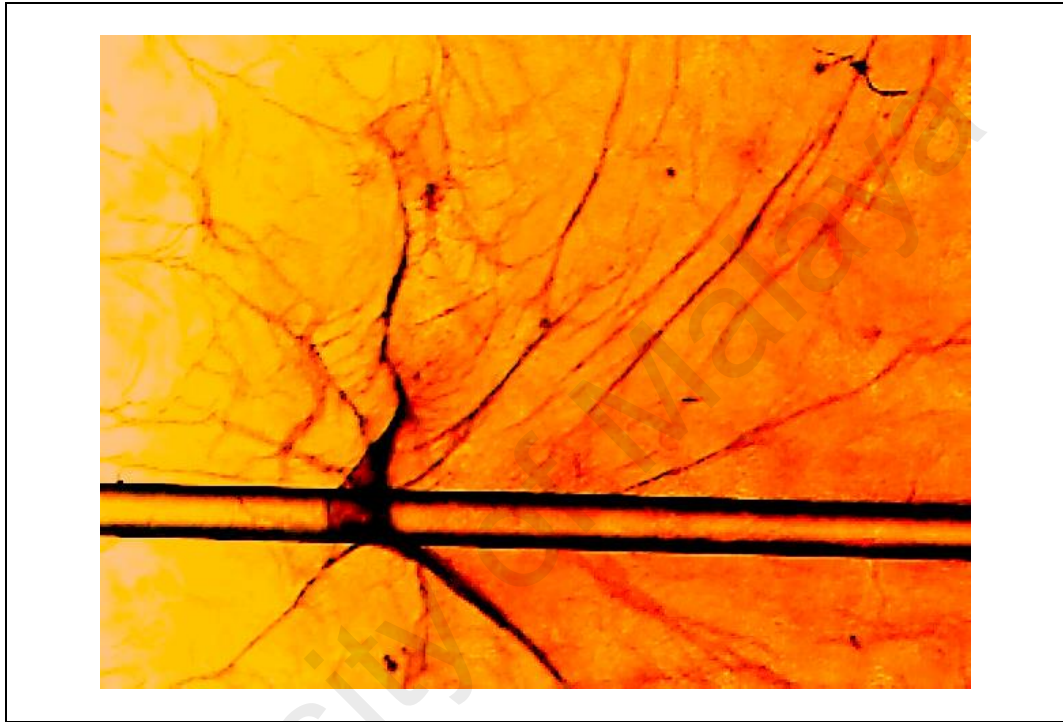


Figure 3.4: Microscopic image of a graphene oxide saturable absorber device.

3.5 Characteristics of Graphene and Graphene Oxide Saturable Absorbers

Two-dimensional (2D) optical materials have been studied extensively and, over the last few years, have been applied in many fields, such as photonics, optoelectronics and sensors, because of their strong optical saturable absorption. Graphene, which is a monolayer of carbon atoms that can be isolated from graphite, has attracted the interest of researchers over the past decade. Graphene exhibits unique properties such as specific integer and fractional quantum Hall effects, a ‘minimum’ conductivity even when the carrier concentration tends toward zero, Shubnikov–de Haas oscillations with a π phase shift due to Berry’s phase, and mobilities (μ) of up to $106 \text{ cm}^2 \text{ V}^{-1} \text{ s}^{-1}$ in suspended samples

(Bonaccorso et al., 2010). By virtue of these optical and electronic properties, graphene and graphene-based materials have been successfully utilized in various applications. Compared with SWCNTs, graphene offers significant advantages, including an ultrafast recovery time, a higher thermal damage threshold, a large saturable absorption modulation depth, a lower saturation intensity and an ultrabroad wavelength spectrum ranging from 300 to 2500 nm. In addition, its thin atomic structure allows it to be easily integrated with other photonic equipment (Luo et al., 2010; Yang et al., 2014). As an alternative to high-quality pure graphene, GO, which is a low-cost precursor for the chemical synthesis of pure graphene, has also attracted attention from a technical perspective as a potential saturable absorption material since it exhibits ultrafast relaxation and strong nonlinear saturable absorption that are nearly comparable to those of pure graphene. GO also has several inherent advantages, such as compatibility with polymers, ease of fabrication and good solubility in water (Lee et al., 2013; Luo et al., 2014).

3.6 Preparation of Chemical Solutions

To prepare an OMF to be used for RI detection, NaCl solutions were prepared as follows. Correct measurements were essential for the preparation of these various NaCl solutions, with weight/volume concentration of 0.5, 0.7, 0.9, 1.1, 1.3, 1.5, and 1.7 %. The measurement technique involved the precise weighing of the salt using a digital weighing balance with an accuracy of 0.001 g. To avoid any error that might be carried forward through serial dilution, each of the above salt concentrations was prepared individually. The corresponding salt weights were calculated as shown below and accurately measured accordingly, and the measured portions were then dissolved in deionized water.

$$\% \frac{W}{V} = \frac{g \text{ of salt}}{100 \text{ ml of solution}} = \frac{g \text{ of salt}}{\text{ml of solution}} \times 100\% \quad (3.1)$$

The water volumes were accurately measured using an analytical graduated cylinder. Once the sodium chloride had dissolved completely (to ensure dissolution, the flask was swirled gently), water was added to bring the volume up to the final value. The same method described above was also used to produce KNO_3 solutions for a different experiment.

University of Malaya

CHAPTER 4: OPTICAL INLINE MICROFIBER MACH-ZEHNDER INTERFEROMETER FOR SENSING APPLICATIONS

4.1 Introduction

Tapered optical fiber has attracted potential interest of researchers over the recent years due to their unique characteristics, such as large evanescent electro-magnetic field, strong light confinement, easy to manipulate and connect to single mode fiber (SMF) (Ma et al., 2014; Wu & Tong, 2013). The tapered OMF applications have been broadened to sensors, filters, optical couplers, supercontinuum generation and atom trapping, that render them preferred as opposed to conventional methods that are used for physical and chemical measurements (Belal et al., 2010; Chen et al., 2008; Jung et al., 2009; Liao et al., 2014). An OMF with small waist diameter has a strong evanescent field and has many sensing applications. Many studies were devoted in determining many types of sensing parameters. As an example, measuring RI is a very important factor in chemistry. Therefore, OMF with different structures are employed to investigate the RI (Shi et al., 2007) . In addition, strain and bending sensor based on multimode interference of OMF has many applications like earthquake and nondestructive evaluation in civil engineering. The tapered OMF for stretch sensing is highly depending on the changing effective refractive index of stretched out microfiber (Li et al., 2014).

Based on the operating principle, optical fiber sensors can be categorized by the primary modulation technique. These modulation techniques have been classified as intensity, phase, frequency, polarization and wavelength modulation. Among all these modulation techniques, intensity based optical sensors is classified as a simple and low cost technique of detecting or measuring different parameters. However, relative measurements and variations in the intensity of the light source may lead to false readings.

On the other hand, phase based optical sensors exhibit a higher sensitivity than intensity based optical sensors and it is classified as the most accurate technique (Fidanboylyu & Efendioglu, 2009; John, 2011; Selvarajan, 2010; Tuma, 1995). The phase change occurring in an optical fiber is detected interferometrically, by comparing the phase of light in a signal fiber to that in a reference fiber. There is a variety of optical fiber interferometers that are commonly used for phase modulation optical fiber sensors such as Mach-Zehnder, Michelson, Sagnac and FPIs. Interest in MZI has increased as a consequence of their simple structure and applicability for many optical and photonic devices. It has long been demonstrated that sensors and modulators incorporating MZIs are based on phase sensitivity to the RI change of the waveguide and/or its surrounding medium (Hsu & Huang, 2005; Wu et al., 2006). Microfiber-based interferometers were given more attention for their main use in RI sensing due to their phase sensitivity to the surrounding medium (Cardenas-Sevilla et al., 2012; Ding et al., 2005; Zhu et al., 2009), while in-line microfiber Mach-Zehnder interferometer (IMMZI) has received considerable attention for advantages such as ease of fabrication, low cost, and small size. The fabrication of IMMZIs are reported via different tapering techniques so that the tapered standard SMF concatenated a dual-tapered region, wherein the fundamental core and cladding modes became coupled; the investigated techniques include the heat-and-pull tapering technique (Jasim et al., 2013a), fusion splicing to arc and heat the fiber (Yang et al., 2011), or operating a CO₂ laser to taper the optical fiber (Wei et al., 2009). This chapter describes the measurements of RI for sodium chloride and potassium nitrate solutions, and strain based IMMZI.

4.2 Fabrication of An Inline Microfiber Mach-Zehnder Interferometer

The schematic diagram for the IMMZI utilized is shown in **Figure 4.1 (a)**, which was fabricated by means of tapering a standard SMF with core and cladding diameters of 8 μm and 125 μm , respectively. This fabrication process involved a glass fiber processing

system (Vytran GPX-3400), in which the uncoated SMF was placed on a motorized fiber-holding block for tapering in accordance to the operator-specified parameters. The Vytran GPX-3400 was equipped with a filament-based heater and fiber holders to simultaneously heat the fiber and pull it in the opposite directions so as to create a tapered structure. To ensure the uniformity and the reproducibility of tapered fibers, the pulling speed and power were set at constant values of 1mm/s and 42W, respectively. An optical microscope image of the IMMZI fabricated by this process is shown in **Figure 4.1 (b)**.

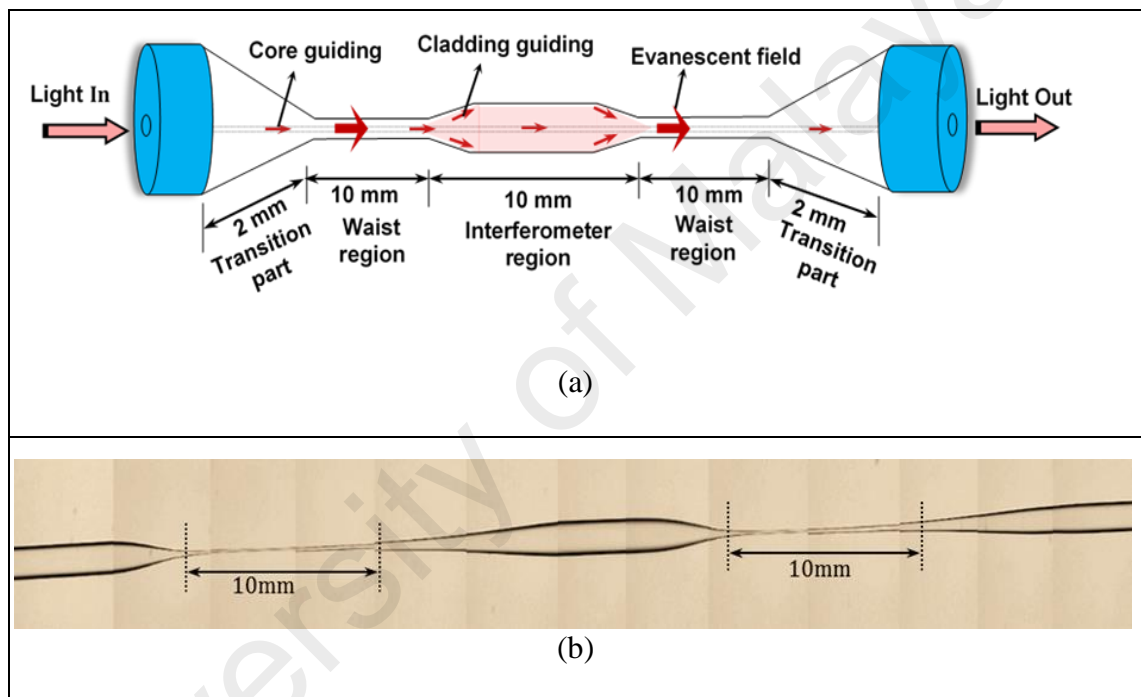






Figure 4.1: IMMZI (a) schematic diagram and (b) optical microscope image.

4.2.1 Characteristic of Inline Microfiber Mach-Zehnder Interferometer

Four samples of IMMZI with different waist diameters were fabricated in this experiment, with each sample consisting of two tapered regions, separated by an untapered section that acts as the interferometer region. These four samples had identical transition part with lengths of about 2 mm, with the waist region length and interferometer region length being around 10 mm. In contrast, the waist diameter of these four samples

was measured to be 10, 11, 12, and 13 μm for samples 1, 2, 3, and 4 respectively, as shown in **Table 4.1**.

Table 4.1: Geometric Parameters of the IMMZI Samples

IMMZI Sample	Waist Diameter (μm)	Total Length (mm)	Microscope Image
Sample 1	10	34	
Sample 2	11	34	
Sample 3	12	34	
Sample 4	13	34	

These samples were prepared to be used as NaCl detectors. The IMMZI sensing mechanism is dependent on wavelength resonance shifts that occur due to changes in the ambient medium RI, which can be triggered by varying the ambient solution concentration. Light launched into an IMMZI device is generally split into guided and unguided modes at the interference region; the guided modes continue to travel in the core, while unguided modes extend through the cladding-air interface and this phenomenon allows the evanescent field to react with the ambient medium. Since IMMZI devices allow splitting and recombining of modes at the interferometer region, an interference signal can be obtained. The intensity transfer function of the IMMZI can be written as:

$$I = I_1 + I_2 + 2\sqrt{I_1 I_2} \cos(\varphi) \quad (4.1)$$

where I is the intensity of interference signal, and I_1 and I_2 are the intensities of the light transfer in fiber core and cladding, respectively. The symbol φ represents the phase difference between the modes of fiber core and cladding, and is given by:

$$\varphi = \left(\frac{2\pi(\Delta n_{eff})L_{eff}}{\lambda} \right) \quad (4.2)$$

where Δn_{eff} can be defined as $[\Delta n_c^{eff} - n_{cl,m}^{eff}]$ and represents the difference between the effective RIs of the core mode and the m -th order cladding mode respectively, L_{eff} is the effective length of the interferometer, and λ is the wavelength of the light. Equation 4.2 shows that the phase difference is directly dependent on the difference in effective RIs as well as the effective length of the interferometer. The fringe spacing between two interference patterns, also known as FSR, can be expressed as:

$$\Delta\lambda = \frac{\lambda^2}{\Delta n_{eff} L_{eff}} \quad (4.3)$$

The output interference spectrum of a fabricated IMMZI with a dual-waist diameter of 10 μ m is shown in **Figure 4.2**, where the spectrum is observed to exhibit well-defined interference fringes with a high extinction ratio of around 20dB and FSR of 8nm. This extinction ratio value provided evidence that the IMMZI could be highly suitable as a sensor device and fiber laser component, since a high extinction ratio can enhance and deliver excellent stability in a multi-wavelength lasing generation system (Ali et al., 2014; Harun & Arof, 2013). In addition, a multichannel filter with a high extinction ratio is effective in slicing the ASE of the gain medium, thus facilitating lasing with narrow

linewidth. For instance, it has been demonstrated in (Ahmad & Dernaika, 2015) that the IMMZI in collaboration with GO flakes can be used as an ultra-narrow filter to create a single longitudinal mode (SLM) laser with a very narrow linewidth and high power efficiency.

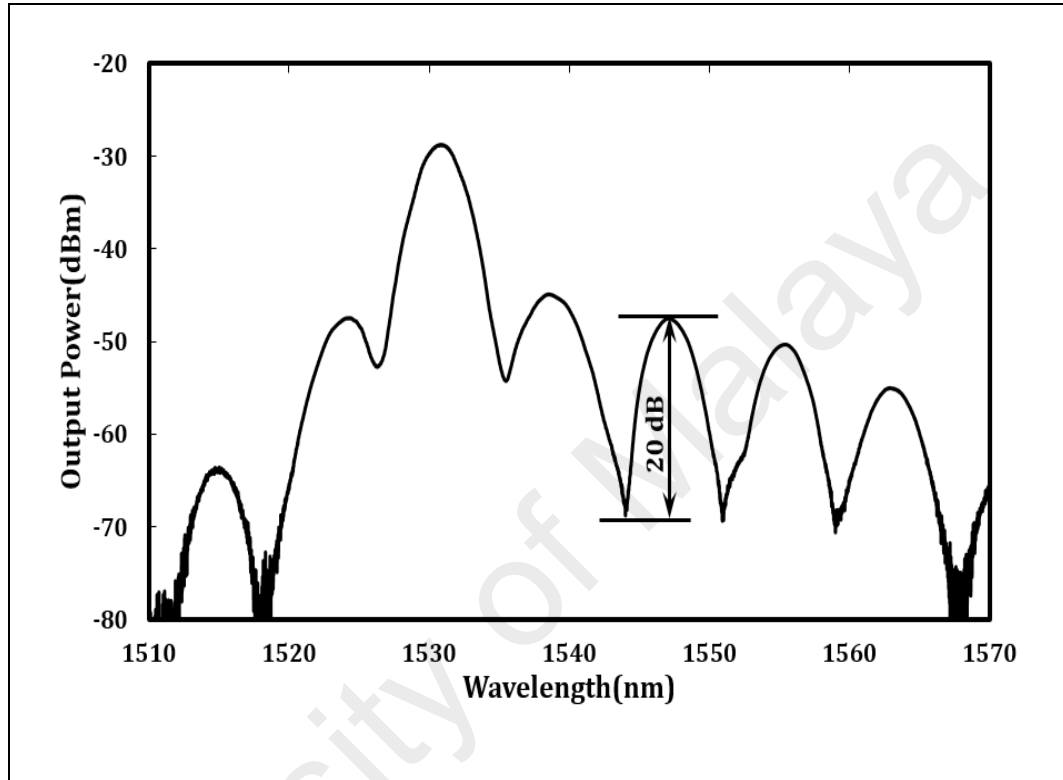


Figure 4.2: Output interference spectrum of an IMMZI with a dual-waist diameter of 10 μm .

4.3 NaCl Detection Using Inline Microfiber Mach-Zehnder Interferometer

Figure 4.3 shows the schematic diagram of the proposed IMMZI-based NaCl detector, in which the IMMZI is placed in a plastic container filled with air and one of the seven aqueous solutions of NaCl is differentiated by mass concentration (0.5 %, 0.7 %, 0.9 %, 1.1 %, 1.3 %, 1.5 %, and 1.7 %) at a constant room temperature and atmospheric pressure. The different concentrations of NaCl indicates that each solution had a specific RI. In order to monitor the optical characteristics and wavelength shifts of the IMMZI inside NaCl solutions, a broadband light source of ASE was injected into the IMMZI input port

while the IMMZI output port was connected to an optical spectrum analyzer (OSA) (model: YOKOGAWA AQ6370B) with 0.05nm resolution. Four IMMZI samples with diverse waist diameters were tested using low concentrations of NaCl to investigate the responsivity of these samples to the RI variation of the NaCl solutions. The RIs of the NaCl solutions depend on the mole ratio of each component, and can be estimated using the following equation (Yu et al., 2014):

$$n_a = [K \cdot n_{NaCl}^2 + (1 - K) n_{Water}^2]^{1/2} \quad (4.4)$$

where n_{Water} represents the RI of water (1.3180), n_{NaCl} is the RI of pure NaCl (1.544), and K is the mole ratio of sodium chloride in the solution. In the studied cases, K is equal to 1.540×10^{-3} , 2.156×10^{-3} , 2.772×10^{-3} , 3.339×10^{-3} , 4.006×10^{-3} , 4.622×10^{-3} , and 5.238×10^{-3} for the NaCl concentrations of 0.5%, 0.7%, 0.9%, 1.1%, 1.3%, 1.5%, and 1.7%, respectively. As such, the RIs of the NaCl solutions with concentrations ranging from 0.5 % to 1.7 % at step change 0.2 %, can be calculated to be equal to 1.31837, 1.31852, 1.31867, 1.31882, 1.31898, 1.31913, and 1.31928, respectively.

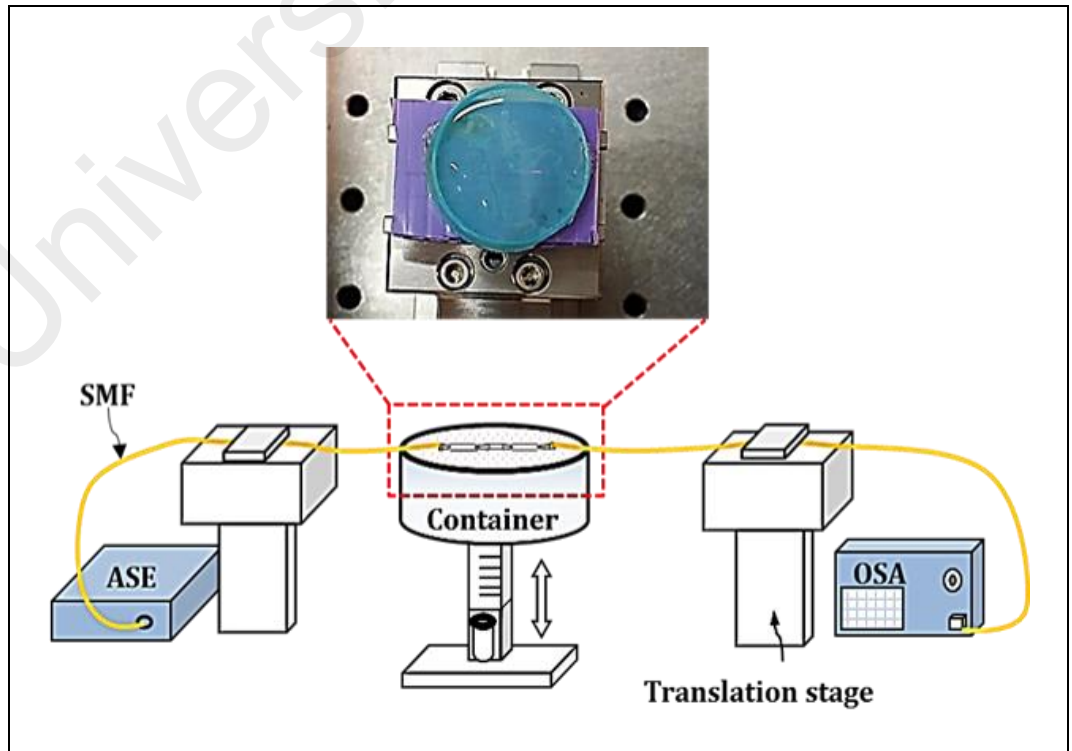


Figure 4.3: Schematic for NaCl detection.

4.4 Results and Discussion

Each IMMZI sample was immersed separately in each of the seven solutions of NaCl. Initially, a syringe was used to remove the solutions from the container after each measurement phase, and then the IMMZI sample was cleaned with deionized water and dried. The samples were also measured in the air for comparison purposes. **Figure 4.4** shows the transmitted interference spectra of the four IMMZI samples with solutions of NaCl in seven different concentrations as well as in the air; in which **(a, b, c, and d)** represents the spectra of samples 1, 2, 3, and 4 respectively. As it can be clearly seen from **Figure 4.4**, the wavelengths of the spectral dip red-shifted when the NaCl solutions' RI increased from 1.31837 to 1.31928 RIU. This shift is attributed to a significant change that occurred in the effective RI difference Δn_{eff} between the core and cladding modes, as well as the higher-order cladding mode that made a significant contribution to the light interference due to its higher RI sensitivity than the fundamental mode (Yang et al., 2011). **Figure 4.5 (a, b, c, d)** shows the wavelengths spectral dip dependence with the index contrast between the solutions; in which **Figure 4.4** shows the transmitted interference spectra of the four IMMZI samples (a, b, c, d) with seven solutions of NaCl. **Figure 4.5 (a, b, c, d)** represents the dependence of samples 1, 2, 3, and 4, respectively. This dependency shows high responsivity of 2913.7, 2811.7, 2012.0, and 1593.3 nm/RI unit (RIU), with a strong linear fit correlation of $r > 0.95$, 0.97, 0.98, and 0.98, respectively. Considering a wavelength resolution of OSA, $\delta\lambda$, the resolution of measurement of the minimum RI variation that can be detected in the OSA that is expressed as $\delta n = \delta\lambda / (d\lambda/dn)$, where $d\lambda/dn$ represents the responsivity of the IMMZI samples. Giving $\delta\lambda = 0.05$ nm, the resolution of measurement for the samples 1, 2, 3, and 4 are calculated to be 1.716×10^{-5} , 1.77×10^{-5} , 2.48×10^{-5} , and 3.13×10^{-5} RIU, respectively. It is observed that the sample 1 has a higher responsivity of 2913.7 nm/ RIU and the lowest resolution of 1.716×10^{-5} RIU than the other samples. This particular case for sample 1

occurred mainly because the sample's waist diameter of $10\mu\text{m}$ was less than that of the other samples, and correspondingly the cladding modes propagation into the ambient medium is increased.

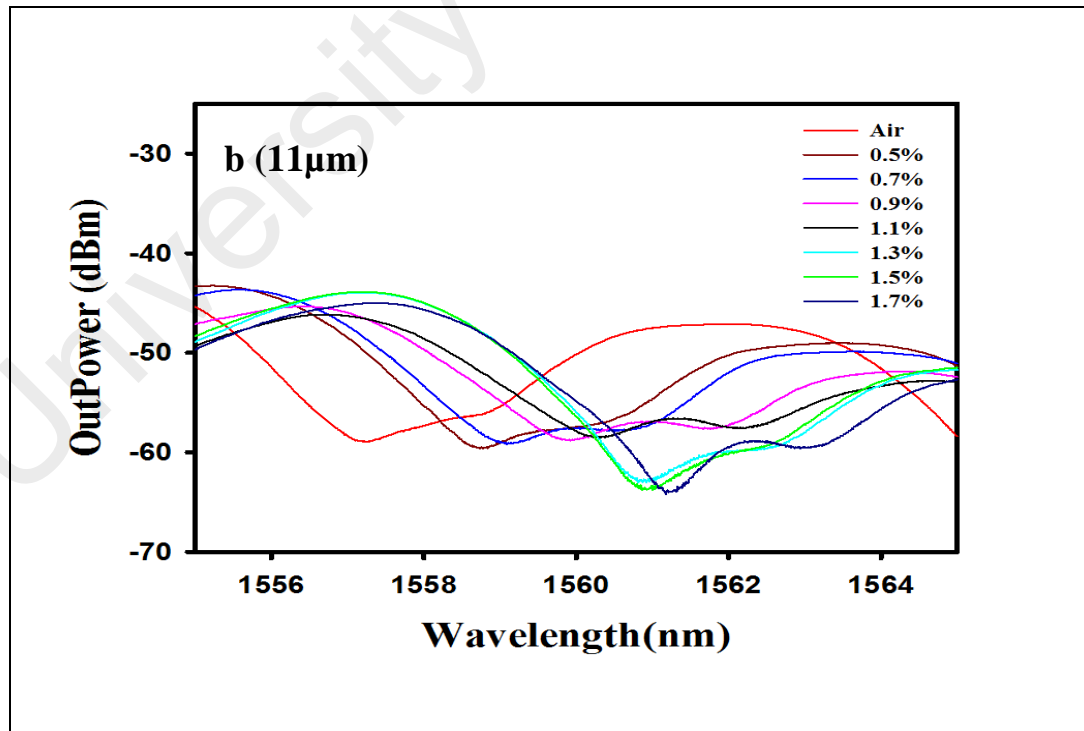
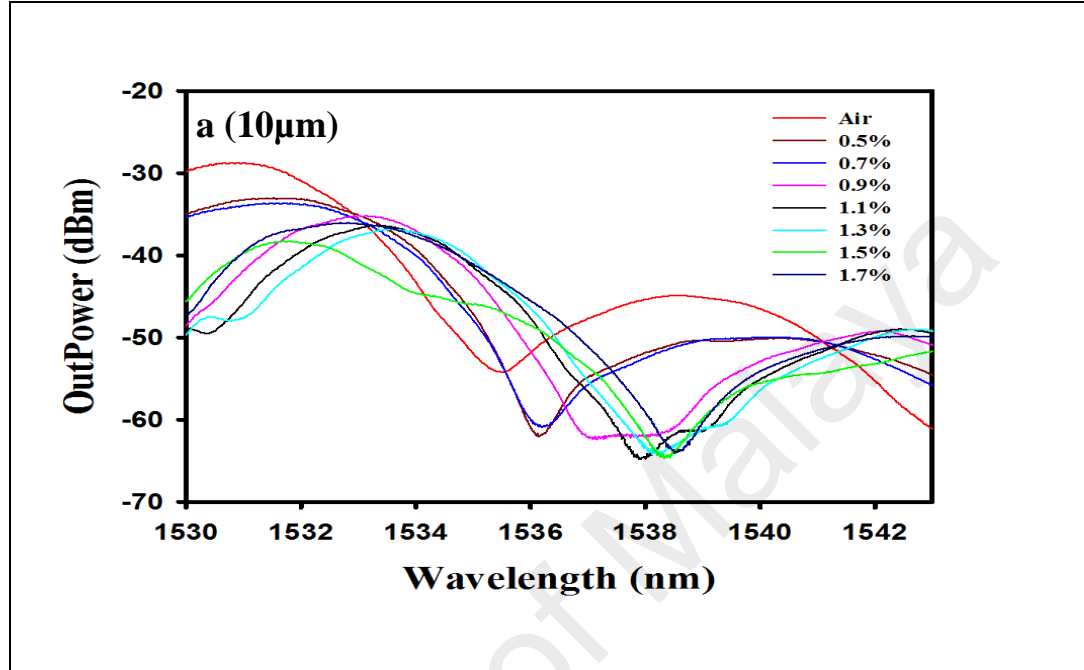


Figure 4.4: Transmitted interference spectra of the four IMMZI samples (a, b, c, d) with seven solutions of NaCl.

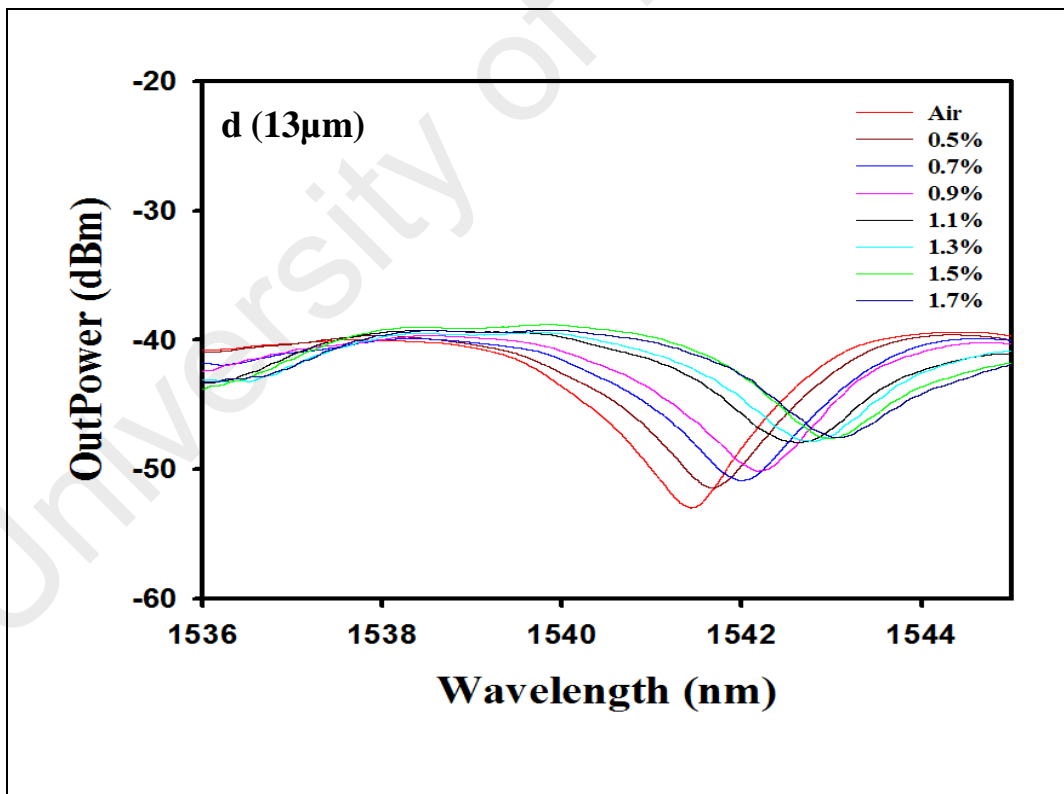
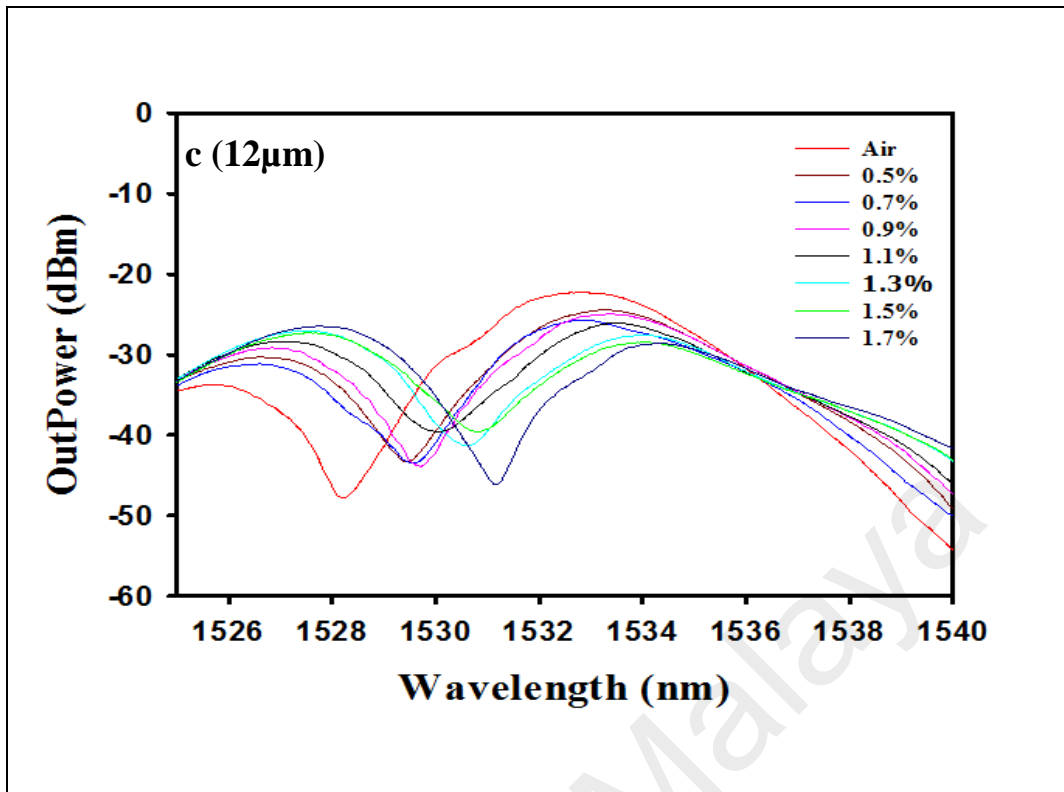


Figure 4.4: Continued.

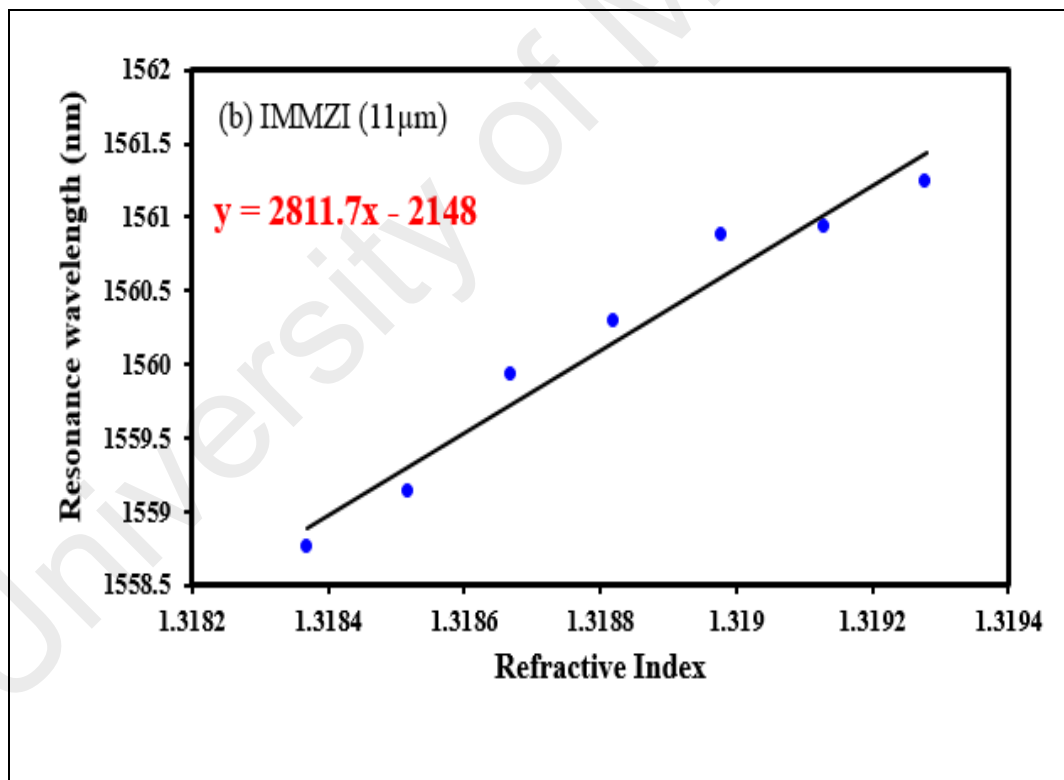
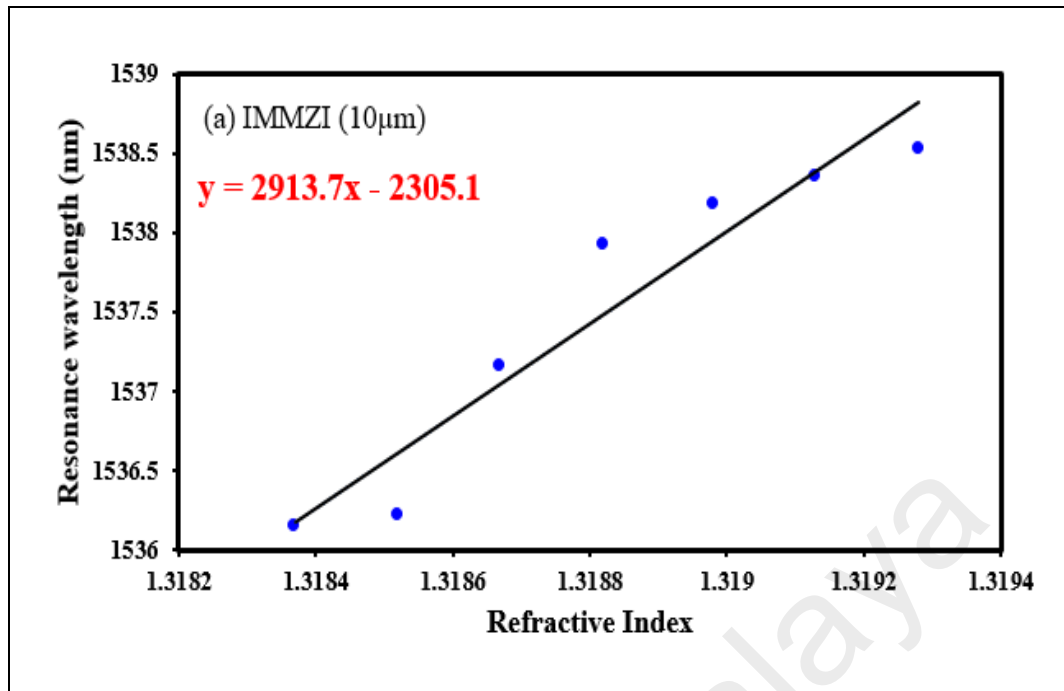


Figure 4.5: Dip wavelengths correlation with different RI ranging from 1.31837 to 1.31928 for the four samples of IMMZI (a, b, c, d).

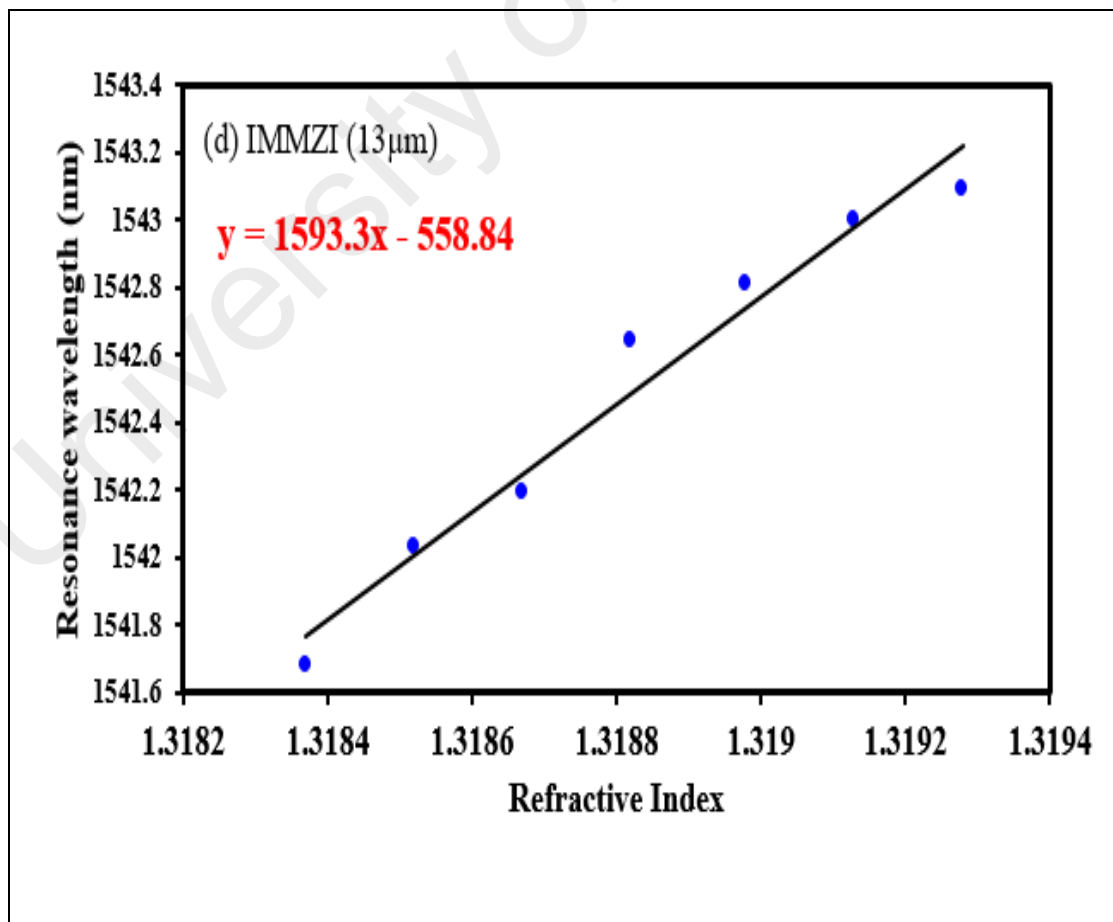
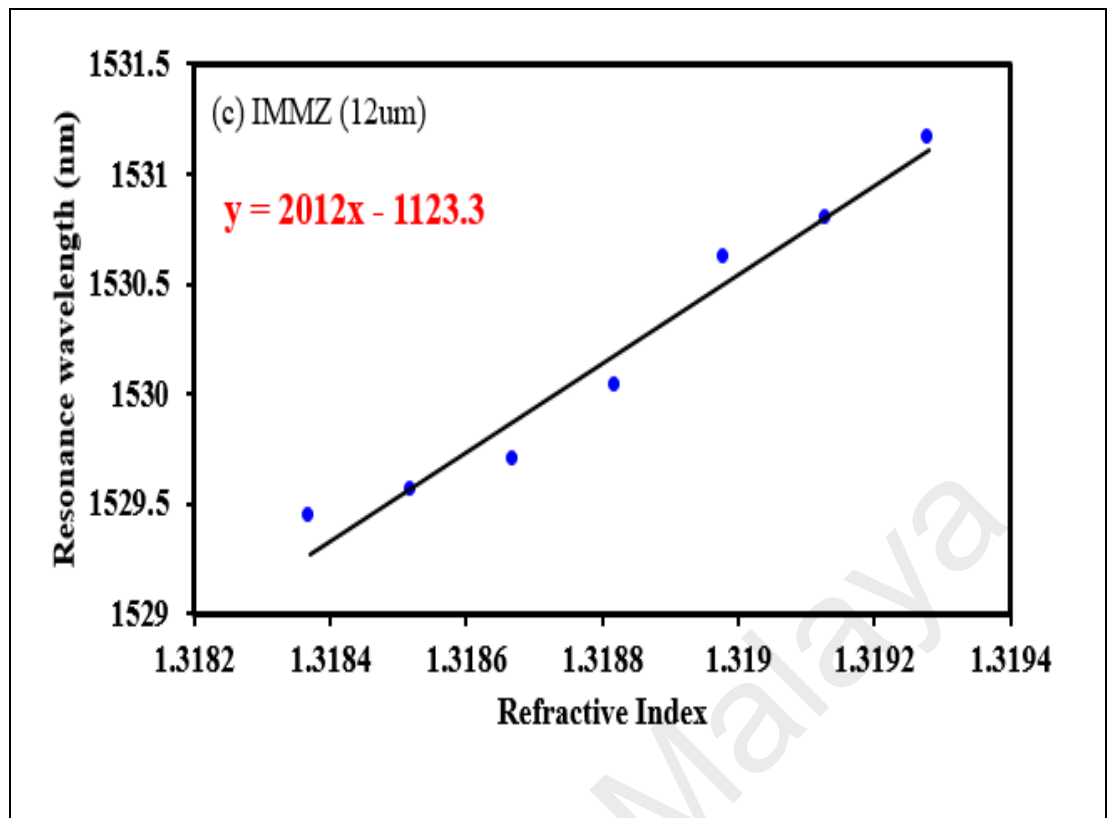


Figure 4.5: continued.

Consequently, the $n_{cl,m}^{eff}$ parameter was significantly affected by the change of the ambient RIs of the NaCl solutions. A reduction in responsivity for an increasing waist diameter was observed for the tapered standard SMF and PCF based RI sensors for RI ranging from 1.333 to 1.435 (Li et al., 2012; Yang et al., 2012), and the responsivity of the proposed IMMZI device was measured much higher on the order of hundreds of nm/RIU. On the other hand, the proposed IMMZI device had a responsivity much lower than that for the twisted highly-birefringent microfiber (HBMF) based RI sensors (Sun et al., 2012), where the HBMF responsivity is on the order of thousands of nm/RIU. This difference was mainly due to the fabricated HBMF having a much lower waist diameter (about $7\mu\text{m}$ in difference) than the fabricated IMMZI sample 1. In practice, this IMMZI was capable of monitoring aqueous solutions with RI ranging from 1.31837 to 1.31928. **Figure 4.6** shows the relationship between responsivity and the waist diameter for the four samples of IMMZI.

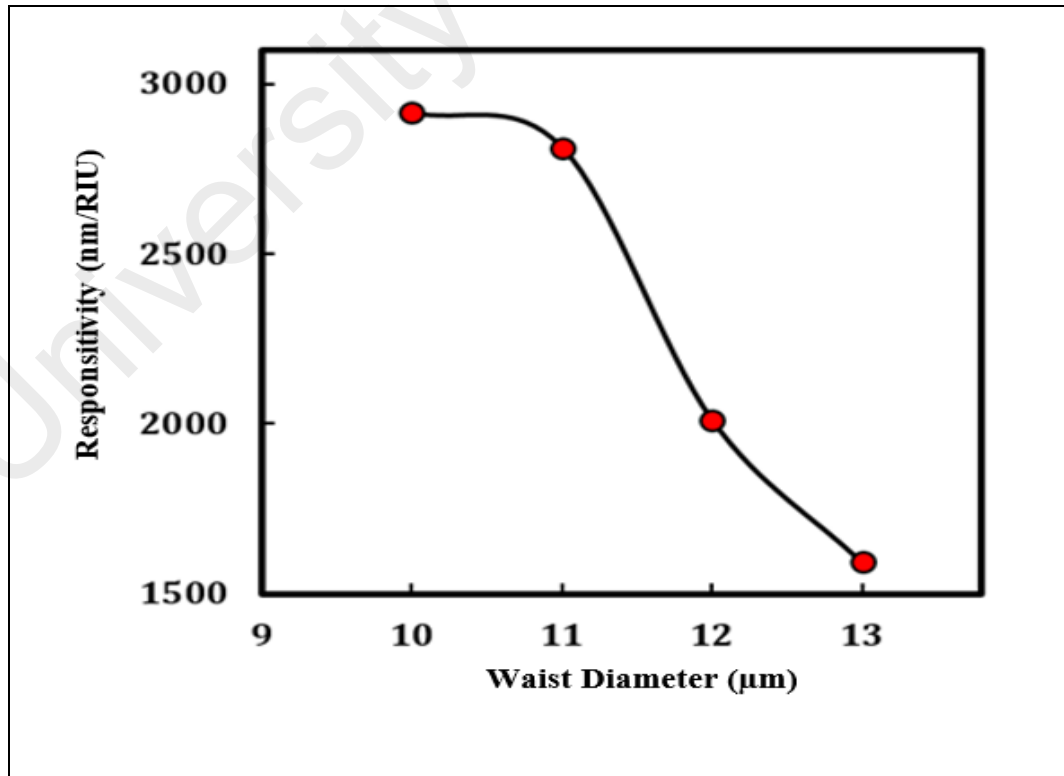


Figure 4.6: Responsivity of IMMZI samples for dissimilar waist diameters.

4.5 Comparison of Optical Microfiber Structures for KNO₃ Refractive Index Detection

4.5.1 Material

Potassium nitrate (KNO₃) is an ionic salt consisting of potassium ions (K⁺) and nitrate ions (NO₃⁻). Potassium nitrate is an important chemical compound in food preservation, especially in the meat and poultry industry, and helps meat to retain its red color. Without preservation measures, red meat and poultry products are strongly susceptible to bacteria, yeasts, and molds, which cause nutritional and sensory deterioration. However, the addition of nitrate components to meat products may result in negative impacts on people's health; one such impact is cancer because nitrate can convert into carcinogenic nitrite if the nitrate concentration exceeds the standard level (Honikel, 2008; Sindelar & Milkowski, 2012). OMFs are widely used as chemical and biological sensors because of their advantageous properties, as mentioned several times in this thesis.

4.5.2 Experimental Setup

In this experiment, the RI values of KNO₃ solutions were measured using an IMMZI and a single tapered fiber (STF), and the sensitivity results for the two structures were compared. Both the IMMZI and the STF were fabricated using the Vytran system. They each had the same length and waist diameter of 35 mm and 12 μm, respectively. **Table 4.2** shows the dimensions of the IMMZI and STF, including the transition length l_t , the waist diameter d_w , and the total length L . To check the sensitivity, various samples of KNO₃ solutions were prepared, with mass concentrations ranging from 2.5 % to 17.5 % in increments of 2.5 %. A single-wavelength EDF laser setup was used, and the tuning of the single wavelength caused by the changing ambient RI was traced and recorded with an optical spectrum analyzer (OSA). Error! Reference source not found. shows the fiber laser cavity used to conduct this experiment. The setup consisted of a laser diode (LD, 980

nm), a 980/1550 WDM instrument, a gain medium (EDF, 3 m), a polarization controller (PC), an OMF sensor, a coupler (90/10), an optical isolator (ISO) and an OSA.

Table 4.2: Parameters of the IMMZI and STF

Parameter	l_t (mm)	d_w (μm)	L (mm)
IMMZI	2	12	35
STF	2	12	35

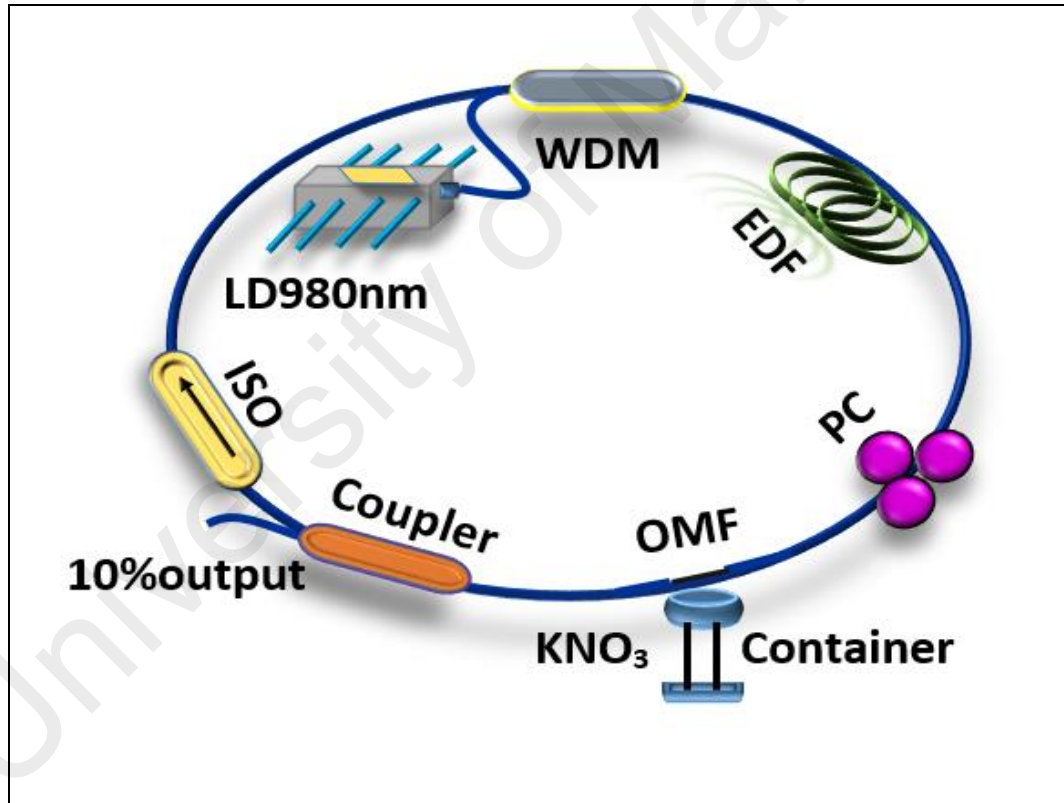


Figure 4.7: Experimental setup for KNO_3 detection.

4.5.3 Results and Discussion

The operational principle of the OMF sensor was based on the shifting of the output resonance wavelength caused by the change in the RI of the surrounding medium. The resolution of the OSA was fixed to 0.05 for all measurements, and a total of 6000 were recorded for each optical spectrum. When the IMMZI was first applied in the EDF laser setup, a single wavelength was generated, centered at 1555.9 nm, with a peak power of -24.72 dBm. **Figure 4.8** shows the output spectrum of the laser cavity with the IMMZI connected. The transmission spectrum shows many interference peaks, which are the result of interference between the excited cladding modes and the core mode.

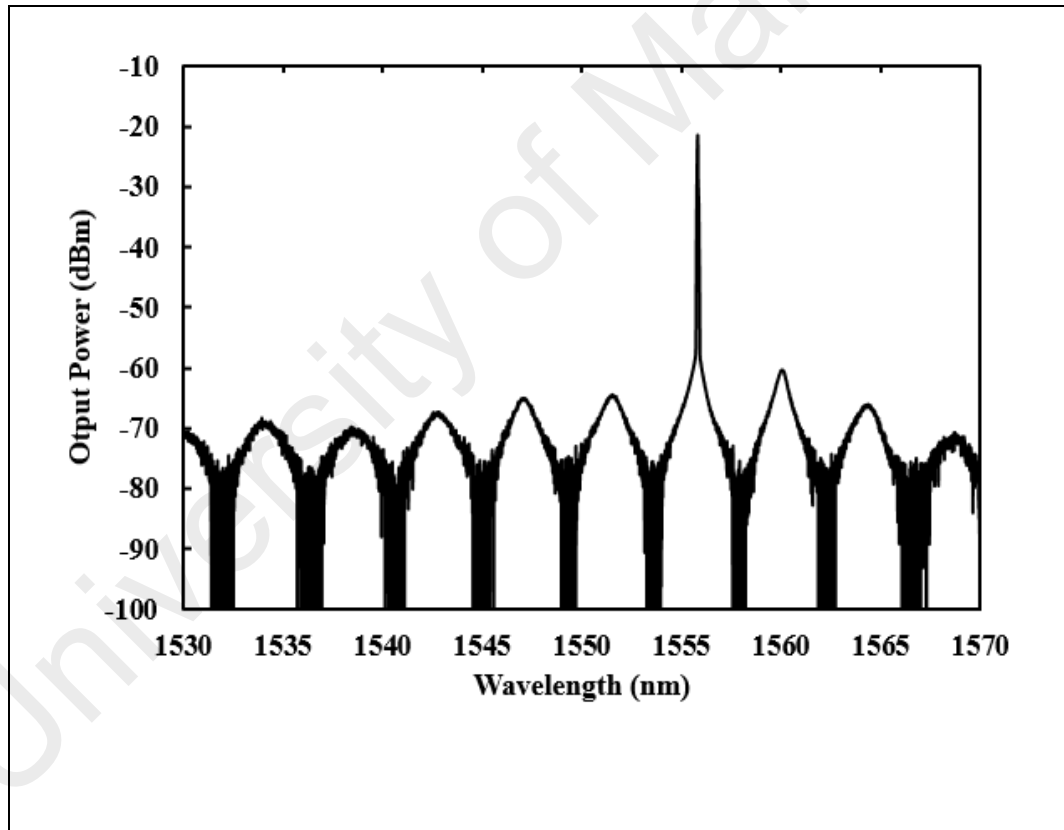


Figure 4.8: Output spectrum of the fiber laser cavity with the IMMZI.

The single wavelength was shifted toward longer wavelengths by changing the RI of the medium surrounding the IMMZI. The IMMZI was cleaned with distilled water and then dried at room temperature after every replacement of the KNO_3 solution to avoid

contamination. **Figure 4.9** shows the shifts in the output spectrum resulting from the changes in the RI for the following surrounding media: air, water and seven samples of KNO_3 with mass concentration values of 2.5 %, 5 %, 7.5 %, 10 %, 12.5 %, 15 %, and 17.5 %. The RIs corresponding to these KNO_3 concentrations were 1.3187, 1.319, 1.32, 1.321, 1.322, 1.323, and 1.324, respectively. The total tuning range was between 1555.97 nm and 1560.78 nm, corresponding to an overall shift of the IMMZI of 4.81 nm.

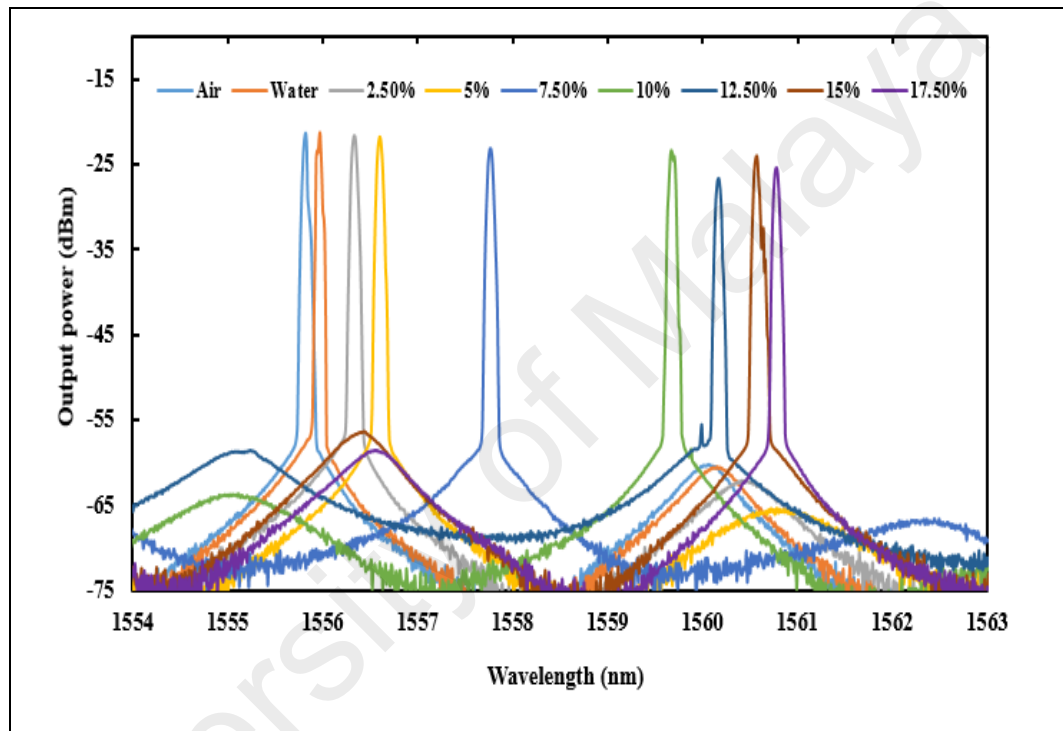


Figure 4.9: Tuning of the transmission spectrum of the IMMZI with different concentrations of KNO_3 .

A second RI sensor experiment was also conducted using a single tapered fiber and the same method previously applied for the IMMZI. A beam with a wavelength centered at 1553.15 nm and a -30.81 dBm peak power was obtained. **Figure 4.10** shows the fiber laser transmission spectrum when the single tapered fiber was used; the number of peaks is smaller than that in the IMMZI spectrum. **Figure 4.11** shows the output spectrum tuning of the single tapered fiber resulting from immersing it in solutions different KNO_3

mass concentrations. The transmission spectrum was tuned from 1553.15 nm to 1555.11 nm wavelength, corresponding to a total shift of 1.96 nm for the STF.

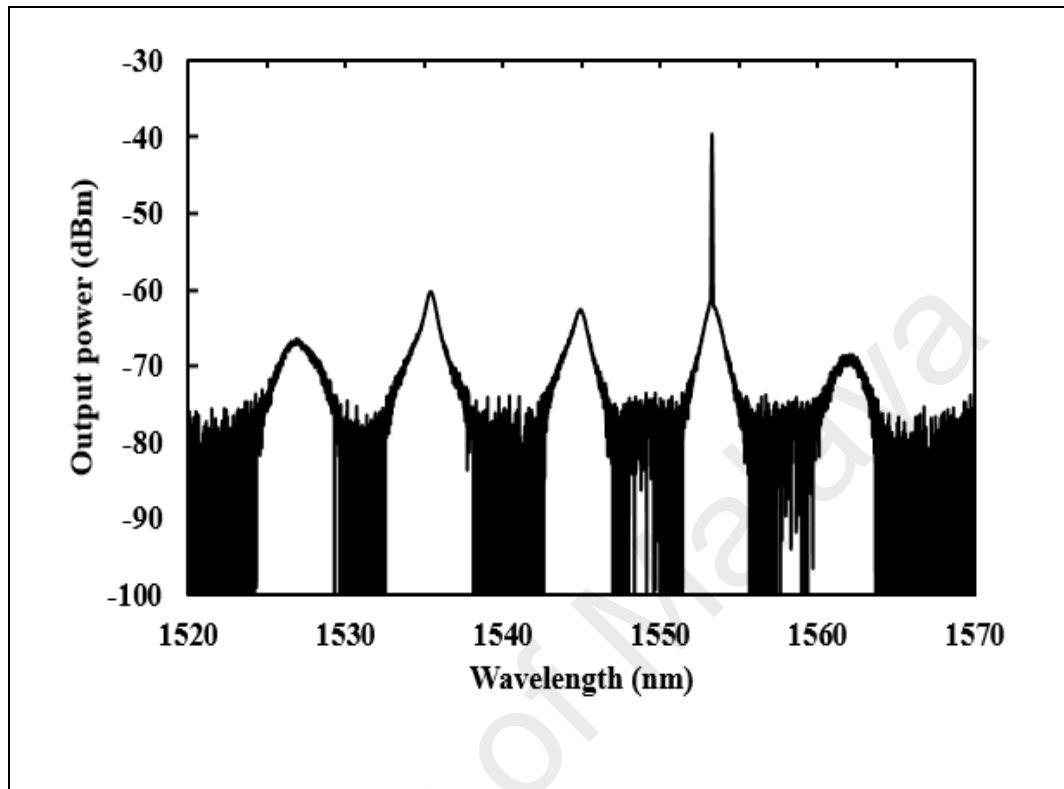


Figure 4.10: Output spectrum of the fiber laser cavity with the STF.

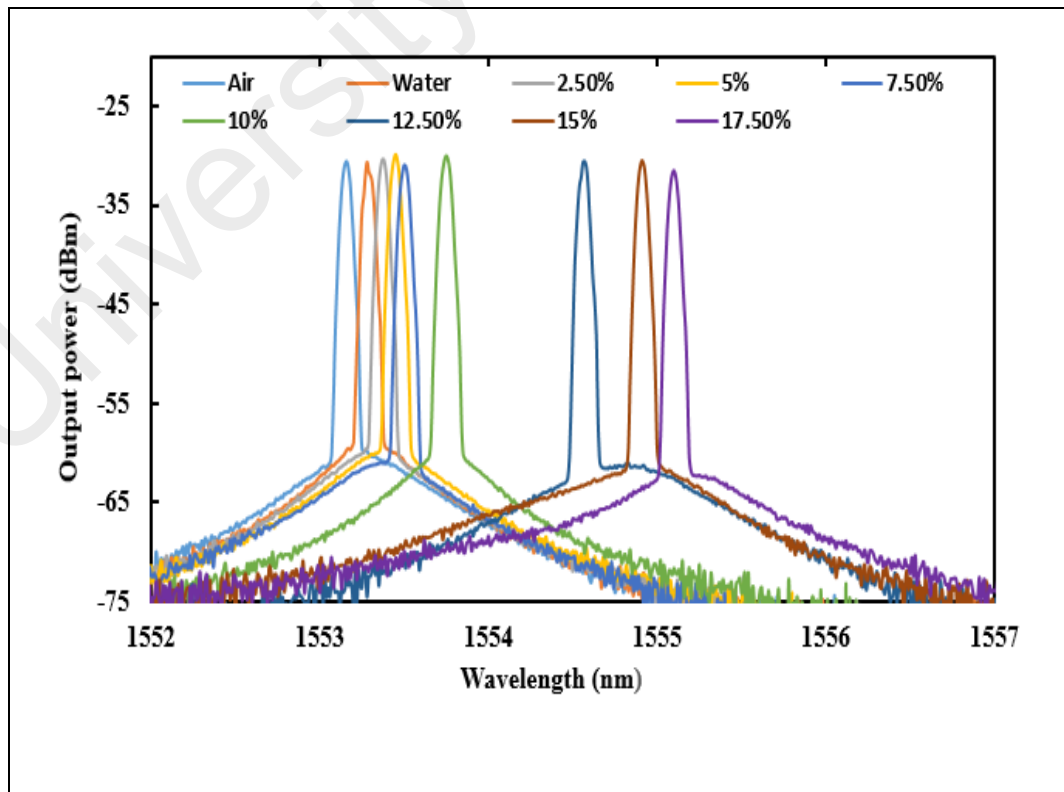


Figure 4.11: Tuning of the transmission spectrum of the STF with different concentrations of KNO_3 .

By plotting the transmission spectra of both the IMMI and the single tapered fiber for the RI range of the KNO_3 solutions, the sensitivities can be calculated. **Figure 4.12** shows the relation between the IMMZI resonant wavelengths and the RIs. The sensitivity is found to be 911.18 nm/RIU, and the slope linearity is high, with a value of 93.68 %. **Figure 4.13** shows the relation between the single tapered fiber resonant wavelengths and the RIs. The sensitivity is 322.41, and the slope linearity is 91.83 %.

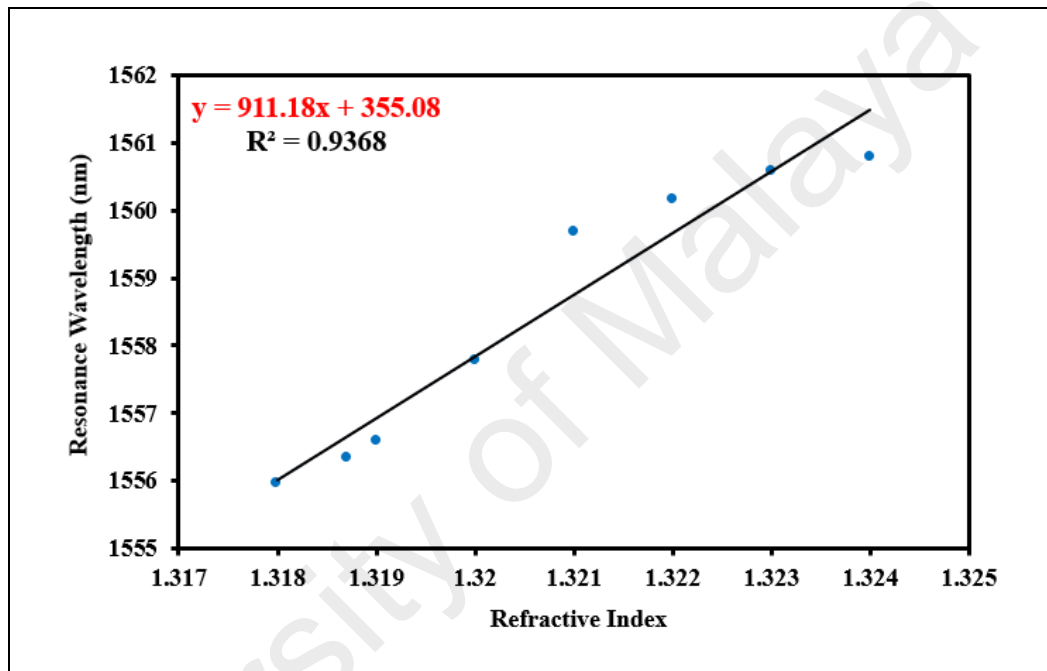


Figure 4.12: IMMZI resonant wavelength as a function of the refractive index.

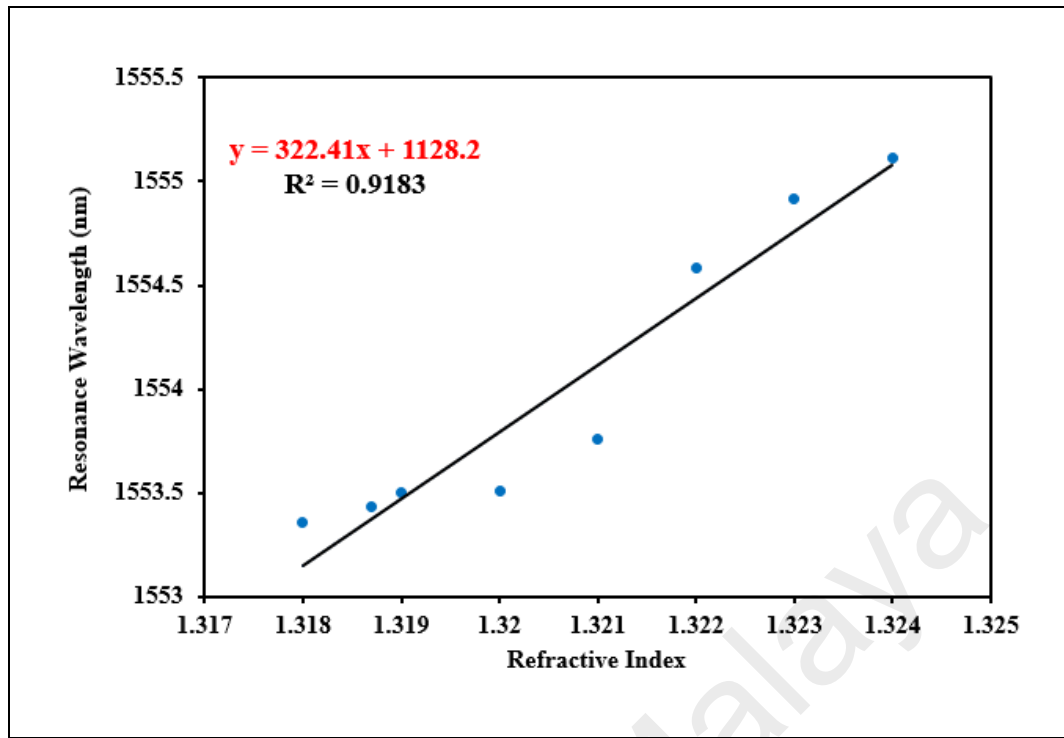


Figure 4.13: STF resonant wavelength as a function of the refractive index.

These results show that the IMMZI has a higher sensitivity of 911.8 nm/RIU compared with the single tapered fiber's sensitivity of 322.41 nm/RIU. In other words, an OMF with double tapered regions shows improved sensitivity compared with a fiber with a single tapered region. In addition, the linearity of the IMMZI is better than that of the STF.

4.6 An Inline Microfiber Mach-Zehnder Interferometer for Strain Sensing

Fiber-optic sensors have received considerable research attention and have been extensively used to detect RIs (Jasim et al., 2014), temperatures (Muhammad et al., 2013), magnetic fields (Sun et al., 2010), gases (Minkovich et al., 2006), currents (Ahmad et al., 2013), strains (Li et al., 2014), and other parameters because of their advantageous properties of small size, electromagnetic immunity, low attenuation, high response to the surrounding environment, and low cost. Many kinds of optical fiber techniques have been used to develop strain sensors, such as FBGs (Yang et al., 2007), FPI (Deng et al., 2011), a displacement sensor in which multimode interference is exploited by splicing a section

of multimode fiber to a single-mode fiber (Mehta et al., 2003), and an IMMZI with an inner air cavity along the fiber length or a photonic crystal fiber (Bai et al., 2014; Liao et al., 2013). The operating principle of a MZI depends on the interference induced by the phase difference between the core and cladding modes. This interference is caused by the difference in the effective refractive index (RI_{eff}) resulting from a change in the surrounding medium or the geometric dimensions of the MZI (Selvas-Aguilar et al., 2014; Zheng et al., 2013). Various tunable filters have been proposed and demonstrated for achieving tunable fiber lasers, such as FBG (Babin et al., 2007), three band-pass filters (Chen et al., 2003), a Fabry-Pérot filter (Masson et al., 2010), a filter based on the multimode interference effect (Castillo-Guzman et al., 2010), and a tunable birefringence comb filter using a semiconductor optical amplifier with a Sagnac loop interferometer (Lee et al., 2004). Although there have been reports from the same group concerning fiber lasers covering the optical network bands (Ahmad et al., 2005; Harun et al., 2006; Mahdi et al., 2000), there is a need to explore the possibility of tunable single-wavelength fiber lasers. In this experiment, a strain sensor based on an IMMZI was investigated based on the tuning of a single-wavelength EDF laser under the application of a stretching force to the IMMZI.

4.6.1 Experimental Setup

A schematic diagram of the strain measurement setup is shown in **Figure 4.14**. It consisted of a laser pump (LD, 980 nm), a WDM, a 3 m long EDF as a gain medium, an IMMZI sandwiched between two adjustable stages with a 13 cm separation distance, a 90/10 coupler, a PC, and an ISO. The output of the laser was measured simultaneously using an OSA (Yokogawa AQ6370B) through the 10-percent port of the coupler.

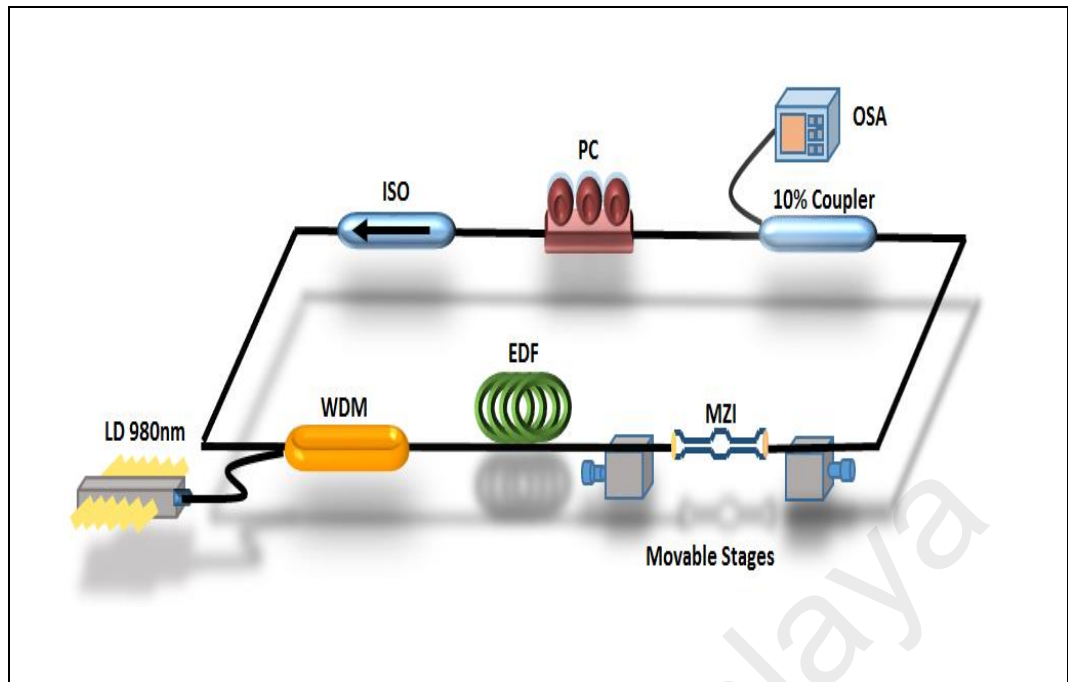


Figure 4.14: Experimental setup for IMMZI strain measurements based on a tunable single-wavelength EDF laser.

To fabricate the IMMZI, we used a standard single-mode fiber (SMF) with core and cladding diameters of $8\ \mu\text{m}$ and $125\ \mu\text{m}$, respectively. Once stripped and cleaned, the fiber was placed onto the motorized fiber-holding blocks of the Vytran GPX-3400 fiber glass processing system for tapering in accordance with the specified parameter settings. The transition length, length and diameter of the tapered fiber's waist were precisely controlled during this process to ensure adiabaticity and uniformity. The Vytran GPX-3400 tapering system uses a filament-based heater to soften the fiber while the fiber holders pull the fiber to create the desired taper dimensions. The pulling speed and power were set to constant values of $1\ \text{mm/s}$ and $42\ \text{W}$, respectively, to ensure the uniformity and reproducibility of the fabricated tapered fiber. The heating element of the Vytran is fixed. To fabricate two tapered regions, the first region was tapered until the desired waist diameter was achieved. Then, the fiber holders were shifted by approximately $1\ \text{cm}$ from the first tapered region to begin tapering the second region. An optical microscopic image of the IMMZI sensor is shown in **Figure 4.15**, where the transition distance (L_T) for both sides is $2\ \text{mm}$, the waist length (W_l) is $10\ \text{mm}$, and the waist diameter (W_D) is $10\ \mu\text{m}$. The two tapered regions are separated by a distance of $10\ \text{mm}$.

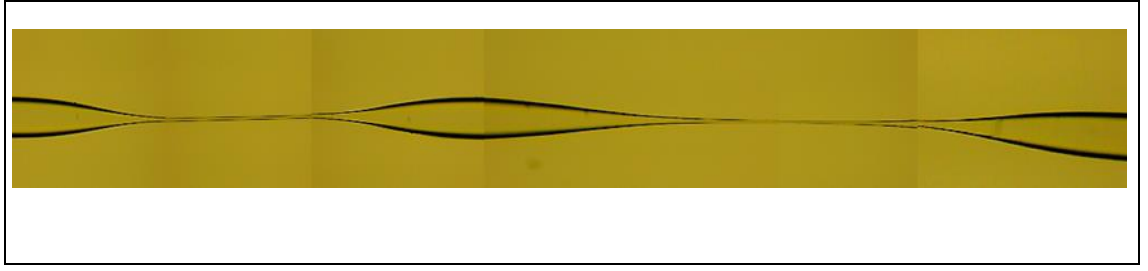


Figure 4.15: Microscopic image of the IMMZI.

4.6.2 Results and Discussion

Figure 4.16 shows the output spectra of the laser at different strain values. With a change in the axial strain ϵ , the length of the IMMZI changes by ΔL , where $\Delta L \ll L$. The strain was increased from 20 μm to 80 μm using a translation stage with a step size of 10 μm . At the strain value corresponding to 10 μm , no change in the laser output spectrum was observed. This was because the IMMZI had not yet reached a straight line. With the application of further strain, the wavelength peak of the tunable fiber laser shifted to a shorter wavelength, satisfying the following equation:

$$\Delta\lambda_m = \lambda_m - \lambda_{m-1} \approx \frac{\lambda^2}{\Delta n_{eff} L} \quad (4.5)$$

where $\Delta\lambda_m$ is the separation between the wavelengths of maximum attenuation, Δn_{eff} is the difference in RI between the core and cladding modes, L is the interference length of the IMMZI sensor, and λ is the operating wavelength. This shift was due to the increase in the RI_{eff} of the fiber core as well as the expansion in the length of the interference section of the MZ interferometer. In addition, this single peak continued to shift to the left at a rate of approximately 1 nm per 10 μm of strain as the applied strain was increased from 20 μm to 80 μm . As shown in **Figure 4.16**, the results clearly indicate a total laser tuning range of 6.19 nm, spanning the wavelength range from 1552.94 nm to 1559.13 nm.

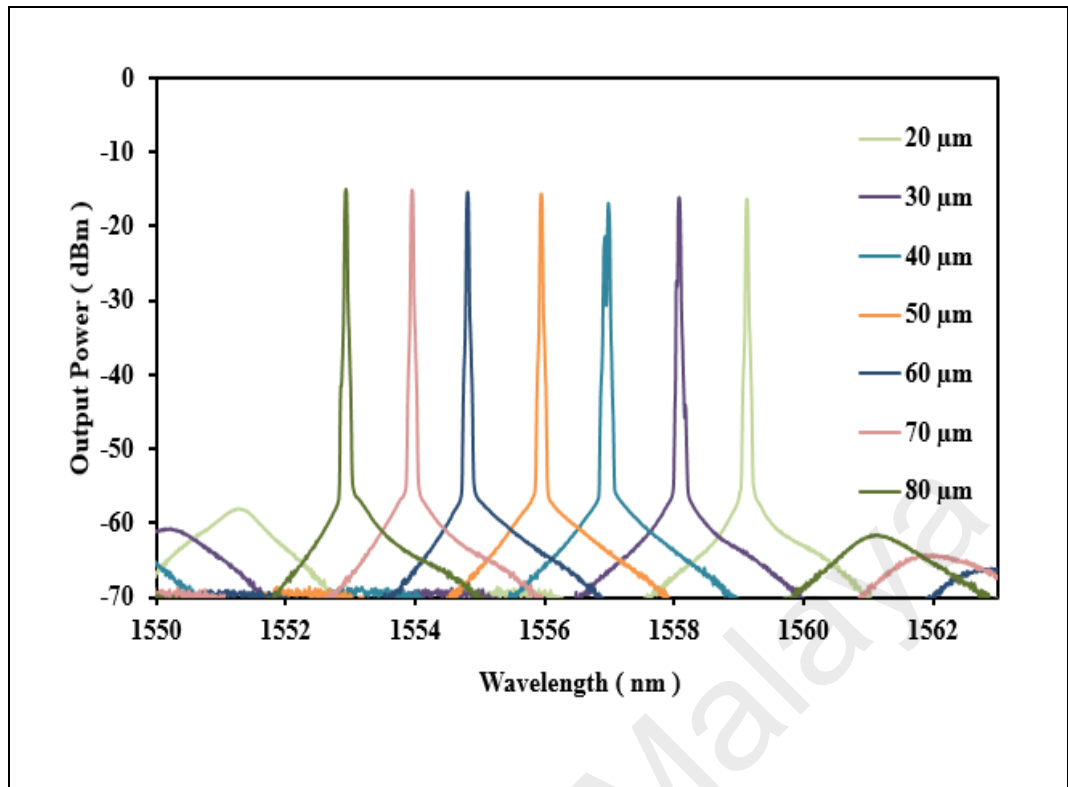


Figure 4.16: Output power of the IMMZI at increasing strain values.

Similar results were obtained when the strain value was decreased from 80 μm to 20 μm . In this case, the peaks shifted to longer wavelengths as the strain was reduced from 80 μm to 20 μm , as presented in **Figure 4.17**. In addition, only small wavelength differences were observed in the shifting of the peaks between the increasing and decreasing processes, with a maximum value of only 0.31 nm. This demonstrates that the measurements performed using the proposed IMMZI are reversible and repeatable.

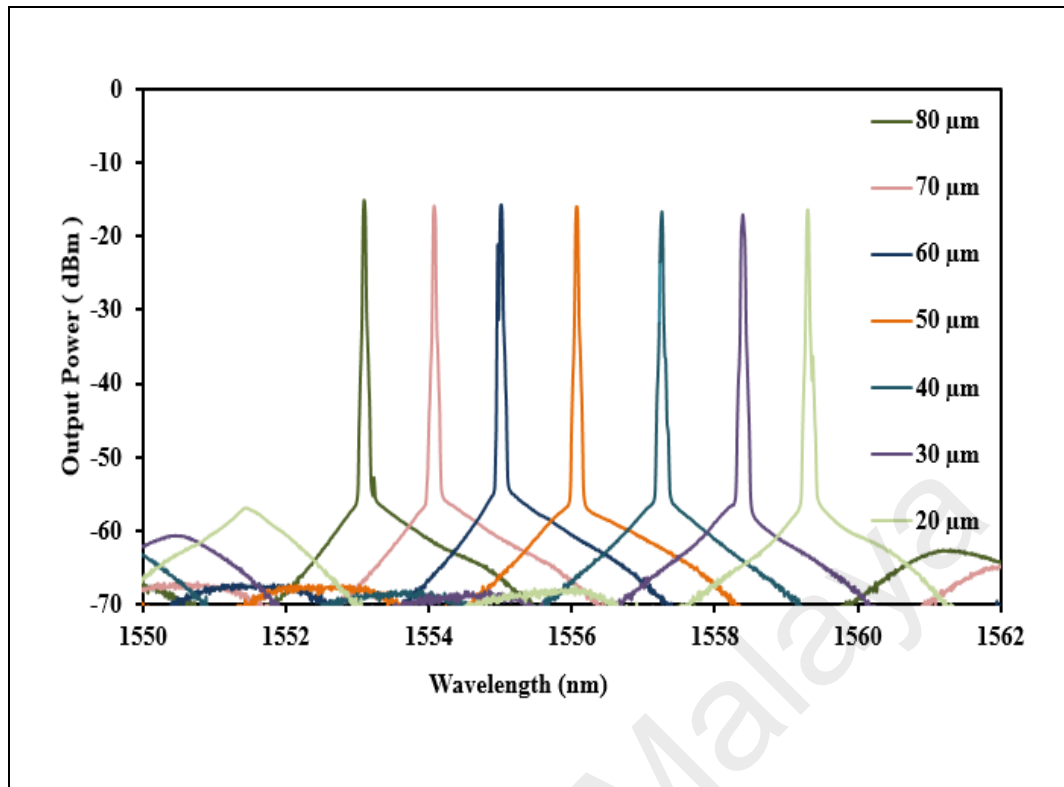


Figure 4.17: Output power of the IMMZI at decreasing strain values.

To confirm the above results, another method of varying the strain on the IMMZI sensor was applied; this method is called discrete adjustment. In this experiment, a measurement was made upon changing the strain from 20 μm to 30 μm . Then, the strain was lowered again to the reference value of 20 μm , and the result of this change was recorded. Next, the strain was increased again, this time to 40 μm , before the strain was lowered back to 20 μm , and measurements were made for both processes. This type of strain adjustment was repeated for every incremental step of 10 μm until a strain value of 80 μm was reached, and all corresponding measurement results were recorded. **Figure 4.18** presents the measurement results, which exhibit similar behavior to that observed using the first method. This further demonstrates that the results of the experimental setup are reproducible. To observe the consistency of the results over a longer duration, the results for the IMMZI under 40 μm strain were recorded once per minute for 16 minutes. **Figure 4.19** presents the measured results at the wavelength peak of approximately

1557.182 nm. It is observed that the results measured by the proposed interferometer remained not only stable but also consistent during the 16 minutes of measurement.

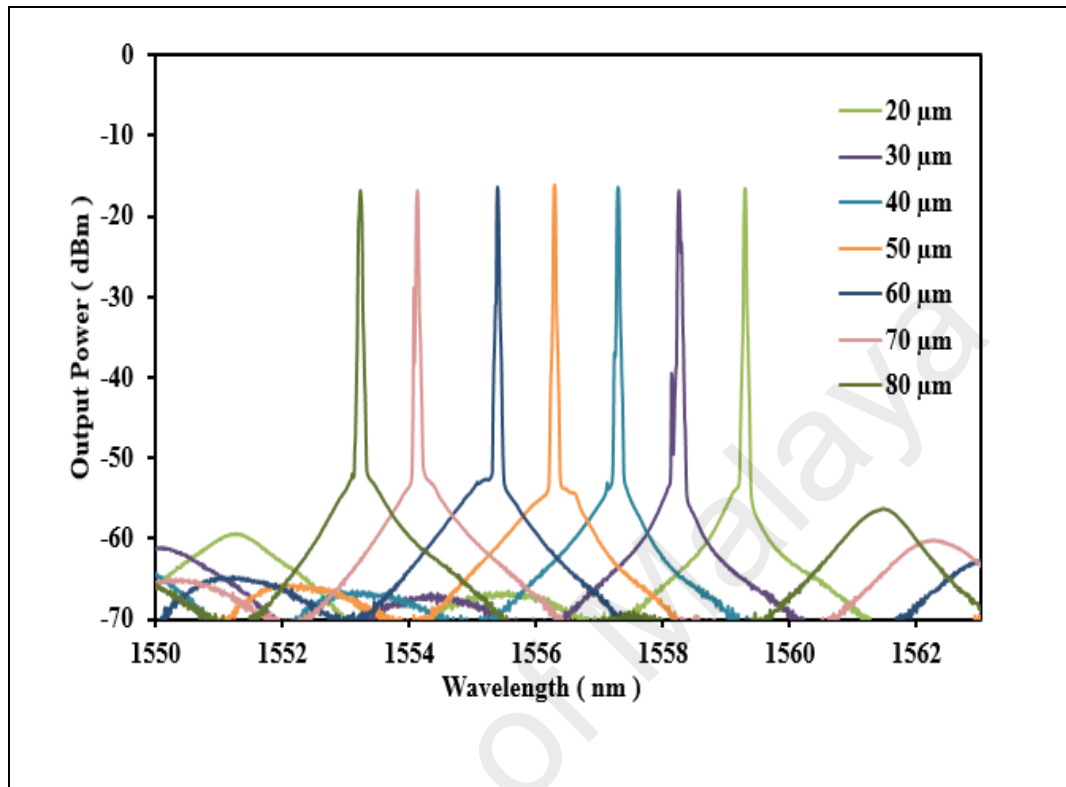


Figure 4.18: Output power of the IMMZI measured using the second strain adjustment method.

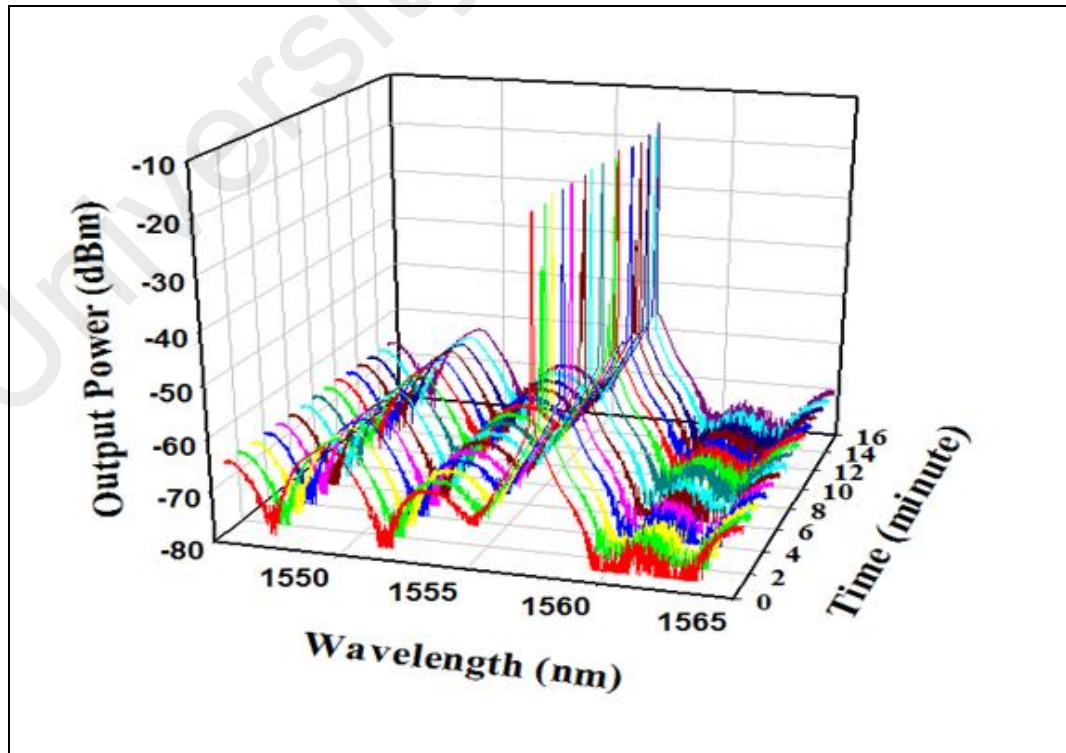


Figure 4.19: Stability over time of the wavelength peak at 1557.182 nm.

The relationship between the wavelength shifts and the different applied strain values is depicted in **Figure 4.20**. In this case, it is found that the graph exhibits a linear slope, as indicated by the coefficient of determination R^2 , which is nearly equal to 1. This indicates that the tunable wavelength is linearly proportional to the strain value. This is an important result because this linear behavior allows a specific strain value to be calculated beforehand and applied to obtain a desired wavelength shift. The result of fitting the wavelength shift with a linear curve shows that the peak wavelength shifts to shorter wavelengths with a sensitivity of 103.5 pm/ μm . The results of the proposed measurement system show significant improvement over those of an earlier report (Mehta et al., 2003) because of the smaller diameter of the fiber used in this experiment. The high R^2 value of 0.9992 also indicates that the proposed ring cavity laser setup based on an IMMZI strain sensor exhibits high accuracy and yields a signal that is strongly dependent on the strain value.

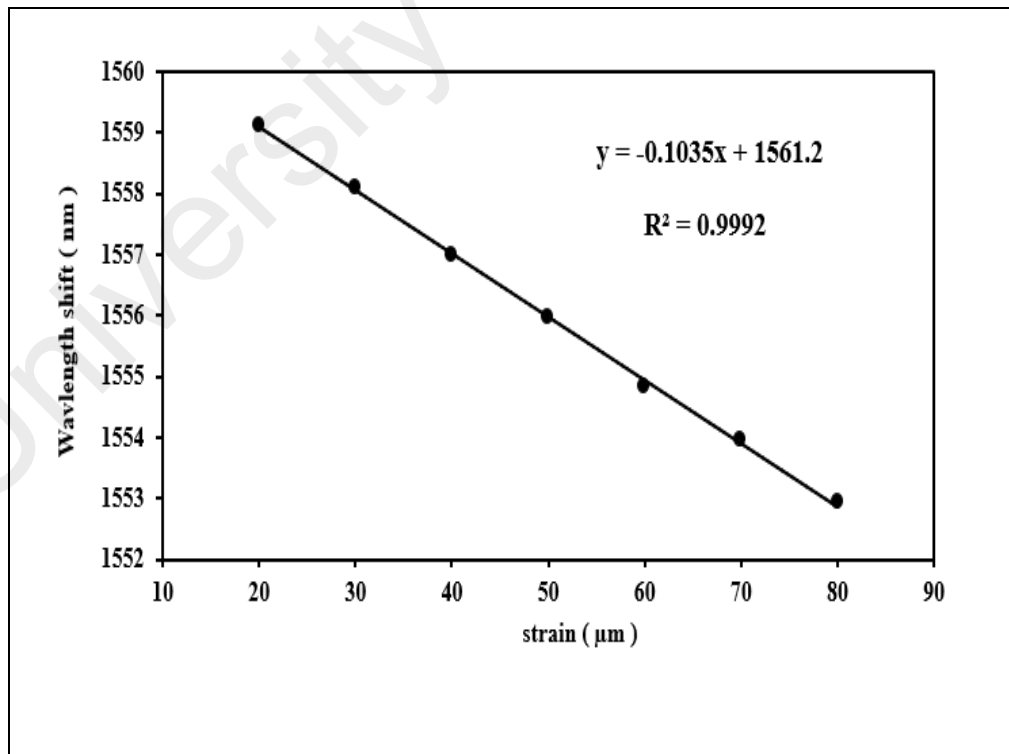


Figure 4.20: Wavelength shifts versus strain values from 20 to 80 μm .

Our proposed system has many advantages, including technical simplicity, low cost, repeatability, ease of fabrication and a wide tuning range compared with other techniques, which are complex and expensive. This tunable fiber laser based on an IMMZI strain sensor can be useful for optical communications applications, mainly in DWDM and CWDM, as well as for medical treatments (Castillo-Guzman et al., 2010; Yun-Shan et al., 2015).

University of Malaya

CHAPTER 5: MULTI-WAVELENGTH AND PULSED LASERS BASED ON TAPERED OPTICAL FIBERS AND GRAPHENE SATURABLE ABSORBERS

5.1 Introduction

Multi-wavelength fiber lasers and pulsed lasers have attracted the attention of researchers for many decades because of their wide array of potential applications in fiber laser sensing, optical communications, measurement systems and laser processing (Lou et al., 2004; Maran et al., 2004; Perez-Herrera et al., 2012). A stable multi-wavelength EDF laser operating at room temperature can be designed based on different techniques, such as a nonlinear optical loop mirror, which contributes to suppressing the mode competition effect of the homogenous broadening of an erbium-doped fiber (Zhang et al., 2008), enhancing the four-wave-mixing effect based on a 5 km single-mode fiber (Wang et al., 2013). Recently, based on a Sagnac loop structure includes a 48.6:51.4 coupler, PC and a piece of 2 km single-mode fiber, a stable multi-wavelength fiber laser has been obtained (Wang et al., 2016). Meanwhile, pulsed lasers can be essentially classified into Q-switched and mode-locked types. The techniques that are used to generate pulsed lasing may be either active or passive (Haus, 2000). The strong evanescent wave of a tapered optical fiber is one of the interesting properties that have found many applications in fiber lasers, including passive Q-switched and mode-locked pulsed lasers. Because of the small waist diameter of a tapered fiber, its electromagnetic field can propagate outside the boundary of the core-cladding interface and interact with the surrounding medium. The surrounding medium can be a light-sensitive material such as graphene, GO, molybdenum disulfide, or a topological insulator. These materials are called (SAs) and are widely used to generate Q-switched and mode-locked pulsed lasing (Chen et al., 2014; Luo et al., 2012; Xu et al., 2012). An SA is applied in a laser cavity either by inserting

the SA between two fiber-optic ferrules as a thin film or using optical energy to deposit the SA on the end face of the fiber or by optically depositing the SA around the tapered OMF (Kashiwagi & Yamashita, 2009; Luo et al., 2010; Luo et al., 2012a). The small waist diameter of the microfiber also endows it with another characteristic, namely, the ability to generate multiple wavelengths in the laser cavity, since it functions as a comb-like filter or selective element. A comb-like filter is produced as a result of the coupling between the fundamental mode and the higher-order mode of the cladding section. The interference between these modes occurs because of the phase difference between them (Ali et al., 2014; Harun et al., 2010; Jiang et al., 2007; Zhao et al., 2014b).

5.2 Q-Switched Erbium-Doped Fiber Laser

Fiber-laser-produced pulses have significant potential applications in many fields, such as spectroscopy, medicine, and optical communications (Huang et al., 2012; Rao et al., 2004; Skorczakowski et al., 2010). Generally, pulsed fiber lasers are divided into mode-locked and Q-switched lasers. Mode-locked lasers are used in some applications in which ultra-fast pulses are required. Although a Q-switched fiber laser has a lower frequency than a mode-locked laser in the kHz range, its pulse energy is higher. There are two main techniques for generating Q-switched pulsed lasing: active (Keller et al., 1996; Yubing et al., 2008) and passive (Liu et al., 2013a). Compared with actively Q-switched fiber lasers, passive laser systems have the advantages of simplicity of setup and compactness (Zhou et al., 2010), making them suitable for small-footprint applications. Most commonly, a carbon-based material is used as the SA to generate passive Q-switching, and in the case of evanescent field interactions, rolled carbon structures known as CNTs can be deposited around a microfiber (Kashiwagi & Yamashita, 2009) to achieve pulsed lasing. Graphene is a two-dimensional carbon material that has attracted the attention of researchers over the last few years in the fields of nanoelectronics and photonics by virtue of its unique properties, including a low threshold for saturable

absorption, an ultrafast recovery time and an ultra-broad wavelength-independent saturable absorption range from the visible to the THz region (Liu et al., 2012; Xie et al., 2012). Based on graphene, Q-switched pulsed lasers have been successfully demonstrated (Lee et al., 2013; Saleh et al., 2014; Sun et al., 2010a; Wang et al., 2012).

5.3 Deposition of Graphene Oxide Around an Optical Microfiber

First, a tapered optical fiber was fabricated using the heat-and-pull technique. A length of 1 cm of an uncoated SMF was clamped between two optical fiber holders. Then, the glass fiber was heated using a movable oxy-butane flame to soften it. It was then stretched to produce a microfiber with low loss (Harun et al., 2012a). The waist of the microfiber was measured to be 16 μm . The evanescent field outside such a microfiber can interact with the surrounding material when the fiber cladding diameter is decreased to less than 30 μm (Khazaeinezhad et al., 2015). Using a micro-pipette, 0.5 μl of a GO solution was dropped onto the microfiber's waist, and laser light was propagated into the fiber at the same time. Because of the evanescent field of the microfiber and the mutual interaction between the microfiber and the GO solution, a nonlinear SA formed around the microfiber (Jung et al., 2012). Compared with the case of direct interaction between the light and the SA, the optical damage threshold is higher when the evanescent field of the microfiber interacts with the SA along the interaction length in this way (Luo et al., 2015). The insertion loss of the GO-deposited microfiber was found to be 4.7 dB. **Figure 5.1(a)** shows the Raman spectrum of the GO solution. The spectrum exhibits two peaks, D and G. The D peak that was measured at 1355 cm^{-1} originates from the C-C bond, and the G peak at 1606 cm^{-1} is due to the first scattering of the E_{2g} phonon mode of sp^2 C atoms (Shahriary & Athawale, 2014; Sobon et al., 2012). **Figure 5.1(b)** presents an optical microfiber image of our tapered fiber deposited with GO over a length of approximately 20 μm .

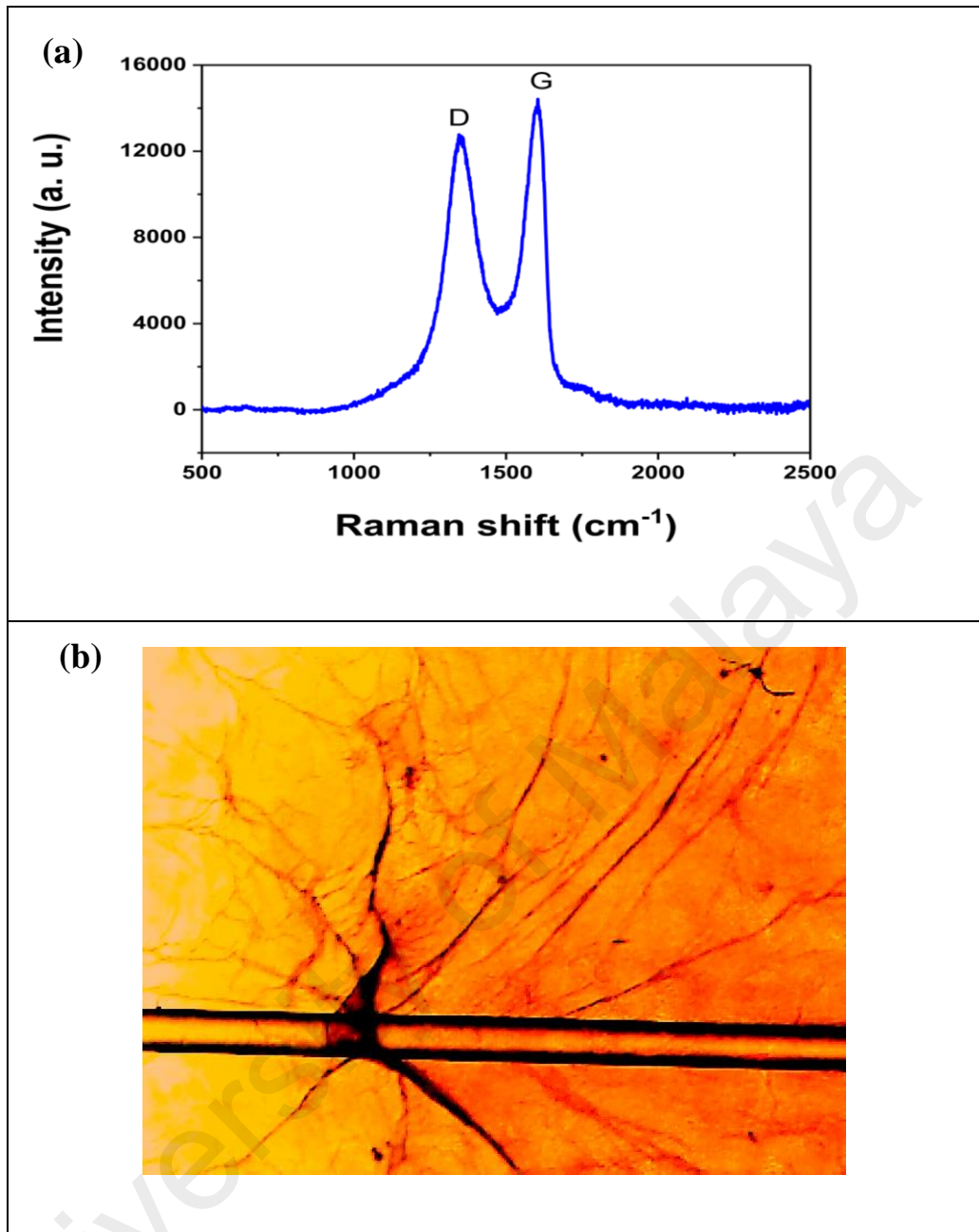


Figure 5.1: (a) Raman spectrum of the GOSA and (b) microscopic image of a microfiber deposited with the GOSA.

5.4 Experimental Setup

Figure 5.2 schematically illustrates the experimental setup for the proposed passively Q-switched pulsed fiber laser. A 980 nm laser diode was used to pump a 3 m long EDF (Fiber core Metro Gain M-12) that acted as a gain medium connected after a 980/1550 WDM. An ISO was used to propagate light unidirectionally; the setup also included a 90/10 coupler, the GO-deposited microfiber, and a PC to adjust the polarization state. A

3-dB coupler was connected to the 10 % output port to simultaneously monitor the wavelength and transient results. The results were recorded using an OSA (Yokogawa AQ6370C) and an RF spectrum analyzer, and the Q-switched pulses were recorded using a digital oscilloscope (Yokogawa DLM 2054).

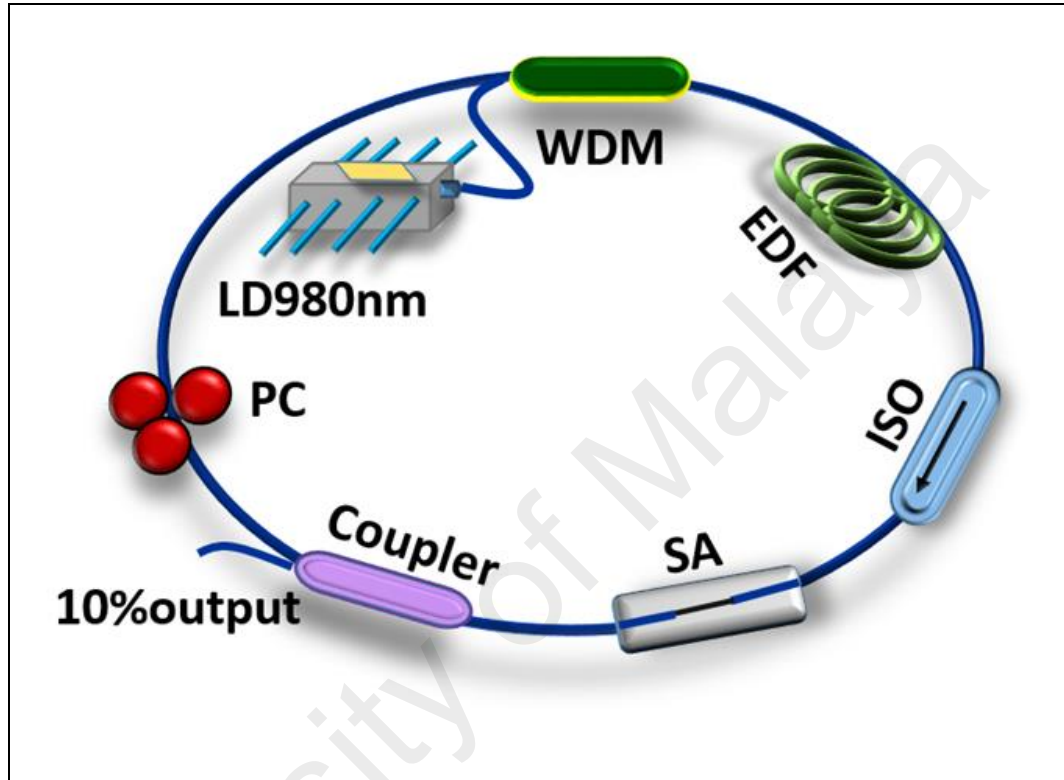


Figure 5.2: Scheme of the proposed passively Q-switched EDF laser.

5.5 Results and Discussion

Once Q-switched operation was initiated at a 56.17 mW pump power, broadening of the output spectrum was clearly observed, with a 3-dB bandwidth of 2.12 nm at the main peak centered on a wavelength of 1529 nm, as shown in **Figure 5.3**. In addition, the gain, as shown by the power peak at 1529 nm, increased when the pump power was enhanced to the maximum of 105.98 mW, with an increase in the 3-dB bandwidth to 2.44 nm. This broadening of the Q-switched output spectrum is related to the strong third-order nonlinear characteristics of GO (Zhao et al., 2014a).

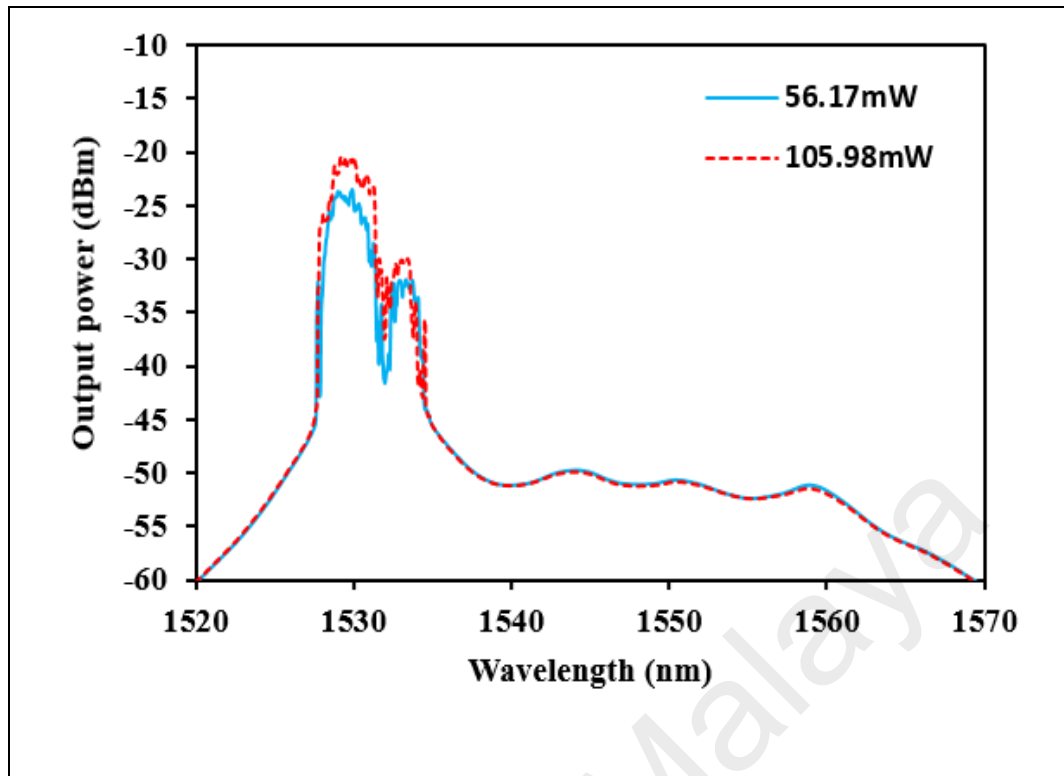


Figure 5.3: Optical spectra of the fiber laser at two different pump currents.

At the threshold pump power of 56.17 mW, the laser started to generate Q-switched pulsed lasing with a repetition rate of 37.06 kHz and a pulse duration of 26.97 μ s. When the pump power was increased from 56.172 mW to 105.98 mW, the repetition rate also increased. However, the pulse duration decreased. This phenomenon is illustrated in **Figure 5.4**. In this case, the PC was kept unchanged in its original position while the pump power was increased.

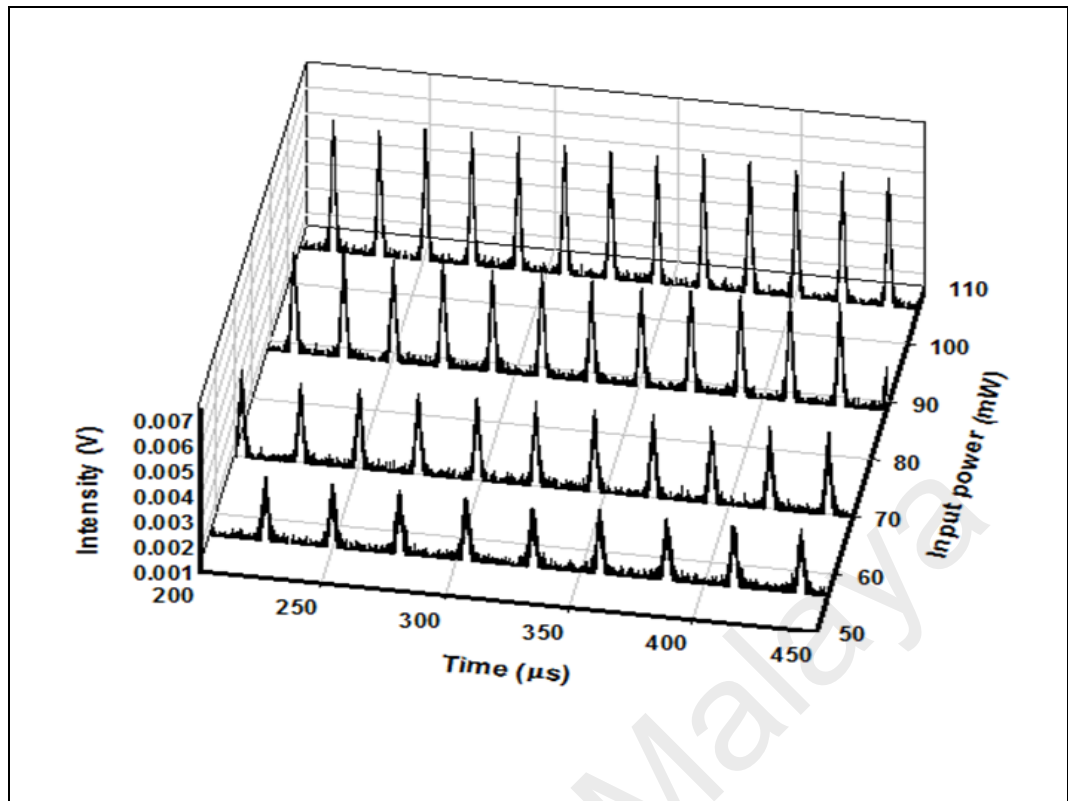


Figure 5.4: Q-switched pulse trains generated at different pump powers (56.17 mW, 69.85 mW, 88.36 mW and 105.98 mW).

Figure 5.5 shows the output pulse train in the frequency domain obtained from the radio-frequency (RF) spectrum analyzer. The spectrum (in the inset) indicates that the fundamental frequency is 43.57 kHz, and clearly defined pulses with an extinction ratio of -38 dB are evident at the corresponding harmonics. Moreover, the broadband RF spectrum presented in **Figure 5.5** shows no spectral modulation, indicating the stable repetition rate of the passively Q-switched lasing at a pump power of 88.36 mW.

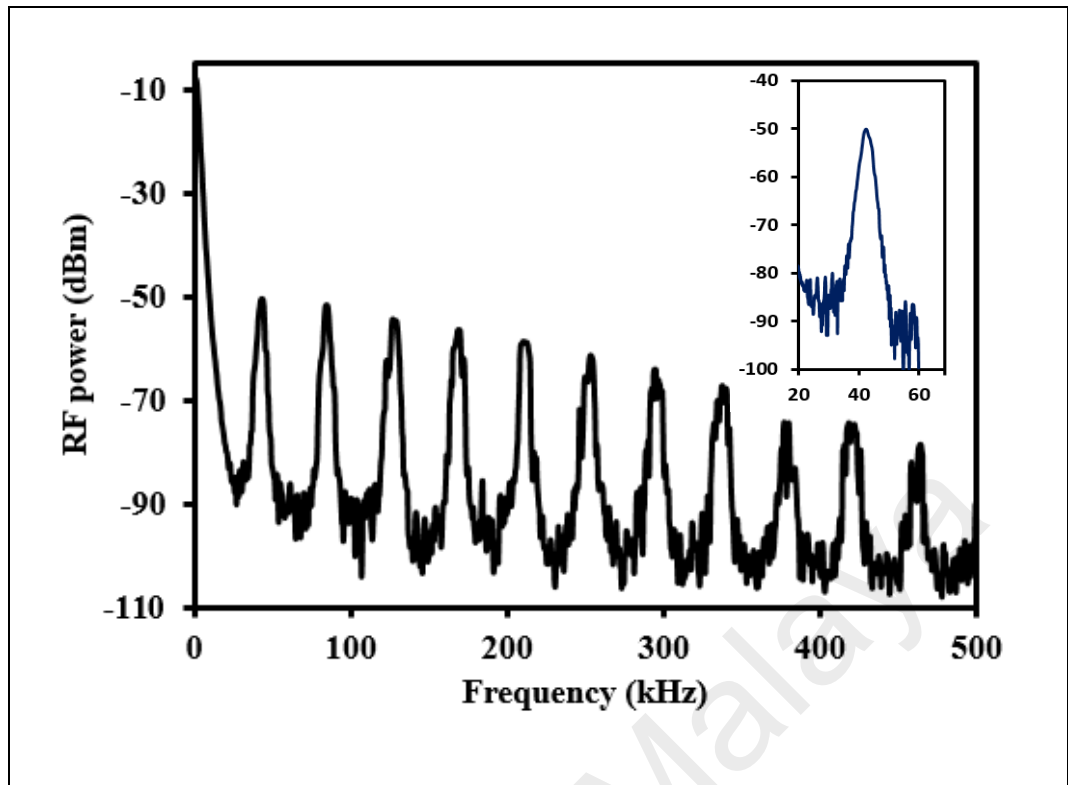


Figure 5.5: RF spectrum at a pump power of 88.36 mW.

Similar to other passively Q-switched lasers, when the pump power increases, the repetition rate of the GO-based Q-switched fiber laser also increases because of population inversion in the gain medium, which causes a shorter time to be required to reach the threshold when the pump power is increased (Men et al., 2013). Repetition rates from 37.06 kHz to 53.45 kHz were observed as the input power was increased from 56.17 mW to 105.98 mW. These repetition rates are higher than that reported in (Wang et al., 2012) and are comparable to the results reported in (Fan et al., 2014). Simultaneously, the pulse width in the same power range decreased from 3.67 μ s to 2.28 μ s, as shown in **Figure 5.6**.

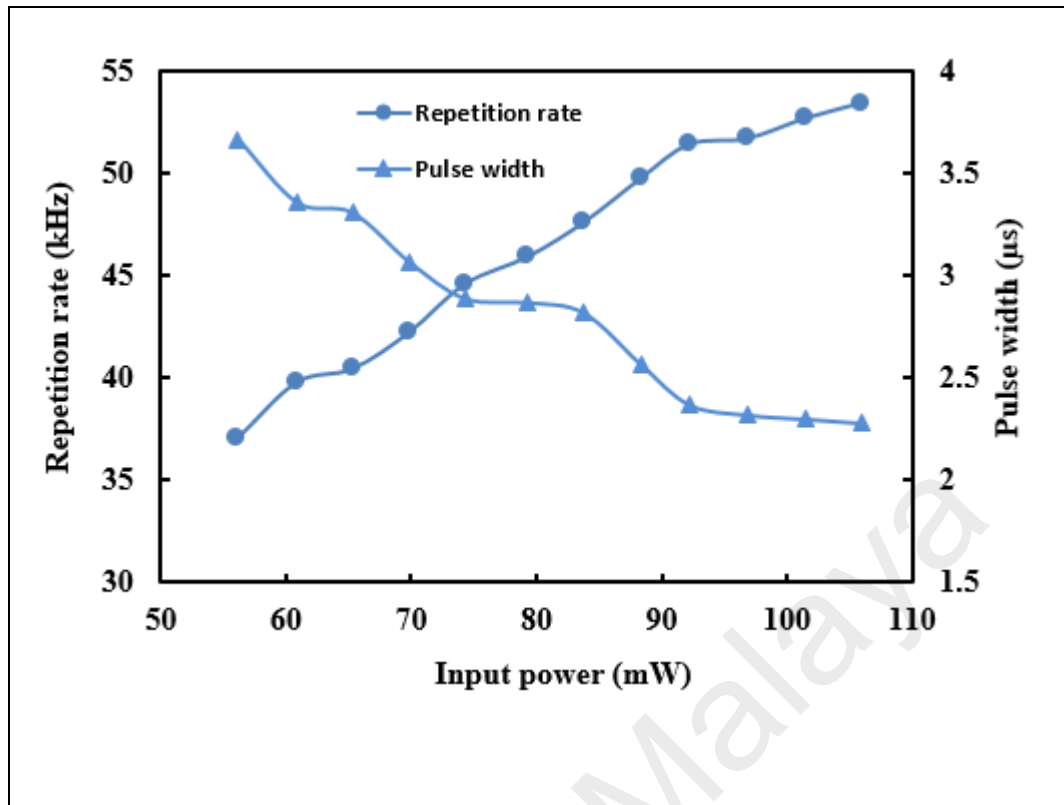


Figure 5.6: Repetition rate and pulse width as functions of the input power.

Figure 5.7 shows the pulse energy and output power of the pulsed laser as a function of the pump power. Experimentally, when the pump power increases, more electrons fill up the energy state. As a result, the SA can saturate more quickly. Therefore, as the pump power was increased, the pulse frequency and pulse energy also increased monotonically. A pulse energy of 0.78 nJ was achieved at the maximum input power of 105.98 mW, whereas the maximum output power was 0.042 mW. However, with any further increase in the pump power, the Q-switched pulsed lasing would become unstable or even disappear. The efficiency of Q-switched pulsed lasing is expected to be further improved by optimizing the SA, microfiber and laser cavity design.

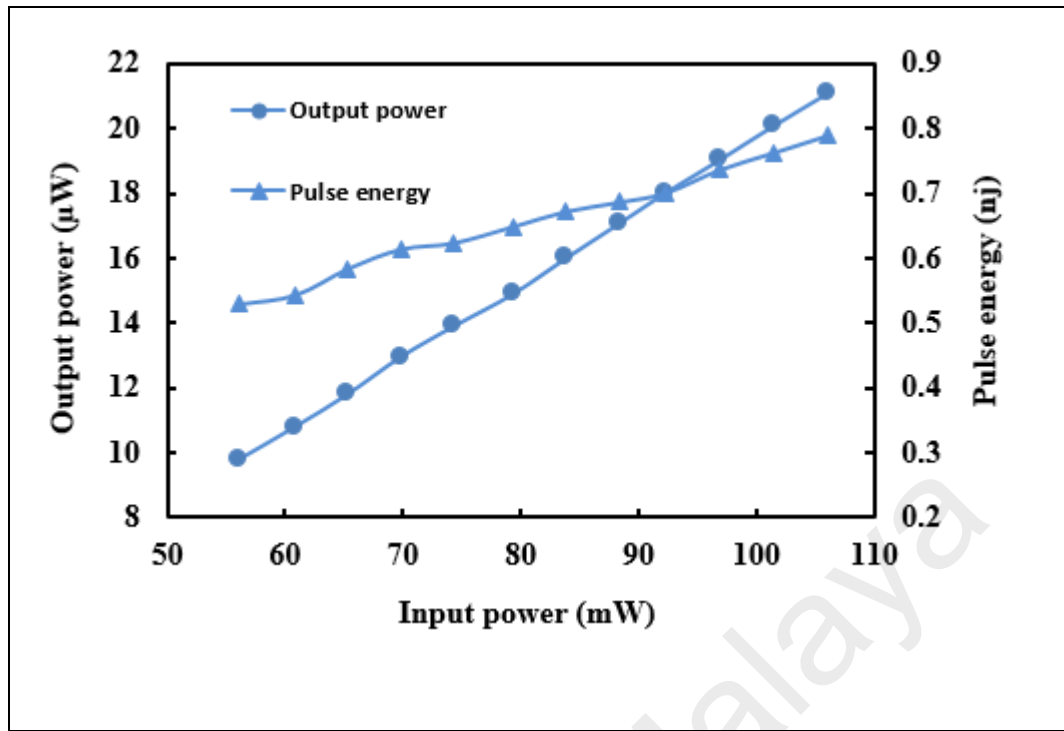


Figure 5.7: Pulse energy and output power as functions of the input power.

5.6 Dual-Wavelength Q-Switched Pulsed Fiber Laser

Dual-wavelength Q-switched erbium-doped fiber lasers (EDFLs) have attracted significant interest in recent years because of their potential applications in sensing, medicine, materials processing and optical communications (Harun et al., 2007; Skorczakowski et al., 2010; Talaverano et al., 2001; Walsh, 2010). Moreover, dual- and multi-wavelength Q-switched pulse lasers have already been used in many applications, such as airborne lidar, terahertz generation, multiphoton dissociation of molecules, and other applications in nonlinear optics or sensing (Ahmad et al., 2010; Liu et al., 2013). Various techniques have been employed to generate dual wavelengths in fiber lasers, such as those based on a single FBG in a linear cavity for tunable and switchable dual-wavelength generation (Feng et al., 2004) or on a double-ring filter (DRF) (Yeh et al., 2007). Recently, because of their small size, compact structure and low cost, microfibers with various structures have also begun to be used in dual-wavelength fiber lasers (Ahmad et al., 2015; Ali et al., 2014). The passive Q-switching technique based on an SA is a

powerful technique for achieving very stable pulses compared with active Q-switching, which requires additional components such as mirrors or lenses. Traditionally, SESAMs are widely used to produce Q-switched pulsed lasing (Ahmad et al., 2014a; Wu et al., 2013). However, the use of SESAMs suffers from several limitations, such as a narrow tuning range, complexity of fabrication/packaging, and a high possibility of optical damage to the semiconductor mirror, which limits the output energy of the generated pulses (Kurkov, 2011). A CNTs have been employed as SAs in laser cavities for pulse production because of their variable size and their ability to generate pulses at different wavelengths (Harun et al., 2012b; Liu et al., 2013a). However, the operating wavelength is strongly dependent on the CNT dimensions (Luo et al., 2012a). Recently, graphene, a monolayer of carbon atoms, has attracted considerable research interest as a potential replacement for SESAMs because of its various prominent features, such as a low saturation intensity, good linear and nonlinear optical characteristics, low cost and high flexibility regarding its incorporation into other photonic structures (Yang et al., 2014). Based on graphene saturable absorbers (GSAs), which can suppress the mode competition of EDFs by virtue of their high third-harmonic-order optical nonlinearity, dual- and multi-wavelength Q-switching has been demonstrated by utilizing a FBG or a photonic crystal fiber with GO (Ahmad et al., 2014; Jun-Qing et al., 2012; Luo et al., 2010). In essence, there are two main methods of incorporating graphene onto a fiber core. The first is by attaching a graphene film to the face of a fiber ferrule (Zhang et al., 2010). The second is by optically depositing a graphene solution around the waist of a microfiber or onto a side-polished fiber (Zhou et al., 2012).

5.7 Experimental Setup and Fabrication

Figure 5.8 shows the EDF ring laser setup used in this experiment, with a GSA and a tapered fiber. The fiber laser ring cavity consisted of a 980 nm LD with a maximum pump power of 600 mW connected to the input port of a 980/1550 WDM coupler. The output

port of the WDM was fusion spliced to a 3 m EDF that acted as a gain medium and was then connected to a tapered optical fiber. To produce a Q-switched laser pulse train, a small piece of GSA film used as a Q-switching element was placed between two fiber ferrules inside the Sagnac loop using a 50/50 coupler. A 90:10 coupler was used to extract 10 % of the laser light from the cavity to record the output spectrum while 90 % of the power was allowed to circulate inside the cavity. An optical isolator was inserted to guarantee the unidirectional propagation of light to enhance the stability of the generated laser output by reducing the back-reflection emission inside the cavity (Ahmad et al., 2005). In addition, a PC was used to control the polarization state of the laser beam inside the cavity. To enable precise measurements, a 50/50 coupler was utilized to distribute the cavity output power equally between two paths: one port was connected to an OSA (Yokogawa, AQ6370C) to record the laser output spectrum, and the second port was used to test the output power using an optical power meter (Thorlabs, S144C) or the time-domain spectrum using a digital oscilloscope (Yokogawa DLM 2054) with a photodetector (Thorlabs, DET01CFC). Except for the 3-m EDF gain medium, all fibers utilized in laser setup were SMF-28 fibers.

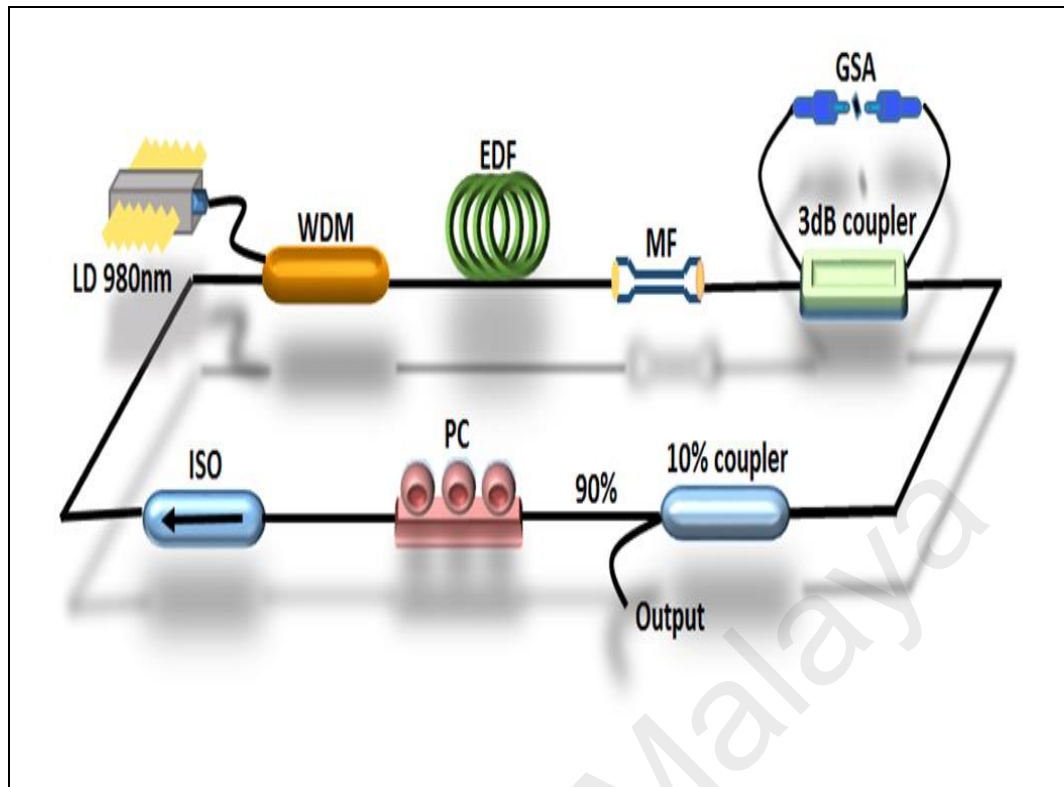


Figure 5.8: Experimental setup for the dual-wavelength Q-switched EDF with a tapered fiber and a GSA.

Our tapered optical fiber was fabricated using the flame brushing technique (Ab Razak et al., 2015). A standard single-mode fiber was stripped of its coating jacket and cleaned using ethanol. Then, it was placed horizontally on two motorized holders. Throughout the fabrication process, a flame, which was produced by burning a combination of butane and oxygen, with a width of approximately 5 mm was used to apply heat along the stripped section of the SMF. Simultaneously, the fiber was elongated by stretching. The advantage of using a moving flame is to ensure a uniform temperature around the fiber, so that the fabricated microfiber will have good optical characteristics (Harun et al., 2010). The diameter of the nonadiabatic tapered fiber waist was 12 μm , and the waist length was 25 mm. To achieve light interference inside the comb-like filter, the higher-order modes of the fiber core were excited in the tapered section as the injected light traveled from the untapered fiber into the tapered region. At the other end of the tapered region, where the light reentered an untapered fiber section, the fundamental and higher-order modes

recoupled, resulting in an interferometric pattern because of the large difference in refractive index between air and glass (Yadav et al., 2014). **Figure 5.9** presents the transmission spectrum of the tapered fiber. It shows an interferometric pattern with a spacing of approximately 5 nm between two consecutive peaks. The inset image shows an optical microscopic image of the fabricated tapered fiber. The peak output was measured to be approximately -22 dBm at a wavelength of 1532 nm.

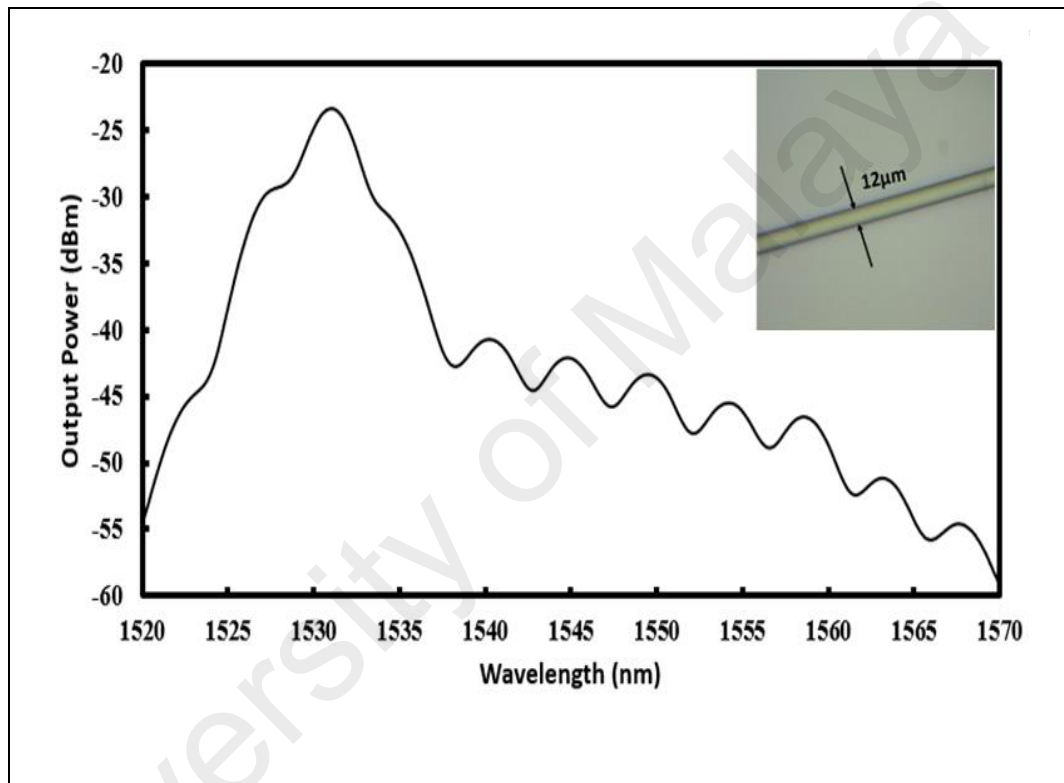


Figure 5.9: Output optical spectrum of the fabricated tapered fiber (inset: microscopic image of the tapered fiber, with a diameter of 12 μm).

To prepare the Q-switching element, an index-matching gel (IMG) was applied to the end surface of the fiber, and this surface was then immersed in a solution containing graphene flakes and allowed to dry at room temperature. The RI of fiber-optic silica is approximately 1.463, and the IMG had an approximately similar RI. **Figure 5.10** shows the Raman spectrum of the deposited graphene. The spectrum exhibits three peaks located at 1350, 1580 and 2700 cm^{-1} . The second and third peaks are commonly called the G and

2-D peaks, respectively. The sample used here is the same as that reported in a study by (Muhammad et al., 2012).

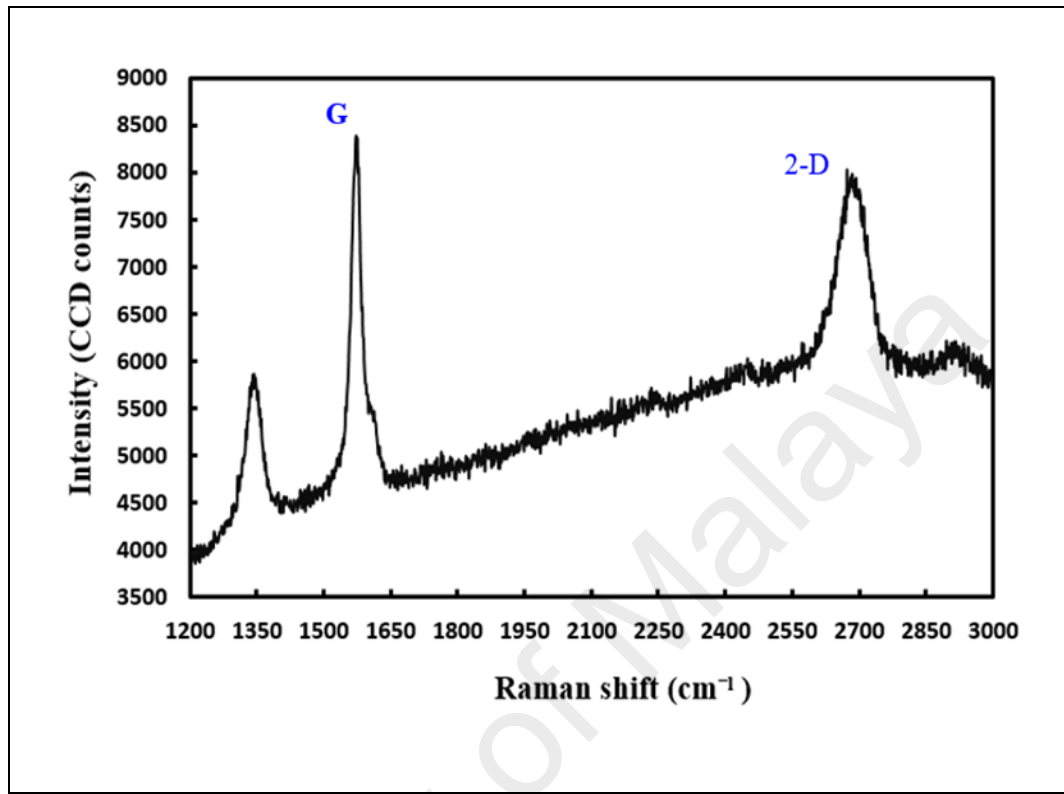


Figure 5.10: Raman spectrum of the deposited graphene saturable absorber.

5.8 Results and Discussion

The proposed stable Q-switched pulsed laser with dual-wavelength output begins to operate at a threshold pump power of 83.82 mW. **Figure 5.11(a)** shows the dual-wavelength optical spectrum produced by the tapered fiber, where the wavelength peaks are centered at 1549.34 nm and 1559.51 nm. These two peaks correspond to output powers of -21.10 dBm and -17.45 dBm, respectively. The generated Q-switched laser pulses had a repetition rate of 15.87 kHz, as shown in **Figure 5.11(b)**.

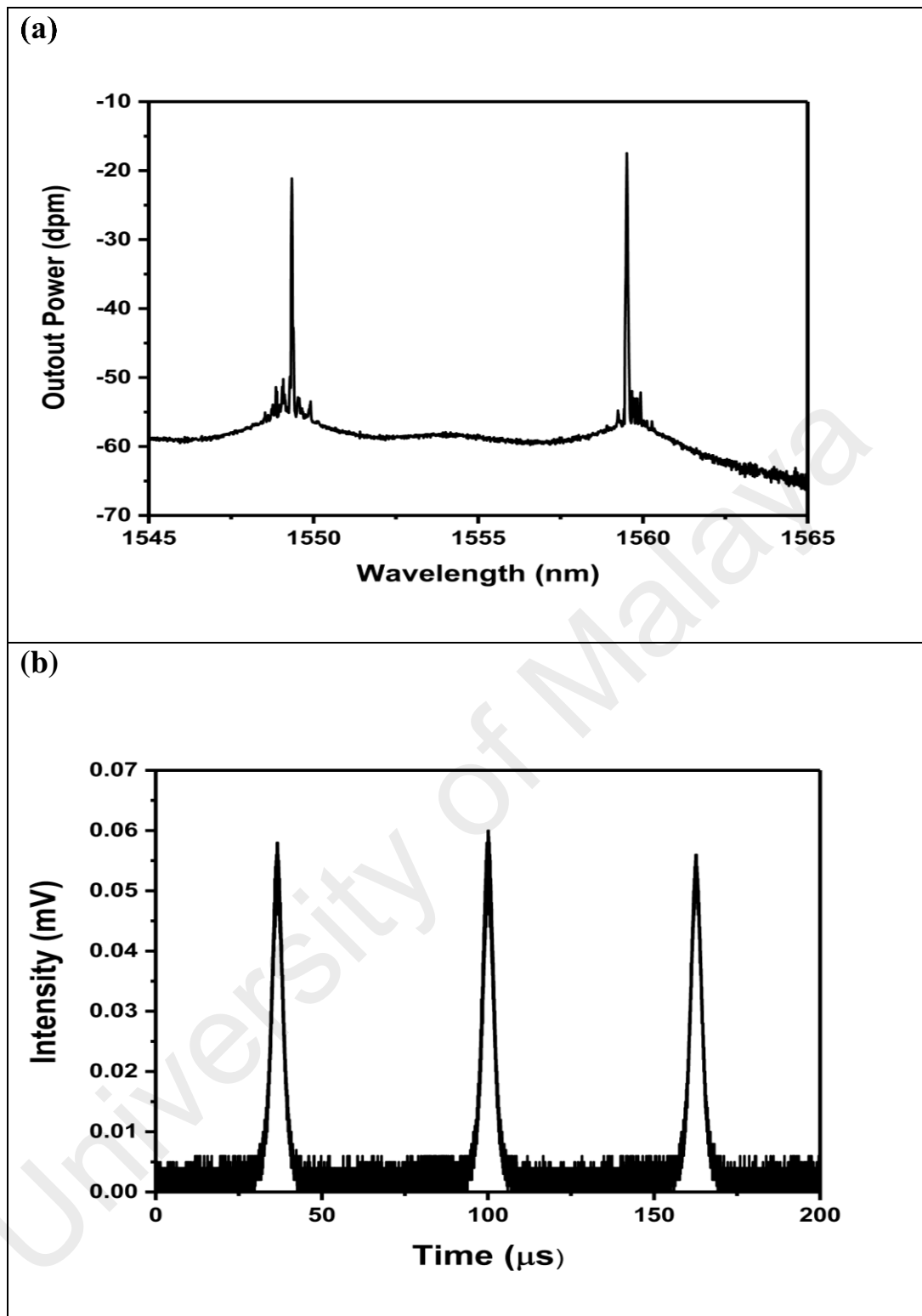


Figure 5.11: (a) Dual-wavelength optical spectrum and (b) passively Q-switched pulse train, at the threshold pump power of 83.82 mW.

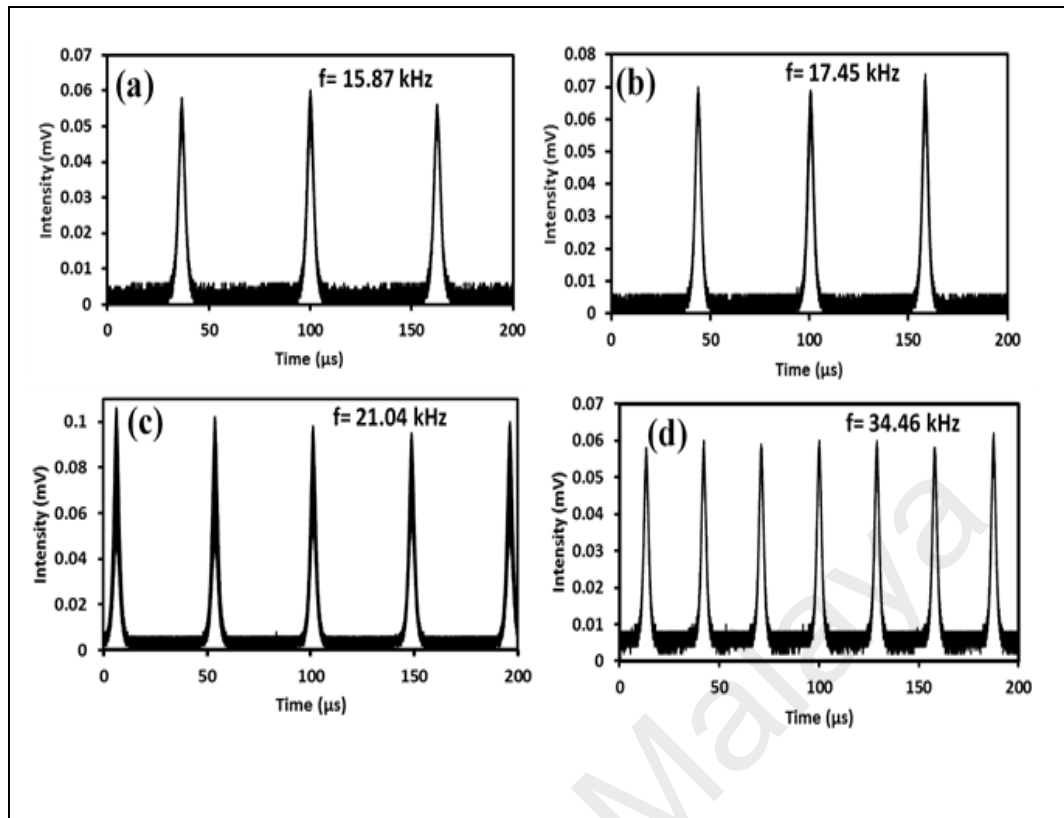


Figure 5.12: Q-switched pulse trains at different pump powers: (a) 88.36 mW, (b) 96.86 mW, (c) 115.91 mW and (d) 135.93 mW.

As the input power was gradually increased from 88.36 to 96.86, 115.91, and 135.93 mW, the Q-switched pulse trains were recorded using an oscilloscope. By varying the pump power, the repetition rates could be tuned from 15.87 kHz to 34.46 kHz, as shown in **Figure 5.12 (a,b,c,d)**. These results represent typical Q-switched pulses, where the frequency varies with different input powers.

Figure 5.13 presents the relations between the measured repetition rate and pulse width of the Q-switched laser setup as functions of the input power. The repetition rate linearly increased with the increase in the input power. Meanwhile, the pulse width linearly decreased with the input power. As the input power was increased, the gain medium (EDF) eventually reached saturation state because of the enhancement of the population excitation process. Therefore, narrower pulse widths and higher pulse repetition rates were obtained. When the pump power was increased from 83.82 mW to

135.93 mW, the repetition rate also increased from 15.8 to 34.4 kHz, whereas the pulse width decreased from 3.8 to 2.7 μs as the pump power was increased in the range of Q-switching operation. The shortest pulse width was 2.7 μs , which is superior to the result reported in (Ahmad et al., 2015a). This effect occurred as a result of gain compression in the Q-switched fiber laser (Herda et al., 2008). A narrower pulse width could be achieved by reducing the length of the optical fiber in the laser setup or by using an optical fiber with a higher dopant concentration. During this experiment, no mode-locking phenomenon was observed.

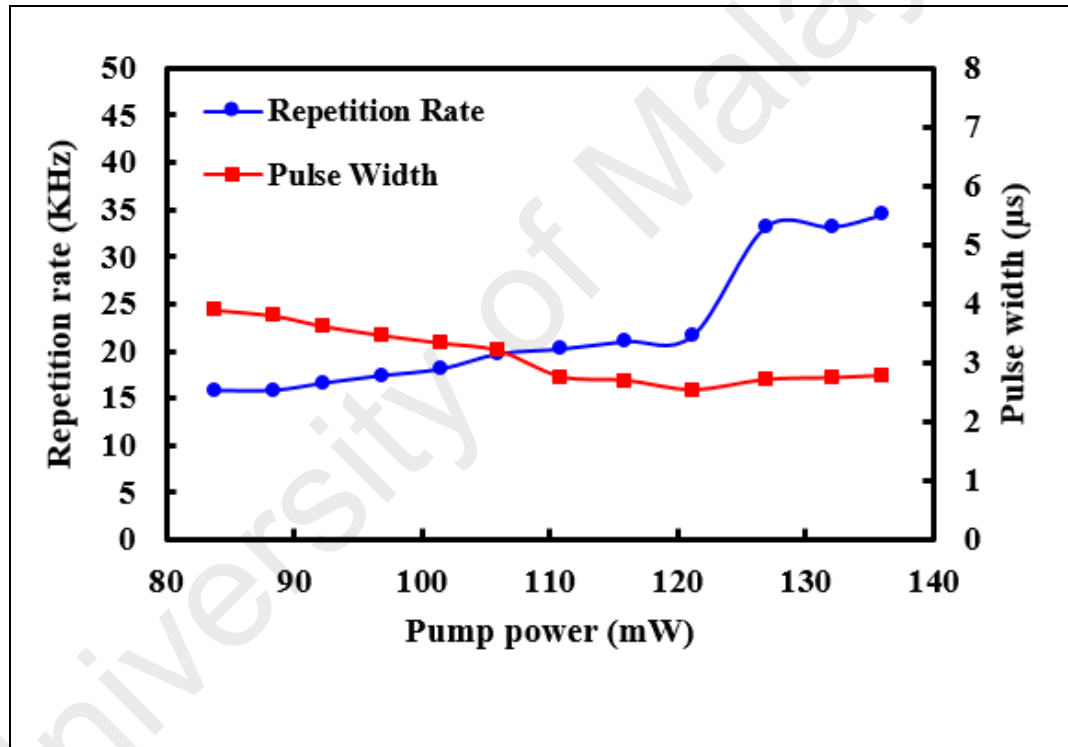


Figure 5.13: Repetition rate and pulse width of the Q-switched pulsed laser setup versus the pump power.

Figure 5.14 shows the trends of average output power and pulse energy with increasing pump power, where pulse energies between 4.2 nJ and 5.54 nJ were recorded. These values are much higher than the result reported in a previous study (Ahmad et al., 2015a). Simultaneously, the output power increased monotonically from 0.07 mW to 0.14 mW.

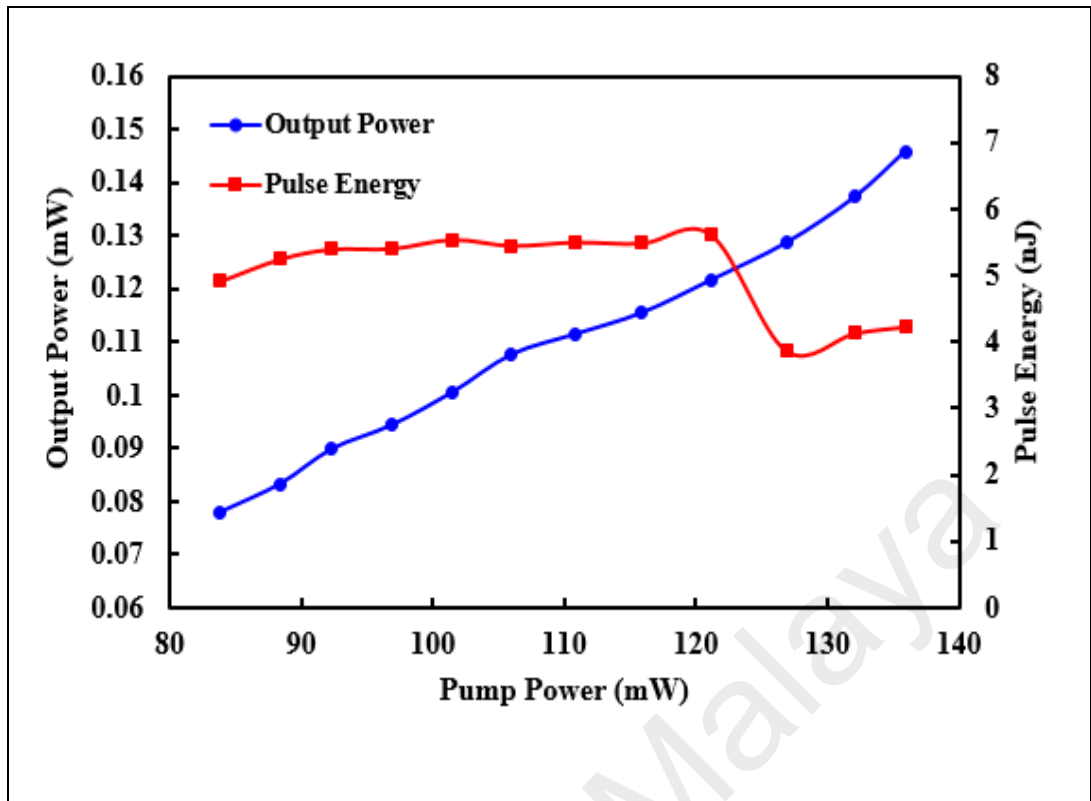


Figure 5.14: Pulse energy and total output power versus the pump power in the Q-switched pulsed laser setup.

The stability of the measured dual-wavelength output power was verified by recording data over a period of 16 minutes at a pump power of 100 mW, as shown in **Figure 5.15**. It was found that the shape of the pulse train did not change over this observed duration. This result indicates that the proposed setup demonstrates stable lasing behavior that will be useful for many lasing applications.

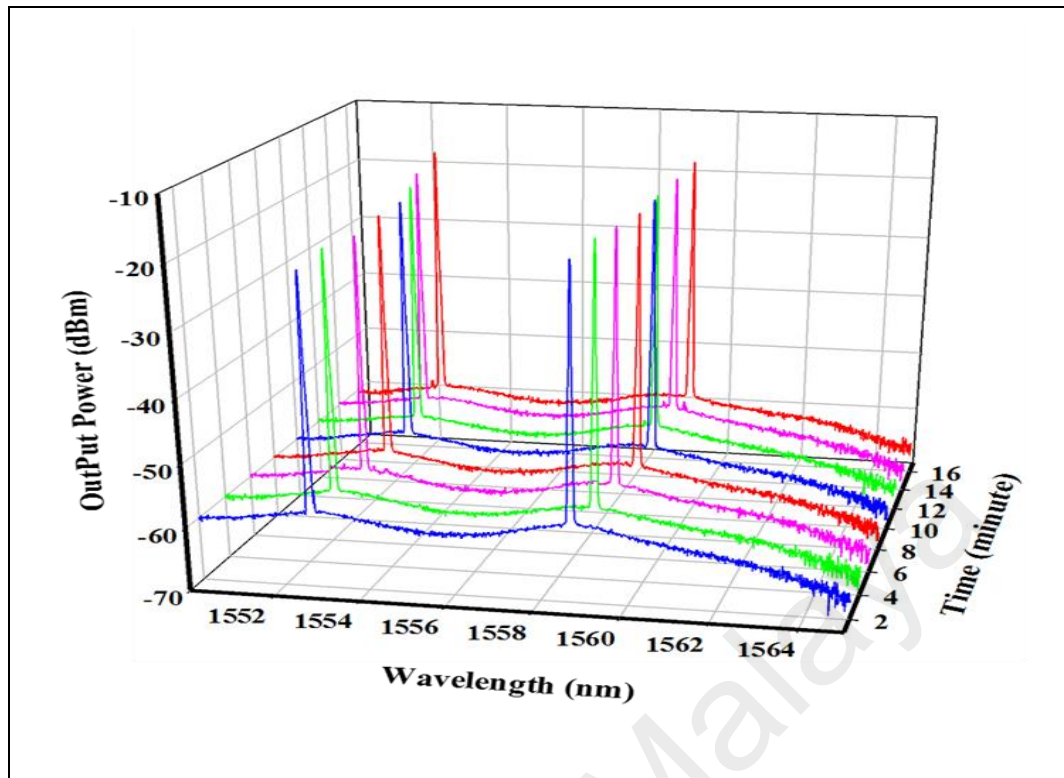


Figure 5.15: Test of the stability over time of the output spectrum of the dual-wavelength Q-switched laser setup.

5.9 Generation of Mode-Locked Pulsed Lasing by Utilizing the Interaction of an Evanescent Field with Graphene Oxide

By coupling a GO solution with the evanescent light field of a side-polished fiber, mode-locked pulsed lasing was successfully demonstrated based on light-matter interaction in this experiment. This GO-coated side-polished fiber is not only capable of enabling passive mode locking in an anomalous-dispersion EDF laser but is also able to address the problem of the significant likelihood of thermal damage that arises when sandwiching a SA directly between two fiber ferrules to generate pulses. The graphene oxide solution that was deposited on the side-polished (or D-shaped) fiber served as a passive SA and coupled with the evanescent light field of the side-polished fiber to generate mode-locked laser pulses.

5.10 Experimental Setup

Figure 5.16 shows the schematic diagram of the mode-locked fiber laser setup using the D-shaped GO SA. A 980-nm laser diode (LD) was used as the pump source, which was connected to a 980/1550 WDM. A 3 m EDF was connected after the WDM to amplify the signal. An isolator was included in the cavity to ensure a unidirectional flow of the propagating light. The fabricated D-shaped GO SA for mode-locked pulse generation was placed between the ISO and a PC, which was used to control the polarization state of the light. A 95:5 coupler was used, whereby 95 % of the light was coupled back into the cavity and 5 % of the light was extracted as output. The output was measured using an OSA (YOKOGAWA, AQ6370C), an oscilloscope (YOKOGAWA, DLM2054), an RF spectrum analyzer (Anritsu, MS2683A), an autocorrelator (Alnair Labs, Hac-200-05-Fs) and an optical power meter (Thorlabs, S144C). A high-speed photodetector (Thorlabs, D400FC) was used to measure the pulses through the oscilloscope and the RF analyzer. The entire cavity was designed using SMF-28 fibers, with the exception of the gain medium. The total length of the laser cavity was measured to be 23.28 m.

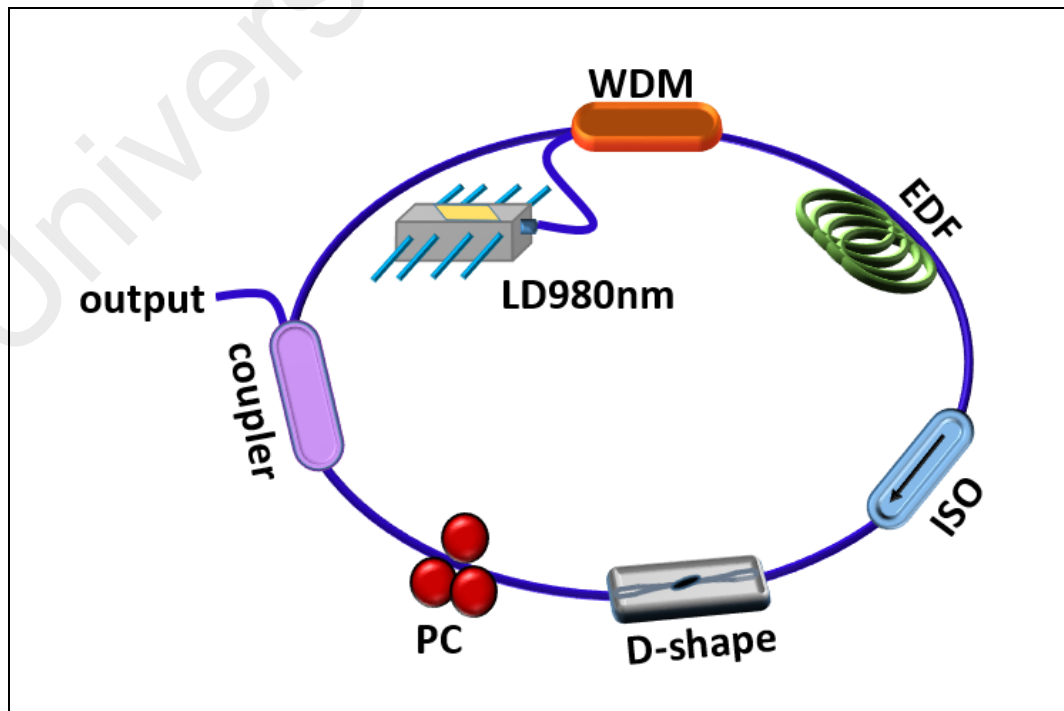


Figure 5.16: Mode-locked EDF laser based on a GO-coated D-shaped fiber.

Figure 5.17 shows the Raman spectrum of the GO. Two main peaks are evident in the spectrum (the D peak at 1356.89 cm^{-1} and the G peak at 1603.3 cm^{-1}). The D band originated from the structural imperfections created by the attachment of hydroxyl and epoxide groups to the carbon basal plane. Meanwhile, the G band corresponds to the ordered sp^2 -bonded carbon (Xu et al., 2012).

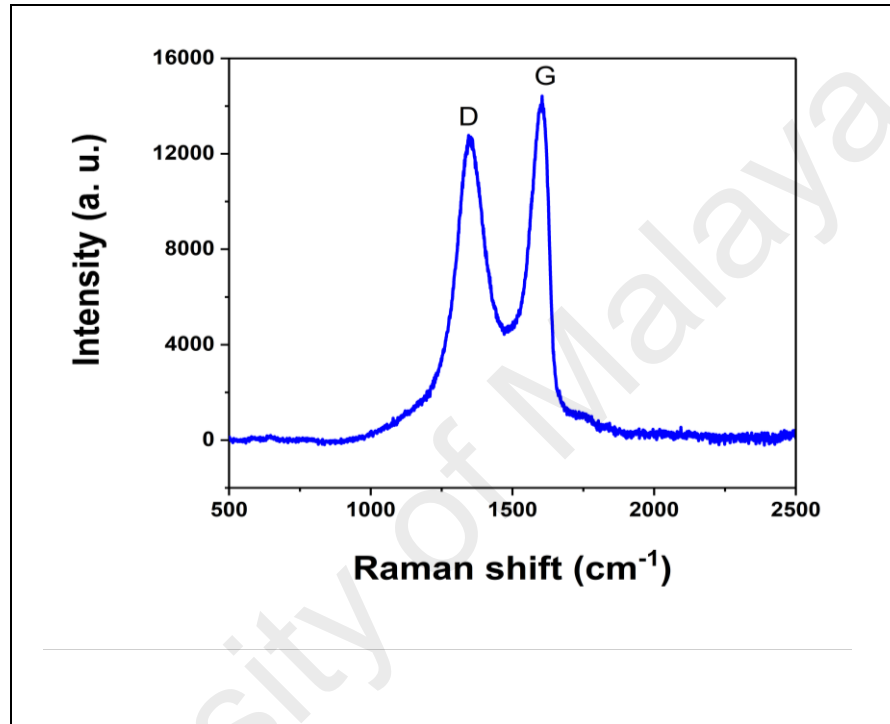


Figure 5.17: Raman spectrum of graphene oxide.

5.11 Results and Discussion

Stable mode-locked operation in the anomalous dispersion regime was observed at an input power of 74.32 mW after the adjustment of the intra-cavity polarization state. A mode-locking pattern was observed over a wide range of input power levels (74.32 mW to 214.52 mW). The optical spectrum was recorded at seven different power levels (74.32 mW, 96.86 mW, 121.17 mW, 144.03 mW, 167.23 mW, 188.03 mW and 214.52 mW) to observe the output variations, as depicted in **Figure 5.18**. A broader 3 dB bandwidth and a higher intensity were observed as the power level increased. Kelly sidebands appeared during the experiment, confirming the occurrence of soliton-regime mode-locking

operation (Lin & Lin, 2013). For demonstration purposes, all mode-locking characteristics were recorded at an input power of 167.23 mW.

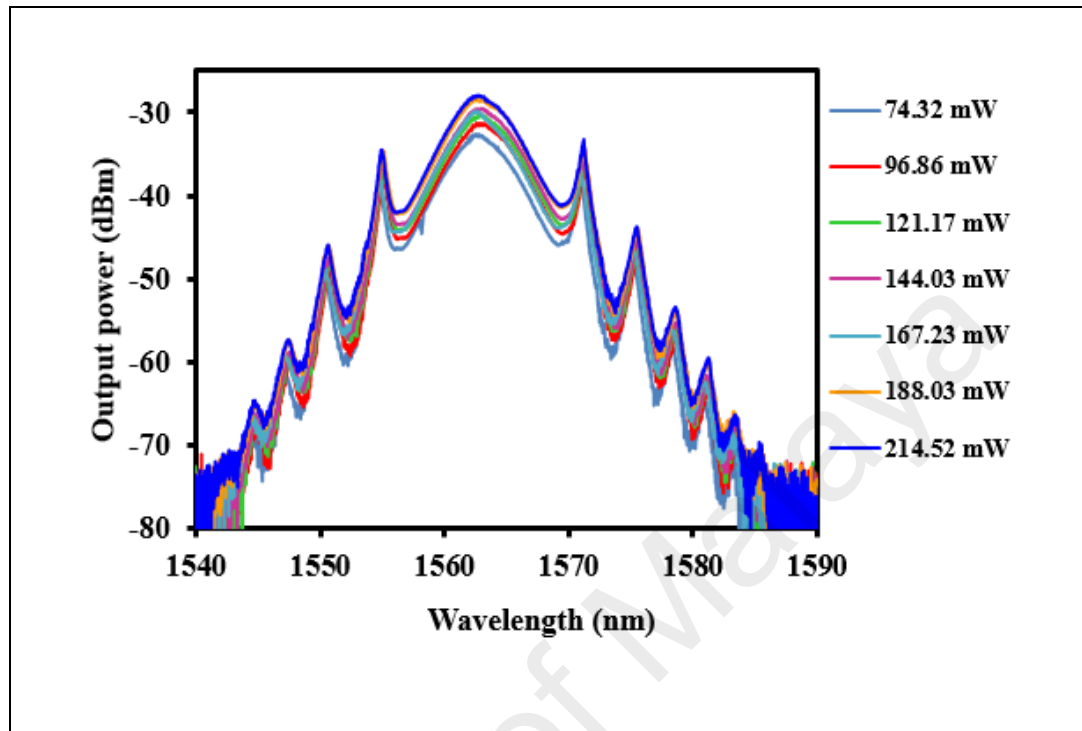


Figure 5.18: Optical spectra corresponding to the mode-locked pulses produced at different pump powers.

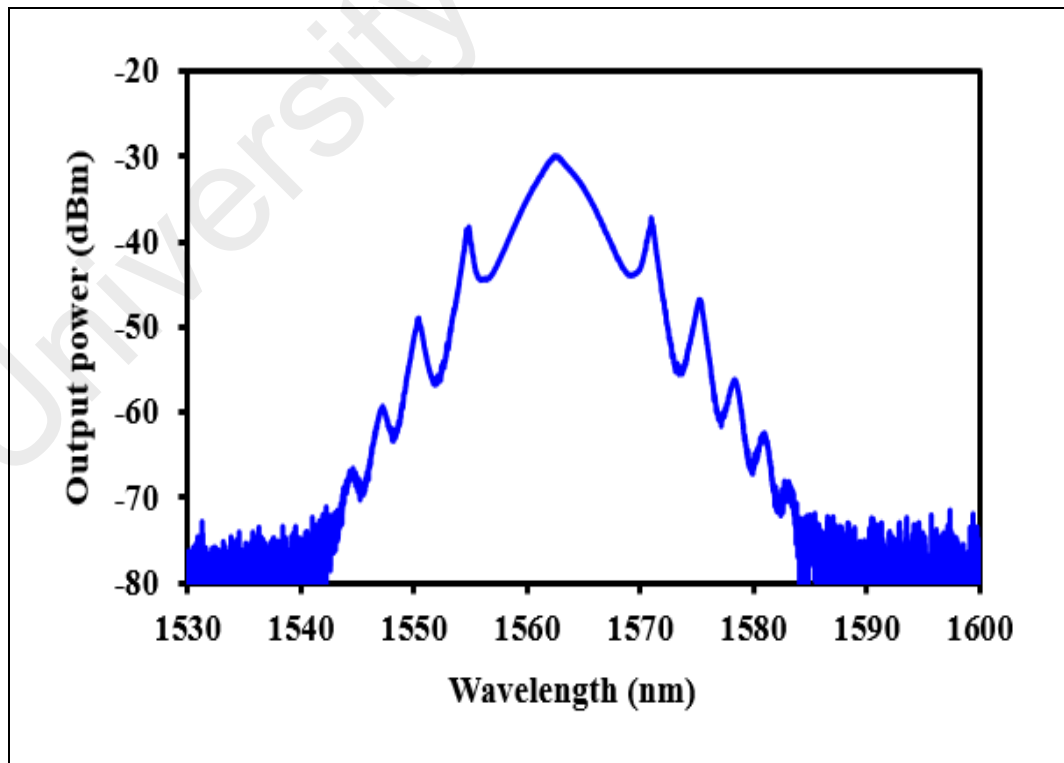


Figure 5.19: Spectral properties of the mode-locked pulses measured through the OSA.

Figure 5.19 depicts the output spectrum measured through the OSA. A 4.2 nm wide 3 dB spectral bandwidth was achieved with a central wavelength of 1565 nm. The measured 3 dB spectral bandwidth was much broader than that previously reported in (Song et al., 2010), where a 3 dB bandwidth of 1.96 nm was recorded, also using a side-polished fiber. The pulse train was measured using the oscilloscope connected to the high-speed photodetector. The resulting pulses are presented in **Figure 5.20**. A round trip time of 111.71 ns was achieved, which corresponds to a repetition rate of 8.95 MHz. This result is consistent with the cavity length and was verified using the following equation:

$$\text{Repetition rate} = \frac{c}{nL} \quad (5.1)$$

where c is the speed of light (3×10^8 m/s), n is the refractive index of the medium (1.44), and L is the length of the cavity (23.27 m). The repetition rate of 8.99 MHz recorded in our experiment is higher than the repetition rate reported previously in (Song et al., 2010), which was 6.99 MHz.

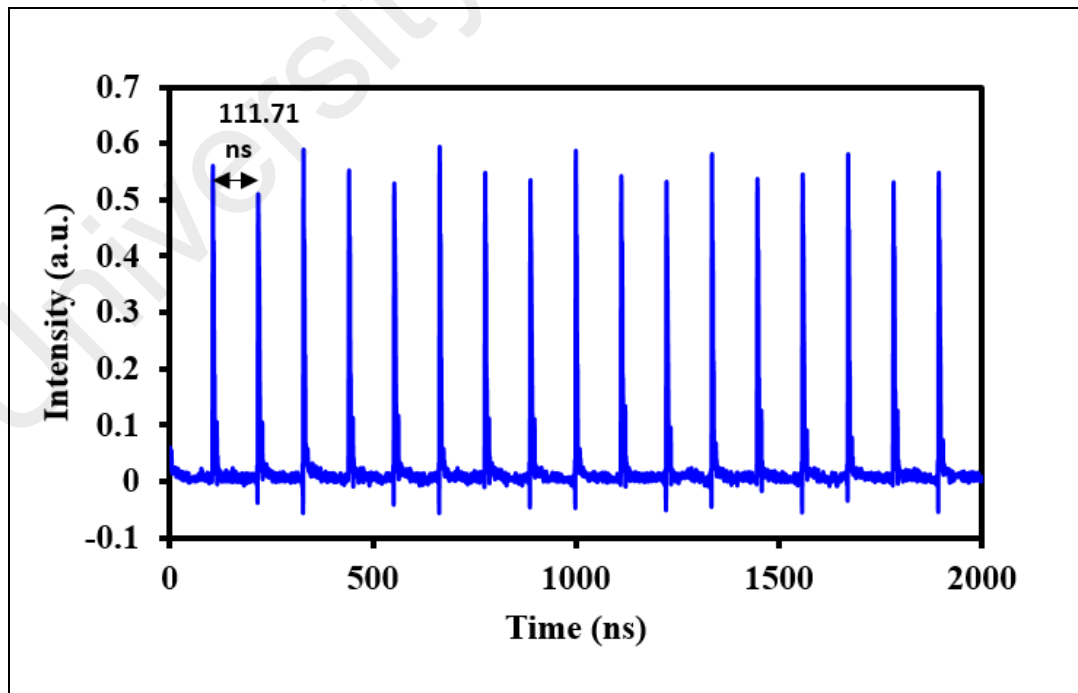


Figure 5.20: Mode-locked pulse train recorded at a pump power of 167.23 mW.

The pulse train was verified using the RF analyzer. A pulse repetition rate of 8.95 MHz was determined from the RF spectrum, as observed in **Figure 5.21**. The resolution bandwidth (RBW) during the measurement was 300 Hz. The RF spectrum over a wider range (up to 100 MHz), for which the RBW was recorded to be 0.3 MHz, is also provided as an inset in **Figure 5.21**. An acceptable signal-to-noise ratio (SNR) of 49.65 dB was measured during the experiment.

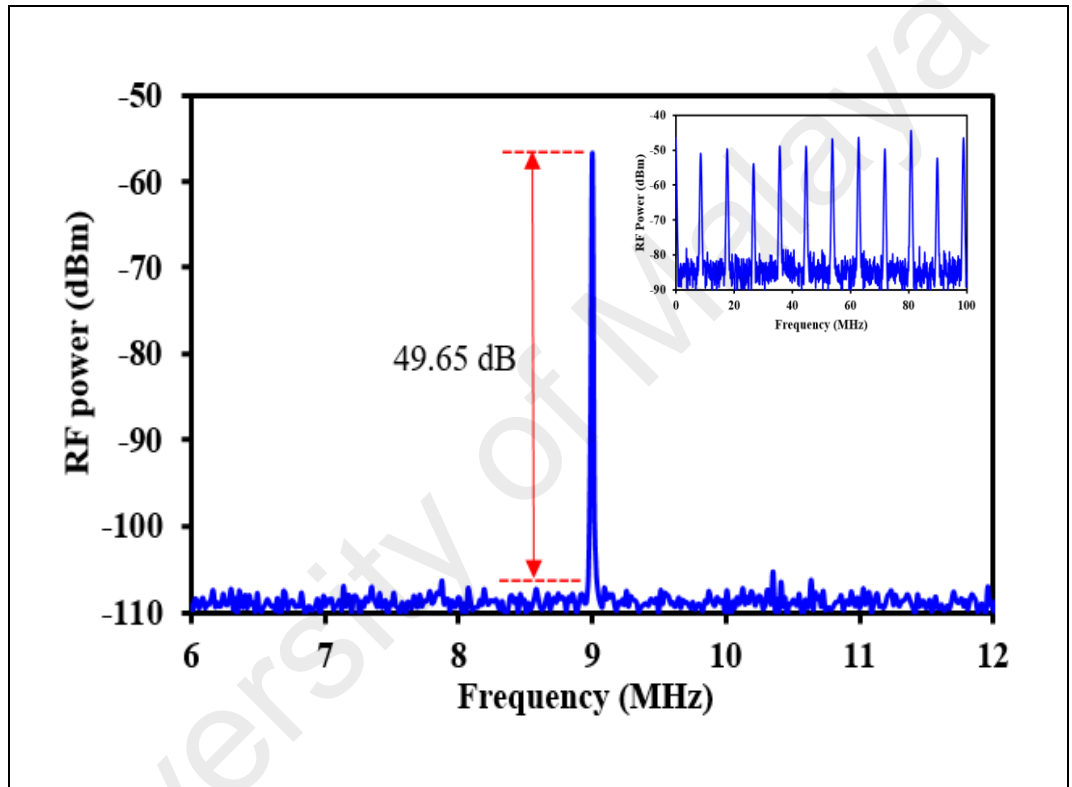


Figure 5.21: Radio-frequency spectrum.

The pulse width was observed using the autocorrelator and is presented in **Figure 5.22**. Since the cavity was operating in the soliton regime, sech^2 curve fitting was used as a reference. The full width at half maximum (FWHM) was recorded to be 1.05 ps. The pulse width was much shorter than value reported in a previous study (Song et al., 2010), which was 1.3 ps. The time-bandwidth product (TBP) was calculated using the following equation:

$$\text{TBP} = \text{Bandwidth} \times \text{Pulse width} = 0.522 \text{ THz} \times 1.05 \text{ ps} = 0.548 \quad (5.2)$$

This means that the pulses were slightly chirped. Notably, the ideal sech^2 pulse has a TBP of 0.315 (Paunescu et al., 2004).

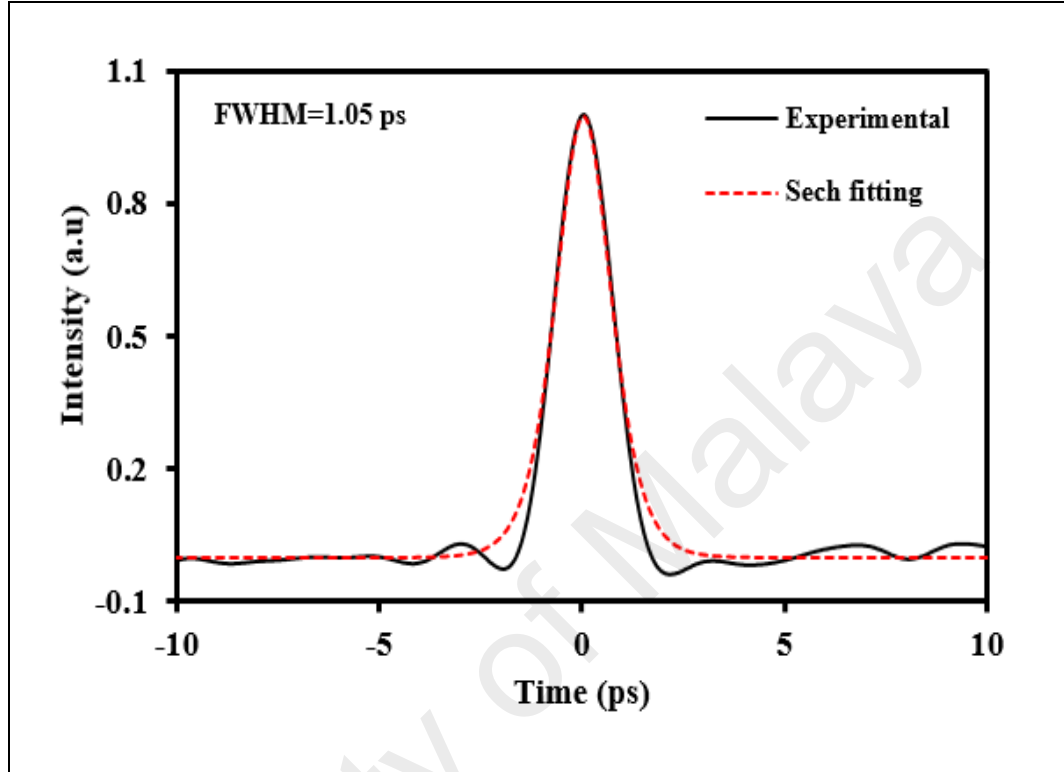


Figure 5.22: Autocorrelation trace with sech^2 profiling.

The laser efficiency was examined over a broader range of input power levels. **Figure 5.23** shows the measured output powers that correspond to different input power levels. It is apparent that when the pump power was increased from 74.32 mW to 214.52 mW, the measured output power also increased from 218.27 μW to 660.1 μW . The laser showed an efficiency of 0.32 % at an input power of 167.23 mW. This study was focused on mode-locked pulses. Thus, we did not consider different polarization orientations. First, a mode-locked spectrum was achieved by adjusting the polarization state using the PC, and the established polarization state was then maintained throughout the experiment. A mode-locked pattern was observed in the input power range of 74.32 mW to 214.52 mW.

The laser stability was studied over a period of 30 minutes. This stability measurement was performed at a pump power of 167.23 mW, corresponding to a laser operating current of 400 mA. The laser demonstrated good stability, with only a minor shift in the central wavelength and 3 dB bandwidth. The central wavelength varied only in the range of 1562.54 nm to 1562.94 nm, whereas the 3dB bandwidth varied only between 4.07 nm and 4.19 nm. **Figure 5.24** represents the stability of the laser.

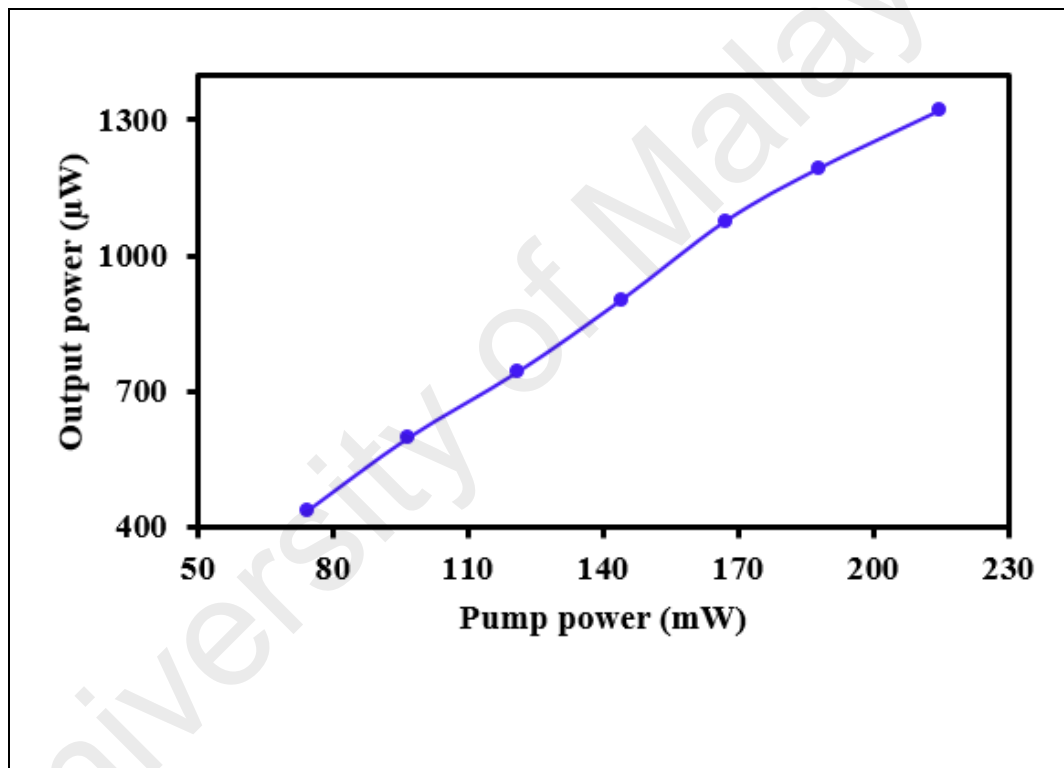


Figure 5.23: Relation between the pump power and output power.

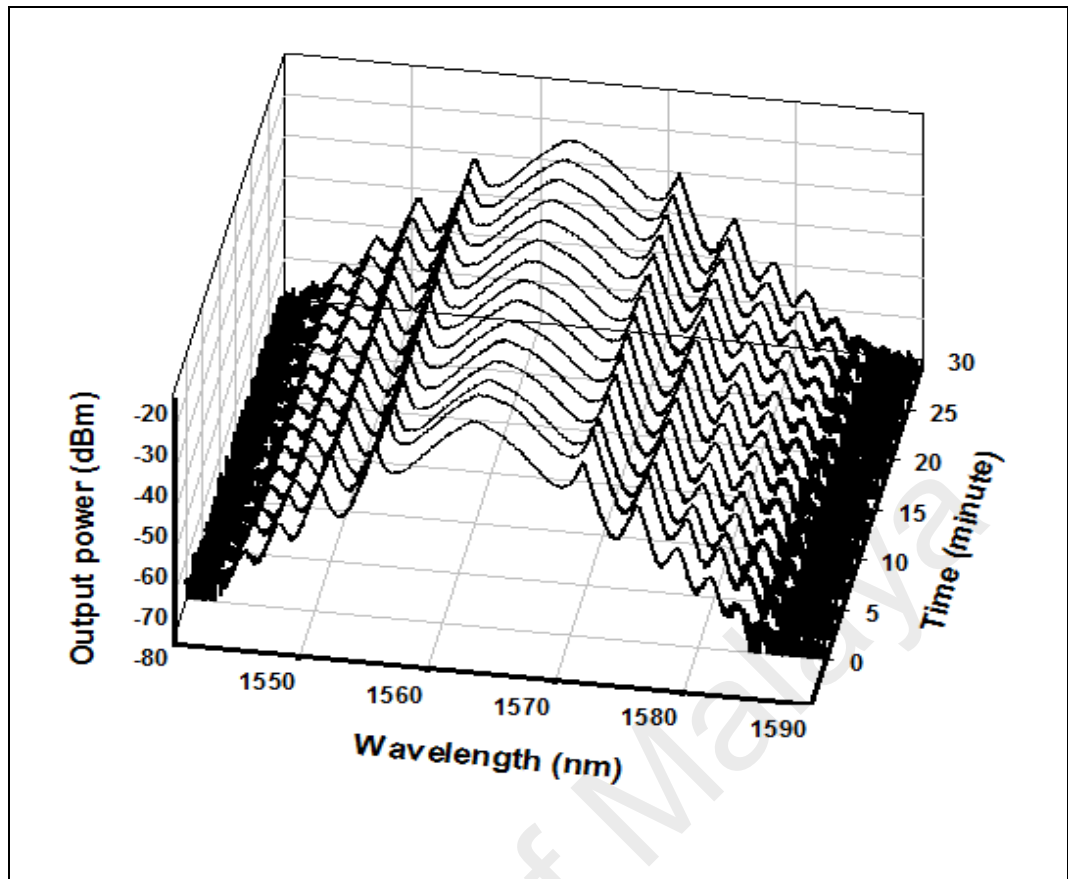


Figure 5.24: Stability of the output optical spectrum over time.

In our study, the mode-locked pulsed lasing results remained consistent throughout the stability measurement period (30 minutes). However, intra-cavity pulses were not observed and thus were not reported. Since the experiment was conducted at a low input power (167.23 mW), no evidence of multiple intra-cavity pulses was observed.

CHAPTER 6: CONCLUSIONS AND FUTURE WORK

6.1 Conclusions

OMFs are versatile and promising components for optical communications systems, sensor devices and fiber laser by virtue of their unique optical and mechanical properties, such as large evanescent fields, strong light confinement, small size, low cost, low loss, ease of configuration and ease of integration with fiber-optic systems. Therefore, in the present work, two techniques were used to fabricate different OMF structures, namely, flame- and microheater-based techniques, both based on the heat-and-pull method. Thus, an inline microfiber Mach-Zehnder interferometer was fabricated using an optical glass processing system (Vytran GPX3400), which is fully computerized. In addition, adiabatic and nonadiabatic OMFs with different dimensions were also fabricated using a simple and cheap homemade tapering setup. These structures were used in two major applications.

6.1.1 Sensing Applications Based on an Inline Microfiber Mach-Zehnder Interferometer

The characteristics of an IMMZI were investigated by observing the change in the FSR as the waist diameter was decreased from $10\mu\text{m}$ to $13\mu\text{m}$ in $1\mu\text{m}$ steps. Moreover, these four samples were utilized as RI sensors for NaCl solutions with different concentrations. The RI values of the NaCl solutions ranged from 1.31837 to 1.31928 RIU. It was concluded that the IMMZI sample with the smallest diameter ($10\mu\text{m}$) compared with the other samples had the highest sensitivity of 2913.7 nm/RIU as a result of the increase in the evanescent field strength with a decreasing OMF diameter.

A comparative study of an IMMZI and an STF was conducted to investigate the sensitivities of these detectors to KNO_3 solutions of different concentrations. The structures had similar dimensions, but the IMMZI possessed two tapered regions, whereas the STF had only one. The study demonstrated that the IMMZI showed a better responsivity to variations in RI compared with the STF.

To investigate the effect of strain on an OMF, an IMMZI was used to generate a stable single wavelength from an EDF in a laser cavity. This single wavelength could be tuned over a range of 6.19 nm, spanning the wavelength range from 1552.94 nm to 1559.13 nm, by means of the 60 μm linear elongation of the IMMZI. The shifting of this single wavelength was studied in three situations: increasing, decreasing and modified stretching. By observing the shift toward the blue region as the strain value increased, the sensitivity of the IMMZI was calculated to be 103.5 pm/ μm , with a slope linearity of more than 99.9%. Based on this result, we conclude that a single generated wavelength can be tuned by modifying the stretching force applied to an IMMZI. The behavior of our proposed IMMZI is reversible and repeatable, and the system a wide tuning range compared with other techniques, which are complex and expensive.

6.1.2 Erbium-Doped Fiber Laser Pulse Generation

The second motivation for this thesis was to generate laser pulses from an erbium-doped fiber, which was successfully achieved in this research. The evanescent field of an OMF was made to interact with a GOSA to create a passively Q-switched pulsed fiber laser. A GO solution was optically deposited on the microfiber surface. When the pump power was increased from 56.172 mW to 105.98 mW, the repetition rate also increased from 37.06 kHz to 53.45 kHz. However, the pulse duration decreased. The evanescent field of a microfiber can be proficiently coupled with GO to facilitate pulsed laser applications.

In the next application, an OMF was employed as a comb-like filter to produce a dual-wavelength output spectrum, which is generally difficult to do using an EDF because it is a homogenous gain medium. In addition, a thin film of graphene, which is a sensitive optical material, was sandwiched between two optical fiber ferrules through a Sagnac loop to generate Q-switched pulses. This simple setup enabled the realization of a passively Q-switched pulsed laser with a dual-wavelength optical spectrum, where the wavelengths were centered at 1549.34 nm and 1559.51 nm. By varying the pump power, the repetition rate of the Q-switched pulses could be tuned from 15.87 kHz to 34.46 kHz. Moreover, the pulse width ranged from 3.8 to 2.7 μ s as the pump power was increased in the range of Q-switching operation. Pulse energies between 4.2 nJ and 5.54 nJ were recorded. The stability of the measured dual-wavelength output power was verified by recording data over a duration of 16 minutes at a pump power of 100 mW. The results indicate that the proposed setup can produce stable dual-wavelength lasing with Q-switched pulsed behavior, which will be useful for many lasing applications.

Mode-locked pulsed EDF lasing was also successfully generated by taking advantage of the interaction of the evanescent field of a side-polished fiber with a GOSA. An optical drop casting method was used to coat the side-polished fiber with a GO solution. Kelly sidebands appeared during the experiment, confirming the occurrence of soliton-regime mode-locking operation. By controlling the polarization status in the laser cavity, the device could be made to produce a mode-locked pulse train with a repetition rate of 8.9 MHz, corresponding to a round trip time of 111.71 ns. A pulse repetition rate of 8.95 MHz was determined from the RF spectrum. The resolution bandwidth (RBW) during the measurement was 300 Hz. The RF spectrum was also observed over a wider range (up to 100 MHz), where the RBW was recorded to be 0.3 MHz. The pulse width was observed using an autocorrelator. The full width at half maximum (FWHM) was recorded to be 1.05 ps.

6.2 Future Work

Future work should focus on achieving the fabrication of an OMF with very low loss, low roughness and high sensitivity by improving the tapering machine specifications. In addition, during this project, many samples of OMFs were fabricated, and we believe that the software for the pulling system requires improvement to better reflect the OMF profile that is produced. Moreover, it will be important to develop new OMF configurations that will allow the evanescent fields to be utilized in a wider variety of applications in the fields of photonics and environmental monitoring, such as the generation of pulses in random fiber lasers based on OMFs or D-shaped fibers by employing nanomaterial-based SAs. Moreover, OMFs can be used as vibration sensors to detect earthquake forces or the vibrations from machines. The performance of an OMF in interacting with the surrounding medium decreases when it is packaged. Therefore, it will be necessary to develop a new packaging material to make OMFs more robust and suitable for real-world applications.

REFERENCES

- Ab Razak, M. Z., Reduan, S. A., Sharbirin, A. S., Jamaludin, N., Zulkifli, M., & Ahmad, H. (2015). Noncontact Optical Displacement Sensor Using an Adiabatic U-Shaped Tapered Fiber. *IEEE Sensors Journal*, 15(10), 5388-5392.
- Afshar, S., Zhang, W. Q., Ebendorff-Heidepriem, H., & Monroe, T. M. (2009). Small core optical waveguides are more nonlinear than expected: experimental confirmation. *Optics Letters*, 34(22), 3577-3579.
- Ahmad, H., & Dernaika, M. (2015). Stabilized single longitudinal mode fibre ring laser based on an inline dual taper Mach Zehnder interferometer filter coated with graphene oxide. *Optics Communications*, 341, 140-146.
- Ahmad, H., Saat, N., & Harun, S. (2005). S-band erbium-doped fiber ring laser using a fiber Bragg grating. *Laser Physics Letters*, 2(7), 369-371.
- Ahmad, H., Salim, M., Azzuhri, S., Zulkifli, M., & Harun, S. (2015). Dual wavelength single longitudinal mode Ytterbium-doped fiber laser using a dual-tapered Mach-Zehnder interferometer. *Journal of The European Optical Society-Rapid Publications*, 10, 15013-15017.
- Ahmad, H., Salim, M., Soltanian, M., Azzuhri, S. R., & Harun, S. (2015a). Passively dual-wavelength Q-switched ytterbium doped fiber laser using Selenium Bismuth as saturable absorber. *Journal of Modern Optics*, 62(19), 1550-1554.
- Ahmad, H., Shahi, S., & Harun, S. (2010). Bismuth-based erbium-doped fiber as a gain medium for L-band amplification and Brillouin fiber laser. *Laser Physics*, 20(3), 716-719.
- Ahmad, H., Soltanian, M., Pua, C., Alimadad, M., & Harun, S. (2014). Photonic crystal fiber based dual-wavelength Q-switched fiber laser using graphene oxide as a saturable absorber. *Applied Optics*, 53(16), 3581-3586.
- Ahmad, H., Soltanian, M., Pua, C., Zulkifli, M., & Harun, S. (2013). Narrow spacing dual-wavelength fiber laser based on polarization dependent loss control. *IEEE Photonics Journal*, 5(6), 1502706-1502706.
- Ahmad, H., Zulkifli, A. Z., Kiat, Y. Y., & Harun, S. (2014a). Q-switched fibre laser using 21cm Bismuth-erbium doped fibre and graphene oxide as saturable absorber. *Optics Communications*, 310, 53-57.
- Ali, M. M., Ibrahim, S. A., Abu Bakar, M., Noor, A., Ahmad Anas, S., Zamzuri, A., & Mahdi, M. (2014). Tapered-EDF-Based Mach-Zehnder Interferometer for Dual-Wavelength Fiber Laser. *IEEE Photonics Journal*, 6(5), 1-9.
- Babin, S., Kablukov, S., & Vlasov, A. (2007). Tunable fiber Bragg gratings for application in tunable fiber lasers. *Laser Physics*, 17(11), 1323-1326.
- Bai, X., Fan, D., Wang, S., Pu, S., & Zeng, X. (2014). Strain sensor based on fiber ring cavity laser with photonic crystal fiber in-line Mach-Zehnder interferometer. *IEEE Photonics Journal*, 6(4), 1-8.

- Batimalay, M., Harun, S., Ahmad, F., Nor, R., Zulkepely, N., & Ahmad, H. (2014a). Study of a fiber optic humidity sensor based on agarose gel. *Journal of Modern Optics*, 61(3), 244-248.
- Batimalay, M., Harun, S., Ahmad, F., Nor, R. M., Zulkepely, N. R., & Ahmad, H. (2014b). Tapered plastic optical fiber coated with graphene for uric acid detection. *IEEE Sensors Journal*, 14(5), 1704-1709.
- Batimalay, M., Harun, S., Irawati, N., Ahmad, H., & Arof, H. (2015). A study of relative humidity fiber-optic sensors. *IEEE Sensors Journal*, 15(3), 1945-1950.
- Belal, M., Song, Z.-q., Jung, Y., Brambilla, G., & Newson, T. (2010). An interferometric current sensor based on optical fiber micro wires. *Optics Express*, 18(19), 19951-19956.
- Birks, T. A., & Li, Y. W. (1992). The shape of fiber tapers. *Journal of Lightwave Technology*, 10(4), 432-438.
- Bonaccorso, F., Sun, Z., Hasan, T., & Ferrari, A. (2010). Graphene photonics and optoelectronics. *Nature Photonics*, 4(9), 611-622.
- Brambilla, G., Finazzi, V., & Richardson, D. (2004). Ultra-low-loss optical fiber nanotapers. *Optics Express*, 12(10), 2258-2263.
- Brambilla, G., Koizumi, F., Feng, X., & Richardson, D. (2005). Compound-glass optical nanowires. *Electronics Letters*, 41(7), 1-2.
- Brambilla, G., Xu, F., Horak, P., Jung, Y., Koizumi, F., Sessions, N. P., Koukharenko, E., Feng, X., Murugan, G. S., & Wilkinson, J. S. (2009). Optical fiber nanowires and microwires: fabrication and applications. *Advances in Optics and Photonics*, 1(1), 107-161.
- Cai, Z. R., Liu, M., Hu, S., Yao, J., Luo, A. P., Luo, Z. C., & Xu, W. C. (2017). Graphene-Decorated Microfiber Photonic Device for Generation of Rogue Waves in a Fiber Laser. *IEEE Journal of Selected Topics in Quantum Electronics*, 23(1).
- Cardenas-Sevilla, G., Monzon-Hernandez, D., Torres-Gomez, I., & Martínez-Ríos, A. (2012). Tapered Mach-Zehnder interferometer based on two mechanically induced long-period fiber gratings as refractive index sensor. *Optics & Laser Technology*, 44(5), 1516-1520.
- Castillo-Guzman, A., Antonio-Lopez, J., Selvas-Aguilar, R., May-Arrioja, D., Estudillo-Ayala, J., & LiKamWa, P. (2010). Widely tunable erbium-doped fiber laser based on multimode interference effect. *Optics Express*, 18(2), 591-597.
- Chen, G. Y., Ding, M., Newson, T., & Brambilla, G. (2013). A review of microfiber and nanofiber based optical sensors. *The Open Optics Journal*, 7(1), 32-57.
- Chen, H., Babin, F., Leblanc, M., & Schinn, G. (2003). Widely tunable single-frequency erbium-doped fiber lasers. *IEEE Photonics Technology Letters*, 15(2), 185-187.
- Chen, S., Chen, Y., Wu, M., Li, Y., Zhao, C., & Wen, S. (2014). Stable-Switched Erbium-Doped Fiber Laser Based on Topological Insulator Covered Microfiber. *IEEE Photonics Technology Letters*, 26(10), 987-990.

- Chen, Y., Ma, Z., Yang, Q., & Tong, L.-M. (2008). Compact optical short-pass filters based on microfibers. *Optics Letters*, 33(21), 2565-2567.
- Chen, Y., Zhao, C., Chen, S., Du, J., Tang, P., Jiang, G., Zhang, H., Wen, S., & Tang, D. (2014a). Large energy, wavelength widely tunable, topological insulator Q-switched erbium-doped fiber laser. *IEEE Journal of Selected Topics in Quantum Electronics*, 20(5), 315-322.
- Chenari, Z., Latifi, H., Ghamari, S., Hashemi, R., & Doroodmand, F. (2016). Adiabatic tapered optical fiber fabrication in two step etching. *Optics & Laser Technology*, 76, 91-95.
- Chuo, S. M., & Wang, L. A. (2011). Propagation loss, degradation and protective coating of long drawn microfibers. *Optics Communications*, 284(12), 2825-2828.
- Cordeiro, C., Wadsworth, W., Birks, T., & Russell, P. S. J. (2005). Engineering the dispersion of tapered fibers for supercontinuum generation with a 1064 nm pump laser. *Optics Letters*, 30(15), 1980-1982.
- Culshaw, B. (2004). Optical fiber sensor technologies: opportunities and-perhaps-pitfalls. *Journal of Lightwave Technology*, 22(1), 39-50.
- De-Jun, F., Guan-Xiu, L., Xi-Lu, L., Ming-Shun, J., & Qing-Mei, S. (2014a). Refractive index sensor based on plastic optical fiber with tapered structure. *Applied Optics*, 53(10), 2007-2011.
- De-Jun, F., Mao-Sen, Z., Liu, G., Xi-Lu, L., & Dong-Fang, J. (2014b). D-shaped plastic optical fiber sensor for testing refractive index. *IEEE Sensors Journal*, 14(5), 1673-1676.
- Deng, M., Tang, C. P., Zhu, T., & Rao, Y. J. (2011). PCF-based Fabry-Pérot interferometric sensor for strain measurement at high temperatures. *IEEE Photonics Technology Letters*, 23(11), 700-702.
- Dianov, E. M. (2009). Bi-doped glass optical fibers: Is it a new breakthrough in laser materials? *Journal of Non-Crystalline Solids*, 355(37), 1861-1864.
- Dikin, D. A., Stankovich, S., Zimney, E. J., Piner, R. D., Dommett, G. H., Evmenenko, G., Nguyen, S. T., & Ruoff, R. S. (2007). Preparation and characterization of graphene oxide paper. *Nature*, 448(7152), 457-460.
- Ding, J. F., Zhang, A. P., Shao, L. Y., Yan, J. H., & He, S. (2005). Fiber-taper seeded long-period grating pair as a highly sensitive refractive-index sensor. *IEEE Photonics Technology Letters*, 17(6), 1247-1249.
- Ding, L., Belacel, C., Ducci, S., Leo, G., & Favero, I. (2010). Ultralow loss single-mode silica tapers manufactured by a microheater. *Applied Optics*, 49(13), 2441-2445.
- Fan, D., Mou, C., Bai, X., Wang, S., Chen, N., & Zeng, X. (2014). Passively Q-switched erbium-doped fiber laser using evanescent field interaction with gold-nanosphere based saturable absorber. *Optics Express*, 22(15), 18537-18542.

- Fan, W., Zhang, Z., Wei, X., Gan, J., Zhan, B., Xu, S., & Yang, Z. (2013). Tunable Dual-Wavelength Narrow-Linewidth Microfiber Laser. *Applied Physics Express*, 6(7), 072701-072703.
- Fang, X., Liao, C., & Wang, D. (2010). Femtosecond laser fabricated fiber Bragg grating in microfiber for refractive index sensing. *Optics Letters*, 35(7), 1007-1009.
- Feng, X., Sun, L., Xiong, L., Liu, Y., Yuan, S., Kai, G., & Dong, X. (2004). Switchable and tunable dual-wavelength erbium-doped fiber laser based on one fiber Bragg grating. *Optical Fiber Technology*, 10(3), 275-282.
- Fidanboyly, K., & Efendioglu, H. (2009). *Fiber optic sensors and their applications*. Paper presented at the 5th International Advanced Technologies Symposium (IATS'09), Karabuk, Turkey.
- Foster, M., Dudley, J., Kibler, B., Cao, Q., Lee, D., Trebino, R., & Gaeta, A. (2005). Nonlinear pulse propagation and supercontinuum generation in photonic nanowires: experiment and simulation. *Applied Physics B*, 81(2-3), 363-367.
- Foster, M., & Gaeta, A. (2004). Ultra-low threshold supercontinuum generation in sub-wavelength waveguides. *Optics Express*, 12(14), 3137-3143.
- Gholamzadeh, B., & Nabovati, H. (2008). Fiber optic sensors. *World Academy of Science, Engineering and Technology*, 42(3), 335-340.
- Grattan, K., & Sun, T. (2000). Fiber optic sensor technology: an overview. *Sensors and Actuators A: Physical*, 82(1), 40-61.
- Guan, B. O., Li, J., Jin, L., & Ran, Y. (2013). Fiber Bragg gratings in optical microfibers. *Optical Fiber Technology*, 19(6), 793-801.
- Guo, W., Kou, J. L., Xu, F., & Lu, Y. Q. (2011). Ultra-flattened and low dispersion in engineered microfibers with highly efficient nonlinearity reduction. *Optics Express*, 19(16), 15229-15235.
- Guo, X., & Tong, L. (2008). Supported microfiber loops for optical sensing. *Optics Express*, 16(19), 14429-14434.
- Haddock, H. S., Shankar, P., & Mutharasan, R. (2003a). Evanescent sensing of biomolecules and cells. *Sensors and Actuators B: Chemical*, 88(1), 67-74.
- Haddock, H. S., Shankar, P., & Mutharasan, R. (2003b). Fabrication of biconical tapered optical fibers using hydrofluoric acid. *Materials Science and engineering: B*, 97(1), 87-93.
- Han, C., Ding, H., & Lv, F. (2014). Demonstration of a refractometric sensor based on an optical micro-fiber three-beam interferometer. *Scientific Reports*, 4, 7504-7511.
- Harun, S. W., Abd Rahman, F., Dimyati, K., & Ahmad, H. (2006). An efficient gain-flattened C-band Erbium-doped fiber amplifier. *Laser Physics Letters*, 3(11), 536-538.

- Harun, S. W., Ahmad, H., Jasim, A. A., & Sulaiman, A. (2012a). *Microfiber structures and its sensor and laser applications*. Paper presented at the Photonics Global Conference (PGC), Singapore.
- Harun, S. W., & Arof, H. (2013). *Current Developments in Optical Fiber Technology*. Croatia: InTech.
- Harun, S. W., Ismail, M., Ahmad, F., Ismail, M., Nor, R., Zulkepely, N., & Ahmad, H. (2012b). A Q-switched erbium-doped fiber laser with a carbon nanotube based saturable absorber. *Chinese Physics Letters*, 29(11), 114202-114205.
- Harun, S. W., Lim, K., Jasim, A. A., & Ahmad, H. (2010). Dual wavelength erbium-doped fiber laser using a tapered fiber. *Journal of Modern Optics*, 57(21), 2111-2113.
- Harun, S. W., Lim, K., Tio, C., Dimyati, K., & Ahmad, H. (2013). Theoretical analysis and fabrication of tapered fiber. *Optik-International Journal for Light and Electron Optics*, 124(6), 538-543.
- Harun, S. W., Shirazi, M., & Ahmad, H. (2007). Multiple wavelength Brillouin fiber laser from injection of intense signal light. *Laser Physics Letters*, 4(9), 678-680.
- Haus, H. A. (2000). Mode-locking of lasers. *IEEE Journal of Selected Topics in Quantum Electronics*, 6(6), 1173-1185.
- He, X., Fang, X., Liao, C., Wang, D., & Sun, J. (2009). A tunable and switchable single-longitudinal-mode dual-wavelength fiber laser with a simple linear cavity. *Optics Express*, 17(24), 21773-21781.
- He, X., Liu, Z. B., Wang, D., Yang, M., Hu, T. Y., & Tian, J. G. (2013). Saturable absorber based on graphene-covered-microfiber. *IEEE Photonics Technology Letters*, 25(14), 1392-1394.
- Herda, R., Kivistö, S., & Okhotnikov, O. G. (2008). Dynamic gain induced pulse shortening in Q-switched lasers. *Optics Letters*, 33(9), 1011-1013.
- Hernández-Romano, I., Monzón-Hernández, D., Moreno-Hernández, C., Moreno-Hernandez, D., & Villatoro, J. (2015). Highly sensitive temperature sensor based on a polymer-coated microfiber interferometer. *IEEE Photonics Technology Letters*, 27(24), 2591-2594.
- Honikel, K.-O. (2008). The use and control of nitrate and nitrite for the processing of meat products. *Meat Science*, 78(1), 68-76.
- Hsu, S. H., & Huang, Y. T. (2005). Design and analysis of Mach–Zehnder interferometer sensors based on dual strip antiresonant reflecting optical waveguide structures. *Optics Letters*, 30(21), 2897-2899.
- Huang, H., Yang, L. M., & Liu, J. (2012). *Femtosecond fiber-laser-based, laser-induced breakdown spectroscopy*. Paper presented at the SPIE Defense, Security, and Sensing, Baltimore, USA

- Iadicicco, A., Cusano, A., Cutolo, A., Bernini, R., & Giordano, M. (2004). Thinned fiber Bragg gratings as high sensitivity refractive index sensor. *IEEE Photonics Technology Letters*, 16(4), 1149-1151.
- Ismaeel, R., Lee, T., Ding, M., Belal, M., & Brambilla, G. (2013). Optical microfiber passive components. *Laser & Photonics Reviews*, 7(3), 350-384.
- Jasim, A. A., Harun, S., Muhammad, M., Arof, H., & Ahmad, H. (2013a). Current sensor based on inline microfiber Mach–Zehnder interferometer. *Sensors and Actuators A: Physical*, 192, 9-12.
- Jasim, A. A., Harun, S. W., Arof, H., & Ahmad, H. (2013b). Inline microfiber Mach–Zehnder interferometer for high temperature sensing. *IEEE Sensors Journal*, 13(2), 626-628.
- Jasim, A. A., Hayashi, N., Harun, S. W., Ahmad, H., Penny, R., Mizuno, Y., & Nakamura, K. (2014). Refractive index and strain sensing using inline Mach–Zehnder interferometer comprising perfluorinated graded-index plastic optical fiber. *Sensors and Actuators A: Physical*, 219, 94-99.
- Jasim, A. A., Zulkifli, A., Muhammad, M., Ahmad, H., & Harun, S. (2012). Fabrication and characterization of a 2×2 microfiber knot resonator coupler. *Chinese Physics Letters*, 29(8), 084204-084203.
- Ji, W. B., Liu, H. H., Tjin, S. C., Chow, K. K., & Lim, A. (2012). Ultrahigh sensitivity refractive index sensor based on optical microfiber. *IEEE Photonics Technology Letters*, 24(20), 1872-1874.
- Jiang, X., Chen, Y., Vienne, G., & Tong, L. (2007a). All-fiber add-drop filters based on microfiber knot resonators. *Optics Letters*, 32(12), 1710-1712.
- Jiang, X., Song, Q., Xu, L., Fu, J., & Tong, L. (2007). Microfiber knot dye laser based on the evanescent-wave-coupled gain. *Applied Physics Letters*, 90(23), 233501.
- Jiang, X., Tong, L., Vienne, G., Guo, X., Tsao, A., Yang, Q., & Yang, D. (2006). Demonstration of optical microfiber knot resonators. *Applied Physics Letters*, 88(22), 223501-223503.
- John, S. M. (2011). *Evanescent wave fibre optic sensors: design, fabrication and characterization*. (PhD), Cochin University of Science and Technology, India
- Jun-Qing, Z., Yong-Gang, W., Pei-Guang, Y., Shuang-Chen, R., Jian-Qun, C., Ge-Guo, D., Yong-Qin, Y., Ge-Lin, Z., Hui-Feng, W., & Jie, L. (2012). Graphene-oxide-based Q-switched fiber laser with stable five-wavelength operation. *Chinese Physics Letters*, 29(11), 114206-114210.
- Jung, M., Koo, J., Chang, Y., Debnath, P., Song, Y., & Lee, J. (2012). An all fiberized, 1.89- μm Q-switched laser employing carbon nanotube evanescent field interaction. *Laser Physics Letters*, 9(9), 669-673.
- Jung, Y., Brambilla, G., & Richardson, D. J. (2009). Optical microfiber coupler for broadband single-mode operation. *Optics Express*, 17(7), 5273-5278.

- Kakarantzas, G., Dimmick, T., Birks, T., Le Roux, R., & Russell, P. S. J. (2001). Miniature all-fiber devices based on CO₂ laser microstructuring of tapered fibers. *Optics Letters*, 26(15), 1137-1139.
- Kashiwagi, K., & Yamashita, S. (2009). Deposition of carbon nanotubes around microfiber via evanescent light. *Optics Express*, 17(20), 18364-18370.
- Keller, U., Weingarten, K. J., Kartner, F. X., Kopf, D., Braun, B., Jung, I. D., Fluck, R., Honninger, C., Matuschek, N., & Der Au, J. A. (1996). Semiconductor saturable absorber mirrors (SESAM's) for femtosecond to nanosecond pulse generation in solid-state lasers. *IEEE Journal of Selected Topics in Quantum Electronics*, 2(3), 435-453.
- Khazaeinezhad, R., Kassani, S. H., Jeong, H., Park, K. J., Kim, B. Y., Yeom, D.-I., & Oh, K. (2015). Ultrafast pulsed all-fiber laser based on tapered fiber enclosed by few-layer WS₂ nanosheets. *IEEE Photonics Technology Letters*, 27(15), 1581-1584.
- Khijwania, S., & Gupta, B. (1999). Fiber optic evanescent field absorption sensor: effect of fiber parameters and geometry of the probe. *Optical and Quantum Electronics*, 31(8), 625-636.
- Khudus, M. I. A., De Lucia, F., Corbari, C., Lee, T., Horak, P., Sazio, P., & Brambilla, G. (2016). *Four-wave mixing UV generation in optical microfibers*. Paper presented at the SPIE Photonics Europe, Brussels, Belgium.
- Kou, J. L., Qiu, S. J., Xu, F., & Lu, Y. Q. (2011). Demonstration of a compact temperature sensor based on first-order Bragg grating in a tapered fiber probe. *Optics Express*, 19(19), 18452-18457.
- Kowsari, A., Ahmadi, V., Darvish, G., & Moravvej-Farshi, M. (2016). Dynamic analysis of optical microfiber coil resonators. *Applied Optics*, 55(24), 6680-6687.
- Kurkov, A. (2011). Q-switched all-fiber lasers with saturable absorbers. *Laser Physics Letters*, 8(5), 335-342.
- Layeghi, A., Latifi, H., & Frazao, O. (2014). Magnetic field sensor based on nonadiabatic tapered optical fiber with magnetic fluid. *IEEE Photonics Technology Letters*, 26(19), 1904-1907.
- Lee, B. H., Kim, Y. H., Park, K. S., Eom, J. B., Kim, M. J., Rho, B. S., & Choi, H. Y. (2012). Interferometric fiber optic sensors. *Sensors*, 12(3), 2467-2486.
- Lee, J., Koo, J., Debnath, P., Song, Y., & Lee, J. (2013). A Q-switched, mode-locked fiber laser using a graphene oxide-based polarization sensitive saturable absorber. *Laser Physics Letters*, 10(3), 035103-035106.
- Lee, K., Fok, M., Wan, S., & Shu, C. (2004). Optically controlled Sagnac loop comb filter. *Optics Express*, 12(25), 6335-6340.
- Leon-Saval, S., Birks, T., Wadsworth, W., Russell, P. S. J., & Mason, M. (2004). Supercontinuum generation in submicron fibre waveguides. *Optics Express*, 12(13), 2864-2869.

- Leung, A., Shankar, P. M., & Mutharasan, R. (2007). A review of fiber-optic biosensors. *Sensors and Actuators B: Chemical*, 125(2), 688-703.
- Li, C., Chen, J. H., Yan, S. C., Xu, F., & Lu, Y. Q. (2016). A Fiber Laser Using Graphene-Integrated 3-D Microfiber Coil. *IEEE Photonics Journal*, 8(1), 1-7.
- Li, C., Qiu, S. J., Chen, Y., Xu, F., & Lu, Y. Q. (2012). Ultra-sensitive refractive index sensor with slightly tapered photonic crystal fiber. *IEEE Photonics Technology Letters*, 24(17), 1771-1774.
- Li, W., Hu, Z., Li, X., Fang, W., Guo, X., Tong, L., & Lou, J. (2014). High-sensitivity microfiber strain and force sensors. *Optics Communications*, 314, 28-30.
- Li, X., Yang, C., Yang, S., & Li, G. (2012a). Fiber-optical sensors: Basics and applications in multiphase reactors. *Sensors*, 12(9), 12519-12544.
- Liao, C., Chen, H., & Wang, D. (2014). Ultracompact optical fiber sensor for refractive index and high-temperature measurement. *Journal of Lightwave Technology*, 32(14), 2531-2535.
- Liao, C., Wang, D., & Wang, Y. (2013). Microfiber in-line Mach-Zehnder interferometer for strain sensing. *Optics Letters*, 38(5), 757-759.
- Lim, K., Ahmad, H., Arof, H., & Harun, S. (2012). Fabrication and applications of microfiber in *Selected Topics on Optical Fiber Technology* (pp. 473-508). Croatia: IN Tech.
- Lim, K., Harun, S., Damanhuri, S., Jasim, A. A., Tio, C., & Ahmad, H. (2011). Current sensor based on microfiber knot resonator. *Sensors and Actuators A: Physical*, 167(1), 60-62.
- Lin, Y. H., & Lin, G. R. (2013). Kelly sideband variation and self four-wave-mixing in femtosecond fiber soliton laser mode-locked by multiple exfoliated graphite nanoparticles. *Laser Physics Letters*, 10(4), 045109-045121.
- Liu, H., Chow, K., Yamashita, S., & Set, S. (2013a). Carbon-nanotube-based passively Q-switched fiber laser for high energy pulse generation. *Optics & Laser Technology*, 45, 713-716.
- Liu, H., Zheng, X. W., Liu, M., Zhao, N., Luo, A. P., Luo, Z. C., Xu, W. C., Zhang, H., Zhao, C. J., & Wen, S. C. (2014). Femtosecond pulse generation from a topological insulator mode-locked fiber laser. *Optics Express*, 22(6), 6868-6873.
- Liu, J., Xu, J., & Wang, P. (2012). Graphene-based passively Q-switched 2 μ m thulium-doped fiber laser. *Optics Communications*, 285(24), 5319-5322.
- Liu, L., Zheng, Z., Zhao, X., Sun, S., Bian, Y., Su, Y., Liu, J., & Zhu, J. (2013). Dual-wavelength passively Q-switched Erbium doped fiber laser based on an SWNT saturable absorber. *Optics Communications*, 294, 267-270.
- Liu, Z., Wang, Y., Zhang, X., Xu, Y., Chen, Y., & Tian, J. (2009). Nonlinear optical properties of graphene oxide in nanosecond and picosecond regimes. *Applied Physics Letters*, 94(2), 021902-021905.

- Lou, J., Carruthers, T., & Currie, M. (2004). 4×10 GHz mode-locked multiple-wavelength fiber laser. *IEEE Photonics Technology Letters*, 16(1), 51-53.
- Lou, J., Wang, Y., & Tong, L. (2014). Microfiber optical sensors: A review. *Sensors*, 14(4), 5823-5844.
- Love, J., Henry, W., Stewart, W., Black, R., Lacroix, S., & Gonthier, F. (1991). Tapered single-mode fibres and devices. I. Adiabaticity criteria. *IEE Proceedings J-Optoelectronics*, 138(5), 343-354.
- Lu, X. Y., & Wang, L. A. (2015). *A stable packaged high-Q microfiber coil resonator*. Paper presented at the 2015 20th Microoptics Conference (MOC), Japan.
- Luo, A.-P., Liu, M., Wang, X.-D., Ning, Q.-Y., Xu, W.-C., & Luo, Z.-C. (2015a). Few-layer MoS₂-deposited microfiber as highly nonlinear photonic device for pulse shaping in a fiber laser [Invited]. *Photonics Research*, 3(2), A69-A78.
- Luo, H., Sun, Q., Xu, Z., Liu, D., & Zhang, L. (2014). Simultaneous measurement of refractive index and temperature using multimode microfiber-based dual Mach-Zehnder interferometer. *Optics Letters*, 39(13), 4049-4052.
- Luo, Z., Wang, J., Zhou, M., Xu, H., Cai, Z., & Ye, C. (2012). Multiwavelength mode-locked erbium-doped fiber laser based on the interaction of graphene and fiber-taper evanescent field. *Laser Physics Letters*, 9(3), 229-233.
- Luo, Z., Zhou, M., Weng, J., Huang, G., Xu, H., Ye, C., & Cai, Z. (2010). Graphene-based passively Q-switched dual-wavelength erbium-doped fiber laser. *Optics Letters*, 35(21), 3709-3711.
- Luo, Z. C., Cao, W. J., Luo, A. P., & Xu, W. C. (2012a). Optical deposition of graphene saturable absorber integrated in a fiber laser using a slot collimator for passive mode-locking. *Applied Physics Express*, 5(5), 055103-055106.
- Luo, Z. C., Liu, M., Guo, Z. N., Jiang, X. F., Luo, A. P., Zhao, C. J., Yu, X. F., Xu, W. C., & Zhang, H. (2015). Microfiber-based few-layer black phosphorus saturable absorber for ultra-fast fiber laser. *Optics Express*, 23(15), 20030-20039.
- Luo, Z. C., Liu, M., Liu, H., Zheng, X. W., Luo, A. P., Zhao, C. J., Zhang, H., Wen, S. C., & Xu, W. C. (2013). 2 GHz passively harmonic mode-locked fiber laser by a microfiber-based topological insulator saturable absorber. *Optics Letters*, 38(24), 5212-5215.
- Ma, C. J., Ren, L. Y., Xu, Y. P., Wang, Y. L., Liang, J., & Qu, E. S. (2014). Design and fabrication of tapered microfiber waveguide with good optical and mechanical performance. *Journal of Modern Optics*, 61(8), 683-687.
- Mahdi, M., Adikan, F. M., Poopalan, P., Selvakenedy, S., Chan, W., & Ahmad, H. (2000). Long-wavelength EDFA gain enhancement through 1550 nm band signal injection. *Optics Communications*, 176(1), 125-129.
- Maran, J. N., Slavík, R., LaRochelle, S., & Karásek, M. (2004). Chromatic dispersion measurement using a multiwavelength frequency-shifted feedback fiber laser. *IEEE Transactions on Instrumentation and Measurement*, 53(1), 67-71.

- Mary, R., Choudhury, D., & Kar, A. K. (2014). Applications of fiber lasers for the development of compact photonic devices. *IEEE Journal of Selected Topics in Quantum Electronics*, 20(5), 72-84.
- Masson, J., St-Gelais, R., Poulin, A., & Peter, Y. A. (2010). Tunable fiber laser using a MEMS-based in plane Fabry-Pérot filter. *IEEE Journal of Quantum Electronics*, 46(9), 1313-1319.
- McAtamney, C., Cronin, A., Sherlock, R., O'Connor, G., & Glynn, T. (2005). *Reproducible method for fabricating fused biconical tapered couplers using a CO₂ laser based process*. Paper presented at the Proceedings of the Third International WLT-Conference on Lasers in Manufacturing, Munich.
- Mehta, A., Mohammed, W., & Johnson, E. G. (2003). Multimode interference-based fiber-optic displacement sensor. *IEEE Photonics Technology Letters*, 15(8), 1129-1131.
- Men, S., Liu, Z., Zhang, X., Wang, Q., Shen, H., Bai, F., Gao, L., Xu, X., Wei, R., & Chen, X. (2013). A graphene passively Q-switched Nd: YAG ceramic laser at 1123 nm. *Laser Physics Letters*, 10(3), 035803.
- Méndez, A., & Morse, T. F. (2011). *Specialty optical fibers handbook*. Imprint of Elsevier: Oxford, UK: Academic Press.
- Miao, Y., Wu, J., Lin, W., Zhang, K., Yuan, Y., Song, B., Zhang, H., Liu, B., & Yao, J. (2013). Magnetic field tunability of optical microfiber taper integrated with ferrofluid. *Optics Express*, 21(24), 29914-29920.
- Minkovich, V. P., Monzón-Hernández, D., Villatoro, J., & Badenes, G. (2006). Microstructured optical fiber coated with thin films for gas and chemical sensing. *Optics Express*, 14(18), 8413-8418.
- Mishakov, G. V., & Sokolov, V. I. (2002). *Precision technique for side-polished fiber fabrication*. Paper presented at the Seventh International Conference on Laser and Laser Information Technologies, Russia.
- Mitschke, F. (2010). *Fiber Optics: Physics and Technology*. Berlin: Springer Science & Business Media.
- Monk, D. J., & Walt, D. R. (2004). Optical fiber-based biosensors. *Analytical and Bioanalytical Chemistry*, 379(7-8), 931-945.
- Muhammad, F., Zulkifli, M., Latif, A., Harun, S., & Ahmad, H. (2012). Graphene-based saturable absorber for single-longitudinal-mode operation of highly doped erbium-doped fiber laser. *IEEE Photonics Journal*, 4(2), 467-475.
- Muhammad, M., Jasim, A. A., Ahmad, H., Arof, H., & Harun, S. (2013). Non-adiabatic silica microfiber for strain and temperature sensors. *Sensors and Actuators A: Physical*, 192, 130-132.
- Nikbakht, H., Latifi, H., Oraie, M., & Amini, T. (2015). Fabrication of Tapered Tip Fibers With a Controllable Cone Angle Using Dynamical Etching. *Journal of Lightwave Technology*, 33(23), 4707-4711.

- Nishizawa, N. (2014). Ultrashort pulse fiber lasers and their applications. *Japanese Journal of Applied Physics*, 53(9), 090101-090111.
- Orucevic, F., Lefèvre-Seguin, V., & Hare, J. (2007). Transmittance and near-field characterization of sub-wavelength tapered optical fibers. *Optics Express*, 15(21), 13624-13629.
- Ozcan, L., Treanton, V., Guay, F., & Kashyap, R. (2007). Highly symmetric optical fiber tapers fabricated with a CO₂ laser. *IEEE Photonics Technology Letters*, 19(9), 656-658.
- Paunescu, G., Hein, J., & Sauerbrey, R. (2004). 100-fs diode-pumped Yb: KGW mode-locked laser. *Applied Physics B*, 79(5), 555-558.
- Perez-Herrera, R., Ullan, A., Leandro, D., Fernandez-Vallejo, M., Quintela, M., Loayssa, A., Lopez-Higuera, J., & Lopez-Amo, M. (2012). L-band multiwavelength single-longitudinal mode fiber laser for sensing applications. *Journal of Lightwave Technology*, 30(8), 1173-1177.
- Qazi, H. H., Mohammad, A. B., Ahmad, H., & Zulkifli, M. Z. (2016a). D-Shaped Polarization Maintaining Fiber Sensor for Strain and Temperature Monitoring. *Sensors*, 16(9), 1505-1517.
- Qazi, H. H., Mohammad, A. B. B., Ahmad, H., Zulkifli, M., & Harun, S. (2016b). Single-mode D-shaped optical fiber sensor for the refractive index monitoring of liquid. *Journal of Modern Optics*, 63(8), 750-755.
- Raji, Y., Lin, H., Ibrahim, S., Mokhtar, M., & Yusoff, Z. (2016). Intensity-modulated abrupt tapered Fiber Mach-Zehnder Interferometer for the simultaneous sensing of temperature and curvature. *Optics & Laser Technology*, 86, 8-13.
- Rao, Y., Zhu, T., Ran, Z., Wang, Y., Jiang, J., & Hu, A. (2004). Novel long-period fiber gratings written by high-frequency CO₂ laser pulses and applications in optical fiber communication. *Optics Communications*, 229(1), 209-221.
- Saleh, Z., Anyi, C., Rahman, A., Ali, N., Harun, S., Manaf, M., & Arof, H. (2014). Q-switched erbium-doped fibre laser using graphene-based saturable absorber obtained by mechanical exfoliation. *Ukrainian Journal of Physical Optics*(15, № 1), 24-29.
- Selvarajan, A. (2010). Fiber optic sensors and their applications. *Indian Institute of Science*, 1-6.
- Selvas-Aguilar, R., Martínez-Rios, A., Anzueto-Sánchez, G., Castillo-Guzmán, A., Hernández-Luna, M., & Robledo-Fava, R. (2014). Tuning of an erbium-doped fiber ring laser based on heating a tapered fiber filter. *Optical Fiber Technology*, 20(4), 391-394.
- Set, S. Y., Yaguchi, H., Tanaka, Y., & Jablonski, M. (2004). Ultrafast fiber pulsed lasers incorporating carbon nanotubes. *IEEE Journal of Selected Topics in Quantum Electronics*, 10(1), 137-146.
- Shahriary, L., & Athawale, A. A. (2014). Graphene oxide synthesized by using modified hummers approach. *Int J Renew Energy Environ Eng*, 2, 58-63.

- Shi, L., Xu, Y., Tan, W., & Chen, X. (2007). Simulation of optical microfiber loop resonators for ambient refractive index sensing. *Sensors*, 7(5), 689-696.
- Sindelar, J. J., & Milkowski, A. L. (2012). Human safety controversies surrounding nitrate and nitrite in the diet. *Nitric Oxide*, 26(4), 259-266.
- Skorczakowski, M., Swiderski, J., Pichola, W., Nyga, P., Zajac, A., Maciejewska, M., Galecki, L., Kasprzak, J., Gross, S., & Heinrich, A. (2010). Mid-infrared Q-switched Er: YAG laser for medical applications. *Laser Physics Letters*, 7(7), 498-504.
- Snyder, A. W. (1970). Coupling of modes on a tapered dielectric cylinder. *IEEE Transactions on Microwave Theory and Techniques*, 18(7), 383-392.
- Sobon, G., Sotor, J., Jagiello, J., Kozinski, R., Librant, K., Zdrojek, M., Lipinska, L., & Abramski, K. M. (2012). Linearly polarized, Q-switched Er-doped fiber laser based on reduced graphene oxide saturable absorber. *Applied Physics Letters*, 101(24), 241106-241110.
- Song, Y. W., Jang, S. Y., Han, W. S., & Bae, M. K. (2010). Graphene mode-lockers for fiber lasers functioned with evanescent field interaction. *Applied Physics Letters*, 96(5), 051122-051125.
- Sotor, J., Sobon, G., Macherzynski, W., Paletko, P., & Abramski, K. M. (2015). Black phosphorus saturable absorber for ultrashort pulse generation. *Applied Physics Letters*, 107(5), 051108-051113.
- Sulaiman, A., Harun, S., Aryanfar, I., & Ahmad, H. (2012). DC current sensing capability of microfiber Mach-Zehnder interferometer. *Electronics Letters*, 48(15), 943-945.
- Sumetsky, M. (2006). How thin can a microfiber be and still guide light? *Optics Letters*, 31(7), 870-872.
- Sumetsky, M. (2008). Basic elements for microfiber photonics: Micro/nanofibers and microfiber coil resonators. *Journal of Lightwave Technology*, 26(1), 21-27.
- Sumetsky, M., Dulashko, Y., Fini, J. M., & Hale, A. (2005). Optical microfiber loop resonator. *Applied Physics Letters*, 86(16), 161108-161111.
- Sun, L., Jiang, S., & Marciante, J. (2010). All-fiber optical magnetic-field sensor based on Faraday rotation in highly terbium-doped fiber. *Optics Express*, 18(6), 5407-5412.
- Sun, L., Li, J., Tan, Y., Shen, X., Xie, X., Gao, S., & Guan, B.-O. (2012). Miniature highly-birefringent microfiber loop with extremely-high refractive index sensitivity. *Optics Express*, 20(9), 10180-10185.
- Sun, Q., Sun, X., Jia, W., Xu, Z., Luo, H., Liu, D., & Zhang, L. (2016). Graphene-Assisted Microfiber for Optical-Power-Based Temperature Sensor. *IEEE Photonics Technology Letters*, 28(4), 383-386.
- Sun, Z., Hasan, T., Torrisi, F., Popa, D., Privitera, G., Wang, F., Bonaccorso, F., Basko, D. M., & Ferrari, A. C. (2010a). Graphene mode-locked ultrafast laser. *ACS nano*, 4(2), 803-810.

- Svelto, O., & Hanna, D. C. (1976). *Principles of lasers*: Springer.
- Taghipour, Z., Zibaii, M., Saeedian, Z., Ghezelayagh, M., & Latifi, H. (2012). *Enhanced sensitivity of gold modified tapered long period fiber grating for refractive index measurement*. Paper presented at the OFS2012 22nd International Conference on Optical Fiber Sensor, China.
- Talaverano, L., Abad, S., Jarabo, S., & Lopez-Amo, M. (2001). Multiwavelength fiber laser sources with Bragg-grating sensor multiplexing capability. *Journal of Lightwave Technology*, 19(4), 553-558.
- Tan, Y., Sun, L. P., Jin, L., Li, J., & Guan, B. O. (2013). Temperature-insensitive humidity sensor based on a silica fiber taper interferometer. *IEEE Photonics Technology Letters*, 25(22), 2201-2204.
- Tang, S. H., Wu, Z. X., Xu, F., & Lu, Y. Q. (2016). Simulation of Optical Microfiber Strain Sensors Based on Four-Wave Mixing. *IEEE Sensors Journal*, 16(9), 3068-3074.
- Tian, Y., Wang, W., Wu, N., Zou, X., & Wang, X. (2011). Tapered optical fiber sensor for label-free detection of biomolecules. *Sensors*, 11(4), 3780-3790.
- Tian, Z., Yam, S. S., & Loock, H. P. (2008). Refractive index sensor based on an abrupt taper Michelson interferometer in a single-mode fiber. *Optics Letters*, 33(10), 1105-1107.
- Tong, L. (2010). Brief introduction to optical microfibers and nanofibers. *Frontiers of Optoelectronics in China*, 3(1), 54-60.
- Tong, L., Gattass, R. R., Ashcom, J. B., He, S., Lou, J., Shen, M., Maxwell, I., & Mazur, E. (2003). Subwavelength-diameter silica wires for low-loss optical wave guiding. *Nature*, 426(6968), 816-819.
- Tong, L., & Sumetsky, M. (2011). *Subwavelength and nanometer diameter optical fibers*. Zhejiang: Springer Science & Business Media.
- Tuma, M. L. (1995). US Patent No. NASA Lewis Research Center; Cleveland, OH, United States.
- Walsh, B. M. (2010). Dual wavelength lasers. *Laser Physics*, 20(3), 622-634.
- Wang, J., Luo, Z., Zhou, M., Ye, C., Fu, H., Cai, Z., Cheng, H., Xu, H., & Qi, W. (2012). Evanescent-light deposition of graphene onto tapered fibers for passive Q-switch and mode-locker. *IEEE Photonics Journal*, 4(5), 1295-1305.
- Wang, M., Yang, M., Cheng, J., Dai, J., Yang, M., & Wang, D. (2012a). Femtosecond laser fabricated micro Mach-Zehnder interferometer with Pd film as sensing materials for hydrogen sensing. *Optics Letters*, 37(11), 1940-1942.
- Wang, P., Bo, L., Semenova, Y., Farrell, G., & Brambilla, G. (2015). Optical microfiber based photonic components and their applications in label-free biosensing. *Biosensors*, 5(3), 471-499.

- Wang, P., Lee, T., Ding, M., Lian, Z., Feng, X., Ma, Y., Bo, L., Wu, Q., Semenova, Y., & Loh, W. (2014). White light trapping using supercontinuum generation spectra in a lead-silicate fibre taper. *Journal of Lightwave Technology*, 32(1), 40-45.
- Wang, P., Wang, L., Shi, G., He, T., Li, H., & Liu, Y. (2016). Stable multi-wavelength fiber laser with single-mode fiber in a Sagnac loop. *Applied Optics*, 55(12), 3339-3342.
- Wang, P., Weng, D., Li, K., Liu, Y., Yu, X., & Zhou, X. (2013). Multi-wavelength Erbium-doped fiber laser based on four-wave-mixing effect in single mode fiber and high nonlinear fiber. *Optics Express*, 21(10), 12570-12578.
- Ward, J., Maimaiti, A., Le, V. H., & Chormaic, S. N. (2014). Contributed Review: Optical micro-and nanofiber pulling rig. *Review of Scientific Instruments*, 85(11), 111501-111511.
- Ward, J. M., O'Shea, D. G., Shortt, B. J., Morrissey, M. J., Deasy, K., & Chormaic, S. G. N. (2006). Heat-and-pull rig for fiber taper fabrication. *Review of Scientific Instruments*, 77(8), 083105-083110.
- Wei, T., Lan, X., & Xiao, H. (2009). Fiber Inline Core-Cladding-Mode Mach-Zehnder Interferometer Fabricated by Two-Point CO Laser Irradiations. *IEEE Photonics Technology Letters*, 21(10), 669-671.
- Wen, X., Ning, T., Bai, Y., Li, C., Li, J., & Zhang, C. (2015). Ultrasensitive temperature fiber sensor based on Fabry-Pérot interferometer assisted with iron V-groove. *Optics Express*, 23(9), 11526-11536.
- Woodward, R. I., & Kelleher, E. J. (2015). 2D saturable absorbers for fibre lasers. *Applied Sciences*, 5(4), 1440-1456.
- Wu, B., Lu, Y., Jing, L., Huang, X., & Yao, J. (2013). The use of a dual-wavelength erbium-doped fiber laser for intra-cavity sensing. *Laser Physics*, 23(11), 115103-115108.
- Wu, C. Y., Lin, P., Huang, R. S., Chao, W. C., & Lee, M. M. (2006). Design optimization for micromachined low power Mach-Zehnder thermo-optic switch. *Applied Physics Letters*, 89(12), 121121.
- Wu, M., Huang, W., & Wang, L. (2008). Propagation characteristics of the silica and silicon subwavelength-diameter hollow wire waveguides. *Chinese Optics Letters*, 6(10), 732-735.
- Wu, X., & Tong, L. (2013). Optical microfibers and nanofibers. *Nanophotonics*, 2(5-6), 407-428.
- Wu, Y., Yao, B., Cheng, Y., Rao, Y., Gong, Y., Zhou, X., Wu, B., & Chiang, K. S. (2014). Four-wave mixing in a microfiber attached onto a graphene film. *IEEE Photonics Technology Letters*, 26(3), 249-252.
- Xian, P., Feng, G., & Zhou, S. (2016). A Compact and Stable Temperature Sensor Based on a Gourd-Shaped Microfiber. *IEEE Photonics Technology Letters*, 28(1), 95-98.

- Xie, G., Ma, J., Lv, P., Gao, W., Yuan, P., Qian, L., Yu, H., Zhang, H., Wang, J., & Tang, D. (2012). Graphene saturable absorber for Q-switching and mode locking at 2 μm wavelength [Invited]. *Optical Materials Express*, 2(6), 878-883.
- Xie, X., Li, J., Sun, L.-P., Shen, X., Jin, L., & Guan, B.-o. (2014). A High-Sensitivity Current Sensor Utilizing CrNi Wire and Microfiber Coils. *Sensors*, 14(5), 8423-8429.
- Xu, J., Liu, J., Wu, S., Yang, Q.-H., & Wang, P. (2012). Graphene oxide mode-locked femtosecond erbium-doped fiber lasers. *Optics Express*, 20(14), 15474-15480.
- Xu, Y., Chen, Z., Li, H., & Wei, Y. (2009). Tapered photonic crystal fiber for supercontinuum generation in telecommunication windows. *Frontiers of Optoelectronics in China*, 2(3), 293-298.
- Xu, Z., Li, Y., & Wang, L. (2014). In situ fine tailoring of group velocity dispersion in optical microfibers via nanocoatings. *Optics Express*, 22(23), 28338-28345.
- Xu, Z., Sun, Q., Li, B., Luo, Y., Lu, W., Liu, D., Shum, P. P., & Zhang, L. (2015). Highly sensitive refractive index sensor based on cascaded microfiber knots with Vernier effect. *Optics Express*, 23(5), 6662-6672.
- Xuan, H., Jin, W., & Zhang, M. (2009). CO₂ laser induced long period gratings in optical microfibers. *Optics Express*, 17(24), 21882-21890.
- Yadav, T., Narayanaswamy, R., Bakar, M. A., Kamil, Y. M., & Mahdi, M. (2014). Single mode tapered fiber-optic interferometer based refractive index sensor and its application to protein sensing. *Optics Express*, 22(19), 22802-22807.
- Yan, S. C., Zheng, B. C., Chen, J. H., Xu, F., & Lu, Y. Q. (2015). Optical electrical current sensor utilizing a graphene-microfiber-integrated coil resonator. *Applied Physics Letters*, 107(5), 053502-053506.
- Yang, C. Y., Lin, Y. H., Chi, Y. C., Wu, C. L., Lo, J. Y., & Lin, G. R. (2015). Pulse-width saturation and Kelly-sideband shift in a graphene-nanosheet mode-locked fiber laser with weak negative dispersion. *Physical Review Applied*, 3(4), 044016-044025.
- Yang, H., Wang, S., Wang, X., Wang, J., & Liao, Y. (2014). Temperature sensing in seawater based on microfiber knot resonator. *Sensors*, 14(10), 18515-18525.
- Yang, R., Yu, Y. S., Chen, C., Xue, Y., Zhang, X. L., Guo, J. C., Wang, C., Zhu, F., Zhang, B. L., & Chen, Q. D. (2012). S-tapered fiber sensors for highly sensitive measurement of refractive index and axial strain. *Journal of Lightwave Technology*, 30(19), 3126-3132.
- Yang, R., Yu, Y. S., Xue, Y., Chen, C., Chen, Q. D., & Sun, H. B. (2011). Single S-tapered fiber Mach-Zehnder interferometers. *Optics Letters*, 36(23), 4482-4484.
- Yang, X., Luo, S., Chen, Z., Ng, J. H., & Lu, C. (2007). Fiber Bragg grating strain sensor based on fiber laser. *Optics Communications*, 271(1), 203-206.

- Yeh, C. H., Shih, F. Y., Chen, C. T., Lee, C. N., & Chi, S. (2007). Stabilized dual-wavelength erbium-doped dual-ring fiber laser. *Optics Express*, 15(21), 13844-13848.
- Yoon, M. S., Kim, S. K., & Han, Y. G. (2015). Highly sensitive current sensor based on an optical microfiber loop resonator incorporating low index polymer overlay. *Journal of Lightwave Technology*, 33(12), 2386-2391.
- Yu, H., Xiong, L., Chen, Z., Li, Q., Yi, X., Ding, Y., Wang, F., Lv, H., & Ding, Y. (2014). Solution concentration and refractive index sensing based on polymer microfiber knot resonator. *Applied Physics Express*, 7(2), 022501-022505.
- Yubing, T., Huiming, T., Jiying, P., & Hongyi, L. (2008). LD-pumped actively Q-switched Yb: YAG laser with an acoustic-optical modulator. *Laser Physics*, 18(1), 12-14.
- Yun-Shan, Z., Xue-Guang, Q., Min, S., & Qin-Peng, L. (2015). In-Fiber Mach—Zehnder Interferometer Based on Waist-Enlarged Taper and Core-Mismatching for Strain Sensing. *Chinese Physics Letters*, 32(6), 064208-064213.
- Zaatar, Y., Zaouk, D., Bechara, J., Khoury, A., Llinaress, C., & Charles, J.-P. (2000). Fabrication and characterization of an evanescent wave fiber optic sensor for air pollution control. *Materials Science and engineering: B*, 74(1), 296-298.
- Zhai, G., & Tong, L. (2007). Roughness-induced radiation losses in optical micro or nanofibers. *Optics Express*, 15(21), 13805-13816.
- Zhang, H., Tang, D., Knize, R., Zhao, L., Bao, Q., & Loh, K. P. (2010). Graphene mode locked, wavelength-tunable, dissipative soliton fiber laser. *Applied Physics Letters*, 96(11), 111112-111115.
- Zhang, J., Sun, Q., Liang, R., Wo, J., Liu, D., & Shum, P. (2012). Microfiber Fabry–Perot interferometer fabricated by taper-drawing technique and its application as a radio frequency interrogated refractive index sensor. *Optics Letters*, 37(14), 2925-2927.
- Zhang, Z., Xu, K., Wu, J., Hong, X., & Lin, J. (2008). Multiwavelength figure-of-eight fiber laser with a nonlinear optical loop mirror. *Laser Physics Letters*, 5(3), 213-216.
- Zhao, J., Wang, Y., Yan, P., Ruan, S., Tsang, Y., Zhang, G., & Li, H. (2014a). An Ytterbium-doped fiber laser with dark and Q-switched pulse generation using graphene-oxide as saturable absorber. *Optics Communications*, 312, 227-232.
- Zhao, N., Liu, M., Liu, H., Zheng, X. W., Ning, Q. Y., Luo, A. P., Luo, Z. C., & Xu, W. C. (2014b). Dual-wavelength rectangular pulse Yb-doped fiber laser using a microfiber-based graphene saturable absorber. *Optics Express*, 22(9), 10906-10913.
- Zheng, J., Yan, P., Yu, Y., Ou, Z., Wang, J., Chen, X., & Du, C. (2013). Temperature and index insensitive strain sensor based on a photonic crystal fiber in line Mach—Zehnder interferometer. *Optics Communications*, 297, 7-11.

- Zhou, D. P., Wei, L., Dong, B., & Liu, W. K. (2010). Tunable passively-switched erbium-doped fiber laser with carbon nanotubes as a saturable absorber. *IEEE Photonics Technology Letters*, 22(1), 9-11.
- Zhou, M., Luo, Z., Wang, J., Ye, C., Fu, H., Zhang, C., Cai, Z., & Xu, H. (2012). Graphene-assisted all-fiber multiwavelength erbium-doped fiber laser functionalized with evanescent field interaction. *Laser Physics*, 22(5), 991-995.
- Zhu, W., Qian, L., & Helmy, A. S. (2015). *Implementation of three functional devices using Erbium-doped fibers: An advanced photonics lab*. Paper presented at the Tenth International Topical Meeting on Education and Training in Optics and Photonics, Canada.
- Zhu, Y., Chen, X., & Wang, A. (2009). Observation of interference in a fiber taper interferometer with a subwavelength tip and its sensing applications. *Optics Letters*, 34(18), 2808-2810.
- Zhu, Y., Murali, S., Cai, W., Li, X., Suk, J. W., Potts, J. R., & Ruoff, R. S. (2010). Graphene and graphene oxide: synthesis, properties, and applications. *Advanced Materials*, 22(35), 3906-3924.
- Zibaii, M., Latifi, H., Karami, M., Gholami, M., Hosseini, S., & Ghezelayagh, M. (2010). Non-adiabatic tapered optical fiber sensor for measuring the interaction between α -amino acids in aqueous carbohydrate solution. *Measurement Science and Technology*, 21(10), 105801-105813.

LIST OF PUBLICATIONS AND PAPERS PRESENTED

- 1- **Jaddoa, M. F.**, Jasim, A. A., Razak, M. Z. A., Harun, S. W., & Ahmad, H. (2016). Highly responsive NaCl detector based on inline microfiber Mach–Zehnder interferometer. *Sensors and Actuators A: Physical*, 237, 56-61.
- 2- **Jaddoa, M. F.**, Razak, M. Z. A., Salim, M. A. M., Sharbirin, A. S., Nayan, N., Ismail, M. F., & Ahmad, H. (2016). Tunable single wavelength erbium-doped fiber ring laser based on in-line Mach-Zehnder strain. *Optik-International Journal for Light and Electron Optics*. 127(20), 8326-8332.
- 3- **Jaddoa, M. F.**, Faruki, M. J., Razak, M. Z. A., Azzuhri, S. R., & Ahmad, H. (2016). Passively Q-switched fiber laser based on interaction of evanescent field in optical microfiber with graphene-oxide saturable absorber. *Ukrainian Journal of Physical Optics*, 17(2), 58-64.
- 4- Ahmad, H., Salim, M. A. M., Azzuhri, S. R., **Jaddoa, M. F.**, & Harun, S. W. (2016). Tunable dual-wavelength ytterbium-doped fiber laser using a strain technique on microfiber Mach–Zehnder interferometer. *Applied Optics*, 55(4), 778-782.
- 5- Ahmad, H., Faruki, M. J., Razak, M. Z. A., **Jaddoa, M. F.**, Azzuhri, S. R., Rahman, M. T. & Ismail, M. F. (2016). A combination of tapered fiber and polarization controller in generating highly stable and tunable dual-wavelength C-band laser. *Journal of Modern Optics*, 64(7), 709-715.
- 6- Ahmad, H., **Jaddoa, M. F.**, Faruki, M. J., Razak, M. Z. A., Azzuhri, S. R., & Ismail, M. F. (2016). Generation of Mode-locked Pulses in a Laser by Utilizing Evanescent Field Interaction with Graphene Oxide. *Optics & Laser Technology*, (submitted paper).